Multiphase Probes of the Baryon Cycle from Big Data Quasar Spectroscopy

Alejandra Yrupe Fresco Arrom

München 2023

Multiphase Probes of the Baryon Cycle from Big Data Quasar Spectroscopy

Alejandra Yrupe Fresco Arrom

Dissertation
an der Fakultät für Physik
der Ludwig–Maximilians–Universität
München

vorgelegt von
Alejandra Yrupe Fresco Arrom
aus Asunción, Paraguay

München, den May 11th, 2023

Erstgutachter: Prof. Dr. Kirpal Nandra
Zweitgutachter: Prof. Dr. Klaus Dolag
Tag der mündlichen Prüfung: June 20th, 2023

Contents

List of Figures

List of Tables

Zusammenfassung

Simulationen der großräumigen Struktur des Universums zeigen das filamentartige kosmische Netz aus Gas, das Galaxien und Galaxiengruppen miteinander verbindet, mit Substrukturen, die komplexe physikalische Prozesse beinhalten, die die Entwicklung von Galaxien vorantreiben. Beispiele für diese Substrukturen sind Filamente aus dem intergalaktischen Medium (IGM) oder dem zirkumgalaktischen Medium (CGM), das die Galaxien umgibt. Diese sind noch zu diffus, um in der Emission beobachtet zu werden, aber die Verwendung von leuchtenden Hintergrundquellen, um dieses schwache Gas in der Absorption zu erkennen, wird zur leistungsfähigsten Technik, um diese Strukturen zu untersuchen.

Die Verwendung von Quasarspektren als Hintergrundquelle kann in einer Vielzahl von Zusammenhängen ein nützliches Werkzeug sein, einschließlich der Untersuchung der großräumigen Struktur und der Umgebungen der Quasare selbst. Ziel dieser Arbeit war es, große Datensätze zu nutzen, um das Signal-Rausch-Verhältnis zu erhöhen, um schwer fassbare Komponenten der baryonischen Materie zu identifizieren, die nicht unbedingt Licht aussenden, aber über Absorptionslinien im elektromagnetischen Spektrum einer Hintergrundquelle aufgedeckt werden können. Unter Verwendung verschiedener bodengestützter Teleskope im optischen Bereich und im nahen UV verwenden wir die Technik des Stacking, die sich die statistisch signifikanten großen Datenmengen zunutze macht.

Das erste Kapitel enthält eine Einführung in die großräumigen Strukturen und andere Objekte, die während der einzelnen Projekte dieser Arbeit untersucht wurden, und gibt einen Überblick über die verwendeten Methoden und Instrumente.

Im zweiten Kapitel wird eine Suche nach dem IGM mit [FeXXI] λ 1354Å vorgestellt, bei der 10^7K-Gas bei UV-Wellenlängen aufgespürt wird. Unter Verwendung von mehr als einhundert Quasar-Spektren mit hoher spektraler Auflösung (R$\sim$ 49.000) und sehr hohem Signal-Rausch-Verhältnis des Very Large Telescope (VLT) und des Ultraviolet Echelle Spectrograph (UVES) haben wir die Rotverschiebung bekannter Damped Lyman-alpha (DLA)-Absorber, die für die Überdichte verantwortlich sind, überlagert. Wir stellen die Ergebnisse der Untersuchungen vor und geben einen Ausblick auf die Möglichkeit, eine ähnliche Studie mit zukünftigen Instrumenten durchzuführen.
Im dritten Kapitel wird eine Studie des Intracluster-Mediums vorgestellt, bei der Quasar-Spektren aus dem Sloan Digital Sky Survey aus Data Release 16 als Hintergrundquellen für ausgewählte Röntgenhaufen aus dem ROSAT All Sky Survey verwendet werden, wobei die spektroskopische Rotverschiebung aus dem SPectroscopic IDentifcation of ERosita Sources (SPIDERS) Programm stammt. Unter Verwendung des MgII-Doubletts als Indikator für

dieses 10^4K-Gas unterteilen wir die Stichprobe in Massen- und Winkelabstandsbereiche und vergleichen sie mit einer bekannten MgII-Absorber-Stichprobe aus SDSS DR16. Wir präsentieren die endgültigen Ergebnisse und vergleichen sie mit Simulationen.

In Kapitel vier untersuchen wir Ausströmungen von Aktiven Galaktischen Kernen (AGN), indem wir SDSS-Quasarspektren verwenden und nach MgII-Absorptionslinien suchen, indem wir eine Stichprobe von 7100 Spektren aus Data Release 18 (DR18) stapeln. Wir stellen unsere Ergebnisse und einen Ausblick auf zukünftige Arbeiten vor.

In Kapitel 5 präsentieren wir eine Zusammenfassung und Schlussfolgerungen mit einem Ausblick auf Möglichkeiten zur Fortsetzung der Forschung in verschiedenen Bereichen, die im Rahmen dieser Arbeit untersucht wurden.

Abstract

Simulations of the large scale structure of the Universe show the filamentary cosmic web of gas connecting galaxies and groups of galaxies with each other, with substructures that involve complex physical processes that drive the evolution of galaxies. Examples of these substructures are filaments from intergalactic medium (IGM) or the circumgalactic medium (CGM) surrounding the galaxies. These are too diffuse to be observed in emission yet, thus using luminous background sources to detect this faint gas in absorption becomes the most powerful technique available to study these structures.

The use of quasar spectra as a background source can be a useful tool in a variety of contexts, including the study of the large scale structure and investigations of the environments of the quasars themselves. The aim of this thesis was to make use of large sets of data to increase the signal to noise ratio in order to identify elusive components of baryonic matter that do not necessarily emit light, but can be revealed via absorption lines in the electromagnetic spectrum of a background source. Using different ground based telescopes from optical and near UV wavelengths, we use the technique of stacking, which takes advantage of the statistically significant large amounts of data being produced.

The first chapter presents an introduction to the large scale structure and other objects that were targeted throughout each project of this thesis, while presenting an overall look of the methods and instruments used.

The second chapter presents a search for the IGM using FeXXI λ 1354Å tracing 10^7K gas at UV wavelengths. Using more than one hundred high-spectral resolution (R$\sim 49,000$) and very high signal to noise quasar spectra from the Very Large Telescope (VLT) and the Ultraviolet Echelle Spectrograph (UVES), we stacked at the redshift of known Damped Lyman-alpha (DLA) absorbers which are tracers of overdensities. We present the results of the findings and provide an outlook for the possibility of performing a similar study with future instruments.

The third chapter presents a study of the Intracluster Medium using quasar spectra from the Sloan Digital Sky Survey from Data Release 16 as background sources for X-ray selected clusters from the ROSAT All Sky Survey, with spectroscopic redshift from the SPectroscopic IDentifcation of ERosita Sources (SPIDERS) program. We present the final results and compare them with simulations. Using the MgII doublet as a tracer of this 10^4K gas, we stack spectra at th redhift of the foreground clusters and we also compare to a known MgII absorbers sample from SDSS DR16. We find tentative evidence of MgII absorption in the whole sample.

In chapter four we study outflows from Active Galactic Nuclei (AGN) by using SDSS quasar spectra and looking for MgII intrinsic absorption lines by stacking a sample of 7100 spectra from Data Release 18 (DR18). We present our results and outlook for future work.

We present summary and conclusions in chapter 5, with an outlook of possibilities to continue the research in different areas that were studied during the course of this thesis.

Chapter 1

Introduction

In the past twenty years, our knowledge of the large scale structure of the Universe has taken a major step thanks to the advances in both simulations and observational capabilities. The cosmological magnetohydrodynamical simulations of galaxy formation such as TNG (Nelson et al., 2020) for example, show how galaxies and groups of galaxies are connected with each other. The large scale structure bears a striking resemblance to a neural map of the brain, a striking image for both the astrophysics community and the public.

From smaller scales of star and planet formation, to galaxy formation, clusters of galaxies and the intergalactic medium connecting all these objects, we are slowly filling in the gaps in our picture of the Universe. However, even considering all the baryonic matter we can observe, this still only corresponds to 5% of the composition of the known Universe. Understanding the interactions and evolution of a system is complex. On the one hand a static image of different objects at different stages of the evolution, like pictures of different human beings at different stages of their lives offers limited information. On the other hand, a still limited computation of possible scenarios of past and future of what we observe, still leaves more open questions than answers.

1.1 Circumgalactic and Intergalactic Medium

The evolution of the cosmic baryons induces processes that can trigger or halt star formation in the interstellar medium (ISM), modifying the flows of gas that ends outside the galaxy stellar body into the surrounding gaseous structure of the galaxy, the circumgalactic medium (CGM; Tumlinson et al. (2017)). The gas that remains in this gaseous halo within the virial radius can be recycled, or can be ejected outside the galaxy. The resupply of new incoming gas happens through accretion from the intergalactic medium (IGM), where the ISM is then able to gain back gas for further star formation processes. In Figure 1.1 we show a very basic schematic of how the galactic growth intakes mass and momentum through accretion from the IGM, and expels them through feedback from supernovae or Active Galactic Nuclei (AGN): in fact, super massive black hole (SMBH) activity can also expel the gas creating outflows all the way out of the galaxy.

1.1.1 Early evolution of the CGM and IGM

After the recombination and neutralization of the Universe at z ∼1,100, the cosmic gas cooled with the expansion of the Universe, creating the conditions for the IGM to emerge as a result of gravity acting on the primordial matter fluctuations. When the first (Population III) stars were created, their low formation rates were only enough to ionize a small fraction of the then neutral IGM. It was not until the first galaxies formed at z ∼ 10, with haloes in which gas are embedded of $\geq 10^8$ $M_\odot$ that could sustain more robust star formation, that the IGM was strongly affected by the radiative backgrounds photoionising intergalactic hydrogen.

The IGM continued its evolution after reionization, which heats the IGM to tens of thousands degrees Kelvin and uniformly ionizes the cosmic intergalactic hydrogen. At lower redshifts (z ∼ 2), cosmological expansion further dilutes this cosmic gas, and structure formation can efficiently shock the intergalactic gas to T∼ 10^{5-6} K (Cen and Ostriker, 1999).

The breakthrough in the study of the gas came with the discovery of quasars and the intervening absorbers in the line of sight, which allowed for the observation of the gas in the intergalactic medium(Wolfe et al., 1995), and the possible connection with close-by galaxies (Bergeron, 1980). This type of observation now comprises one of the most used methods for studying the CGM and IGM (Bouché et al., 2006; Lofthouse et al., 2020; Hamanowicz et al., 2023), together with the state of the art magnetohydrodynamical simulations show us a more complete overview of the inflow and outflow processes in and out of galaxies (Schaye et al., 2015).

1.1.2 Physical characteristics of the CGM and IGM

The CGM is a multiphase diffuse gas extending from the outer stellar disk of the galaxy up to the virial radius. With various states of ionization, velocities, and complex dynamics, it is dominated by cool clumpy collisionally ionised (T∼ $10^{4-5.5}$ K) gas of low density (Tumlinson et al., 2017). Characterising the exact chemical composition, densities and ionization states of the gas is essential to constrain the baryon budget, metallicity and gas flow inside the CGM, but remains difficult due to instrument capabilities. Only a subset of the ionization states of each element lie at accessible wavelengths, and its low surface brightness makes it even more challenging to detect with present-day instruments (Wisotzki et al., 2018; Augustin et al., 2019). Considering the instruments to date used to measure the CGM (ALMA, Hubble, Chandra, XMM-Newton, eROSITA), the rest of the puzzle must be filled in with physical models such as Collisional Photoionization Equilibrium or Photoionization Equilibrium assumption (Fumagalli, 2015).

The cold gas density profile drops with distance from the galaxy, while the hot gas remains mostly constant gradually transforming into diffuse and hot (T∼ 10^6K) Warm-Hot Intergalactic Medium (WHIM) (Cen and Ostriker, 1999; Davé et al., 2001). The WHIM occupies the space from outside the virial radius of galaxies and cluster of galaxies (Tumlinson et al., 2017). These dilute reservoirs of gas filling the space in between the

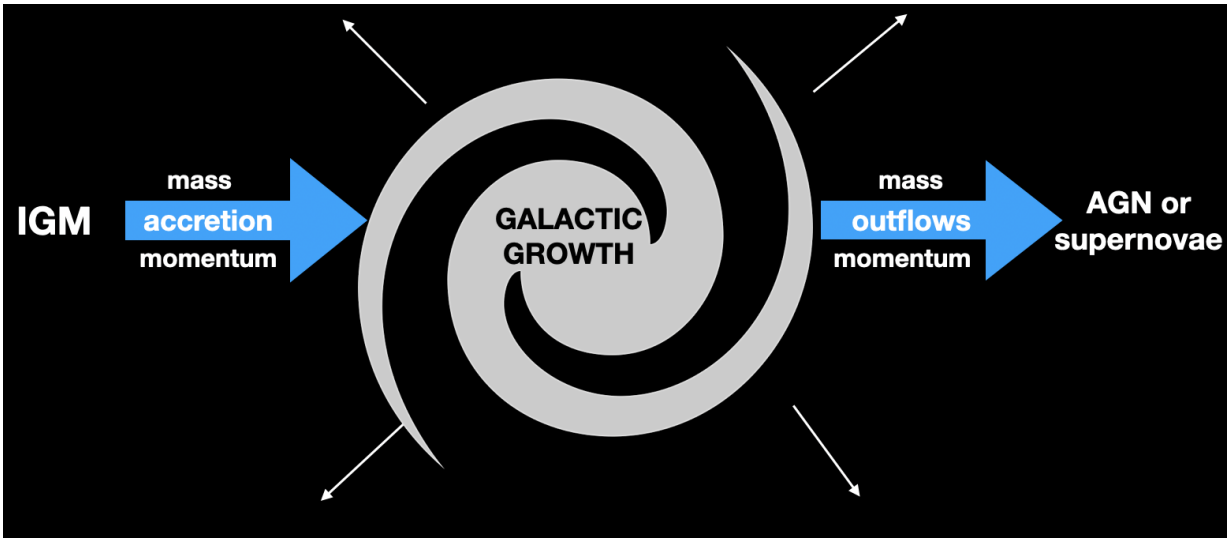

Figure 1.1: Baryon cycle representation, where the galaxy growth gains mass and momentum through accretion of the IGM, and looses them through outflows caused by AGN or supernovae activity.

void of galaxies can be hard to disentangle from the CGM, and have gas densities less than $\sim$ 200 times the mean cosmic density (McQuinn, 2016). The importance of the IGM is based on the fact that most of the baryonic matter resides in these unvirialised structures, as well as roughly half of the dark matter at present day (McQuinn, 2016). In addition, the IGM plays a major role in galaxy growth by resupply of gas, and intake of the gas ejected from both star formation and AGN activity.

1.1.3 Simulations vs. observations

In order reach a full understanding of the complexity and origin of the multiphase CGM, we require more than what current observations and modeling alone can provide. Cosmological hydrodynamical simulations play a key role in deciphering the nature of this inhomogeneous mix of different gas phases, where direct comparisons of synthetic spectra to observations can be achieved (Machado et al., 2018). Nevertheless, the simulations face many of the same challenges as observations, like ionization mechanisms and radiative transfer code assumptions which can end in misleading results.

Observations of the T $< 10^4$ K gas use tracers of neutral and low ionisation state such as HI, K, NaII, CaII. From studies of the Milky Way halo, Magellanic Stream (Putman et al., 2012) and stacked optical spectra from SDSS (Zhu et al., 2014), this gas can make up to $\sim$ 1% of the total baryon budget of the halo. The cool gas with T $< 10^{4-5}$ K that can be traced by UV lines presents a plethora of absorption features at low redshift, which allow us to better constrain estimates total amount of gas due to the neutral atoms and low ionisation states in this temperature range. Figure 1.2 shows a schematics of the main properties of the cold gas around (simulated) galaxies at redshift 2 to 3.

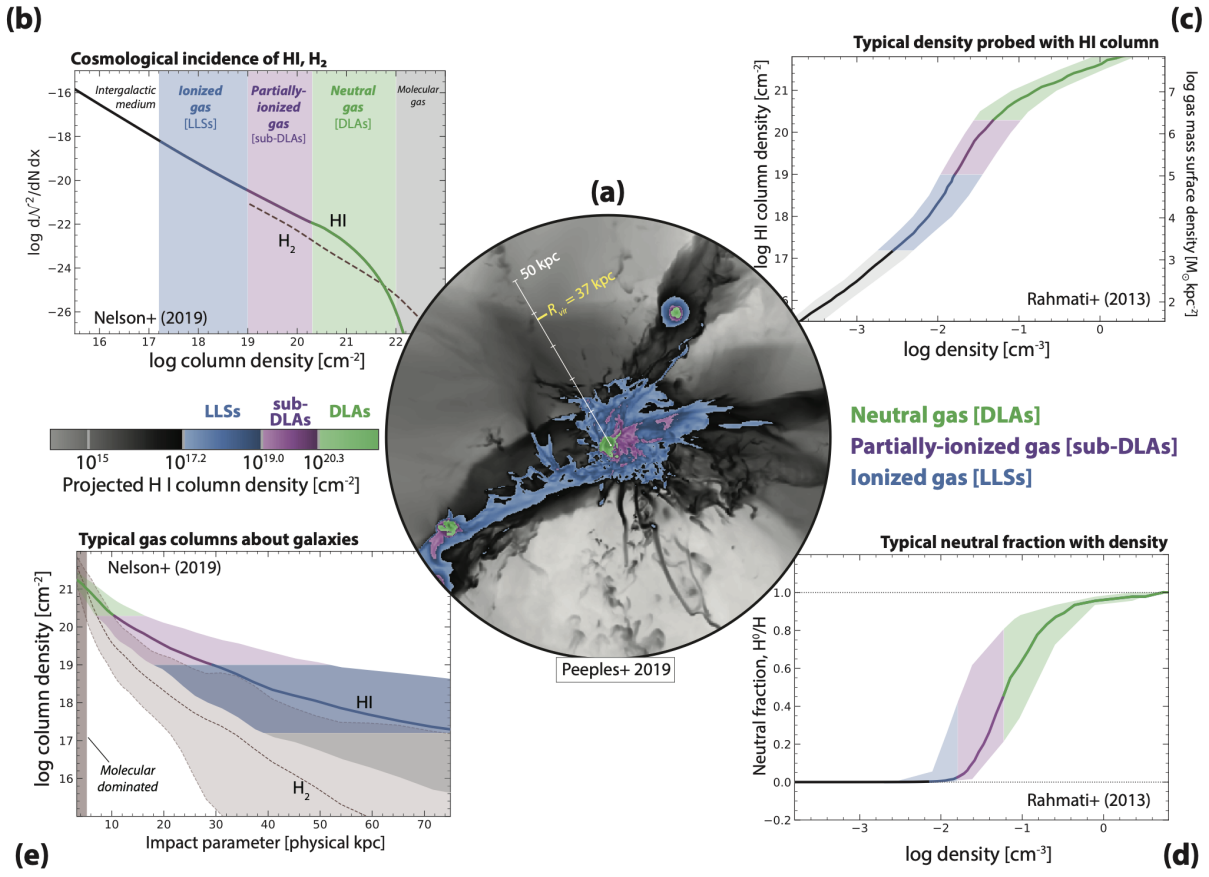

Figure 1.2: Characteristics of the cold gas around simulated galaxies at redshifts 2 to 3. Panel (a) (central image) shows column densities of a halo that will turn into a Milky-way-mass system at redshift z=0. HI color densities are shown on the middle left color-coded, and their description in middle right. Panel (b) shows cosmological column density contribution of each component (Nelson et al., 2019). Panel (c) shows the typical column density of HI as a function of total particle density (Rahmati et al., 2013). Panel (d) shows the typical neutral fraction of the gas with density as a funcion of particle density (Rahmati et al., 2013). Panel (e) shows the typical gas column density of HI and HII as a function of projected distance in physical kpc (Nelson et al., 2019). Image Ref: (Péroux and Howk, 2020).

The warm gas with T $< 10^{5-6}$ K that can also be traced by far-UV absorption lines like NeVII, NV, OVI, CIV, becomes much harder to estimate due to the uncertainties in ionization mechanisms (Tumlinson et al., 2017). For example, partial photoionisation of OVI could be adding fractions of T $< 10^4$ K gas that have already been accounted for in the colder phase. In addition, to reproduce the observations of this gas in simulations, the temperature range of models needs to be narrowed down, for example the mentioned OVI line has to be narrowed to $< 10^{5.3-6.6}$ K (Werk et al., 2016).

The hot T $> 10^6$ K phase properties of the CGM are different in different types of galaxies, and can be studied through X-Ray observations using state-of-the art instruments like Chandra, XMM-Newton and eROSITA, or through the Sunyaev Zeldovich effect with telescopes using microwave maps (e.g. Planck, SPT, AcT). The hot gas can be detected in absorption in the Milky Way, and in emission only in very massive galaxies (Lim et al., 2021). State of the art cosmological simulations like Illustris-TNG (Nelson et al., 2018; Pillepich et al., 2018), Magneticum (Dolag et al., 2017), EAGLE (Schaye et al., 2015), can test this gas at different temperatures. In Figure 1.3 we show a comparison of this hot gas from different observations at this temperature range. Future X-ray missions with high-resolution spectroscopic capabilities, like XRISM (XRISM Science Team, 2022), Arcus (Heilmann et al., 2022), and Athena (Nandra et al., 2013), will revolutionize further the CGM science.

The IGM at intermediate redshifts ($z \sim 2-5$) has a density and ionization state that can be probed near the mean cosmic density through HI Lyman α forest (Meiksin, 2009). These, together with associated metal lines, can be observed using ground-based optical telescopes, as the most relevant lines are redshifted in the optical band.

Observations of the IGM in the higher temperature range $> 10^{5-6}$K and at lower redshifts z < 2 show that the gas is more diluted and diffuse than at higher redshifts, while simulations show that a large percentage of the gas has been shock heated to high temperatures T $> 10^{5-7}$. The WHIM is the dominant baryon contributor at low redshift and is located mostly in filaments and knots along the cosmic web, in which groups and clusters also reside (Martizzi et al., 2019). Observing the WHIM remains a challenge (Bertone et al., 2008; Frank et al., 2010; Augustin et al., 2019; Wijers et al., 2020), nevertheless this gas in emission has been successfully detected in a filament of the famous galaxy of M87, where an emission of FeXXI (λ1354 Å) in X-Ray at T $> 10^7$ K was found (Anderson and Sunyaev, 2018), as shown in Figure 1.4. There are other claims of WHIM detection in emission (Werner et al., 2009; Reiprich et al., 2021) as well as in absorption (Fang, 2010; Nicastro et al., 2018).

1.1.4 Open Questions in the field of CGM relevant for this work

The remaining questions about the CGM are 1) which different phases contribute to the CGM? 2) which objects are associated with to the CGM? Observations still rely on a number of assumptions and models that await confirmation. Another major observational challenge is the metallicity and total gas content of the highly ionized phase of the gas. The process of dust production and destruction, key ingredients to star formation, needs a better

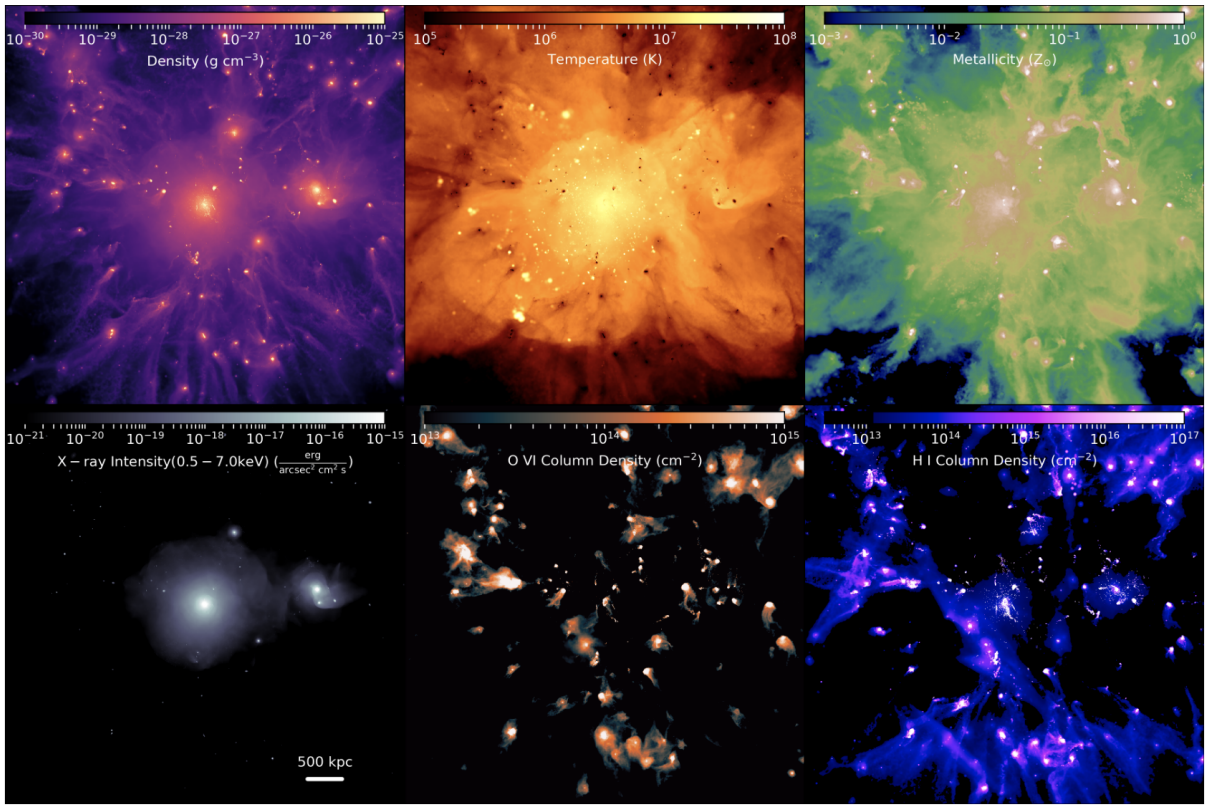

Figure 1.3: Snapshot of the ROMULUS simulation of the ICM, in a 5 x 5 Mpc cut of density-weighted projections of gas density, temperature and metallicity on top. Integrated X-ray intensity, O VI column density and H I column density in the bottom. The image shows that the clusters outskirts and small-scale structure is better traced with UV absorption studies (O VI and H I), compared to X-ray emission (Butsky et al., 2019).

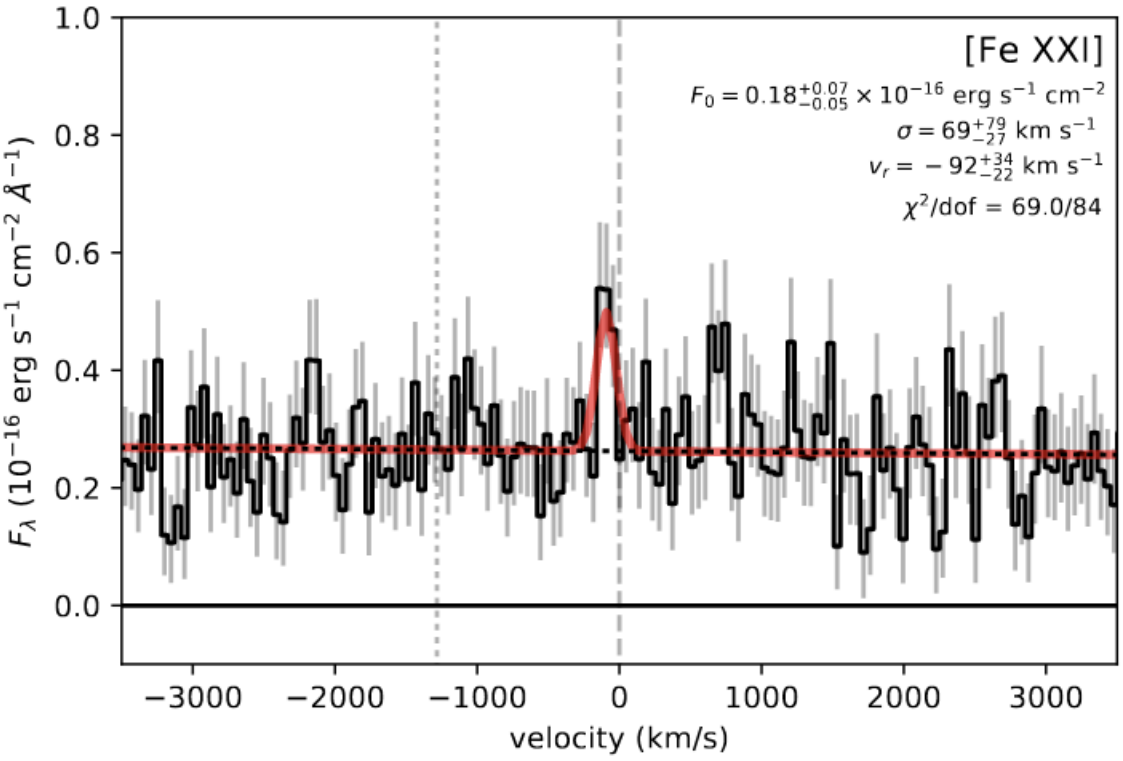

Figure 1.4: Detection of FeXXI in emision in X-ray wavelength of a filament of M87 galaxy (Anderson and Sunyaev, 2018).

in-depth understanding. Most importantly, the CGM gas might have been detected in its hot phase in emission (Anderson and Sunyaev, 2018), while other detections of absorption remain controversial (Nicastro et al., 2018). New results from FOGGIE (Figuring Out Gas Galaxies in Enzo with exquisite spatial resolution in the CGM) simulations show that the CGM is a multiphase gas (Lochass et al in prep), the filaments are cooler than the rest of CGM but heat up toward the center, which may cause their disruption. And further away from CGM the cooler the gas may be, so that it could be trace by cool clouds of the common DLAs.

1.2 Clusters of galaxies

Among the most massive objects in the Universe are galaxy clusters and superclusters (Peebles, 2020), where galaxies are held together by the gravitational potential. Galaxy clusters also make it possible to test models of gravitational structure formation, galaxy evolution, thermodynamics of the intergalactic medium, and plasma physics (Kravtsov and Borgani, 2012). Even considering the presence of AGN, and gravitational shock heating, the size and depth of the gravitational potential would allow the clusters to retain their initial baryon fraction on these large scales (Voit, 2005). This makes galaxy clusters a possible reflection of the universal fraction of baryonic to dark matter, and are thus perfect laboratories to test cosmological models of our universe.

1.2.1 Physical characteristics

Clusters of galaxies have three major components: galaxies, intracluster gas, and dark matter, the last being the dominant component (83% to 90%). Out of the remaining baryonic matter, the majority resides in the X-ray emitting hot intracluster gas (up to 15%). The rest of the baryons are in the luminous galaxies and in isolated stars which comprise the faint and diffuse intra-cluster light ($\sim 2\%$) (Laganá et al., 2013). The large reservoir of hot gas makes clusters prominent sources that can be easily traced by X-rays; they can also be studied using the SZ effect through the interactions of the CMB with the hot intra-cluster medium (ICM). Observations in the optical band can be used to study the luminosity of the galaxies, and infrared photometry can be used to study the intracluster light (ICL). In addition, the deep gravitational potential of clusters causes gravitational lensing, which can also be used to study the clusters via the distortion of the light from background sources.

1.2.2 Structure

Clusters can be classified according to their structure: Regular clusters, which are approximately circularly symmetrical with a central mass concentration, where most of the members are either elliptical or early type spirals (SOs) (Kravtsov and Borgani, 2012); and

Irregular ones, with a poorly defined structure, and where most of the members are spiral galaxies.

On the other hand, Bautz Morgan (B-M) defined a classification scheme based on the brightest galaxy in the cluster (Bautz and Morgan, 1970). Massive galaxies at the center of the cluster can merge as a result of dynamical friction. The movement of galaxies within the cluster produces an asymmetrical distribution of galaxies and dark matter, because the gravitational force produces friction which slows the orbital motion. The larger the mass of the galaxy, the faster the slowing rate, since deceleration is a function of galaxy mass. This causes the largest galaxies to end up in the center, these central objects are called Brightest Cluster Galaxy (BCG) or sometimes cD (central Dominant) galaxies (Giacintucci et al., 2007), with rotational symmetry after the Yerkes classification (type I cluster from B-M). There can also be more than one BCG per cluster (type II B-M). However, not all clusters host a giant galaxy at the center (type III B-M). The clusters with cD galaxies, or relaxed galaxy clusters, have reached dynamical equilibrium, and baryonic processes are balanced with the gravitational forces, while unrelaxed clusters are still in the process of formation and are not gravitationally stable (Mantz et al., 2015). These processes lead to velocity dispersion that deviate from simple gaussian distributions, which are possibly reflected by the new observational results presented in Chapter 3.

Clusters also differ depending on their size, where the small mass clusters can have almost equal amount of cold and hot gas (Sanderson et al., 2013). Another difference is that not all clusters have an ICL component. Even if it does not contribute greatly to the overall mass budget, the ICL can become more important in lower mass systems as well. In the lowest mass halos where the feedback can be more influential, the hot gas may have been displaced to outskirts or ejected completely from the halo altogether. The cold gas in these systems can also be in between intracluster stars, where the low surface brightness and diffuse nature makes it harder to detect (Sanderson et al., 2013).

Another difference between cluster samples is found in temperature profiles of galaxy clusters where we can differentiate between cool cores and non-cool cores clusters. While the cool-core clusters are defined as having low central entropy and a systematic temperature drop, the non-cool core clusters have high central entropies (Hudson et al., 2010). There is also a middle category of weak cool-core types, which have a flat temperature profile or slight decrease towards the center, with enhanced central entropy.

1.2.3 Intracluster Medium

The bulk of the baryonic matter in clusters resides in the hot Intracluster Medium (ICM), where the gas is not directly associated with the individual galaxies that are part of the cluster, but the properties of the individual galaxies are still correlated to the hot ICM of the clusters. The ICM seems to be near equilibrium with the galaxies within a common gravitational potential well due to the consistency of the gas temperature with the galaxies velocities (Kravtsov and Borgani, 2012).

Most of the ICM is of course made up from the most abundant element in the universe, Hydrogen (electrons and protons), and small amount of Helium. The average abundance

of heavier nuclei is about one-third of that of the Sun, which are related to the Type Ia and core-collapse supernovae that enriched the ICM environment (Mernier et al., 2018). The abundance of these heavier elements is still uncertain due to the inhomogeneity of the ICM gas (Mernier et al., 2018). This inhomogeneity has been linked to be ubiquitous motions generated by the structure formation processes of galaxy formation, as hydrodynamical simulations have shown (Dolag et al., 2005; Battaglia et al., 2012; Ryu et al., 2003). The more inhomogeneously distrubuted the metals are, the less accurate the metallicity measurements can be according to simulations of galaxy clusters. Metal mass obtained by X-ray observations can be underestimated to up to three times in the inner regions of R_{500} (Kapferer et al., 2007). Additional gas motions in cluster cores have been linked to radiative cooling and feedback from stars and AGN. Apart from case of mergers with a sub-cluster or an infalling galaxy into host clusters, the energy input of a supermassive black hole in the cores of clusters is probably the dominant cause of gas perturbations (Simionescu et al., 2019).

In order to understand cluster formation, the thermodynamics of the ICM in comparison with models is key. Multiwavelength measurements (X-ray, optical, weak lensing, and radio) of cluster properties require significant resources for large cluster samples, although some wavelengths probe some properties better than others (Figure 1.3). Scaling relations play an important role by constraining ICM physics and theoretical models based on gravitational collapse, through comparison with observables. The most popular assumption is the self-similar one (Kaiser, 1986), where clusters are simply scaled down versions of each other, and gas density at a given fraction of radius is independent of cluster mass. Nevertheless new models and observations have shown significant deviations from this initial simple assumption.

Due to the high temperatures of the hot plasma, the ICM emits primarily in X-rays through thermal Bremsstrahlung. In addition to Bremsstrahlung, recombination and line emission can be important. For a given density, the spectra are determined by the temperature and the abundance of heavy elements, which can be estimated by fitting models to observed X-ray spectra. Deep X-ray observations of bright galaxy clusters with XMM-Newton and Chandra (Gatuzz et al., 2022) revealed a 2D mapping of the ICM distribution of metals, which demonstrated that only a modest amount of the total X-ray emission relates to gas cooled down to lower temperatures. Consistent with low star formation rates on BCGs, the cooling down of cluster cores is prevented by a heating mechanism that compensates for radiative losses (McDonald et al., 2011). The outskirts of clusters have characteristically lower X-ray surface brightnesses. The previously mentioned instruments are affected by particle background, so that Suzaku satellite, with its high spectral resolution, provides the best abundance measurements at large radii (Werner et al., 2008). Along with the remarkable results from Hitomi satellite (Matsumoto et al., 2018), these instruments set the ground for measuring elemental abundances in the ICM.

Nowadays, the extended ROentgen Survey with an Imaging Telescope Array (eROSITA) (Merloni, 2012; Predehl et al., 2021) is providing an increasing amount of statistical power observing the largest number of x-ray sources compared to previous instruments like Chandra observatory (Weisskopf et al., 2000), Newton-XMM (de Chambure et al.,

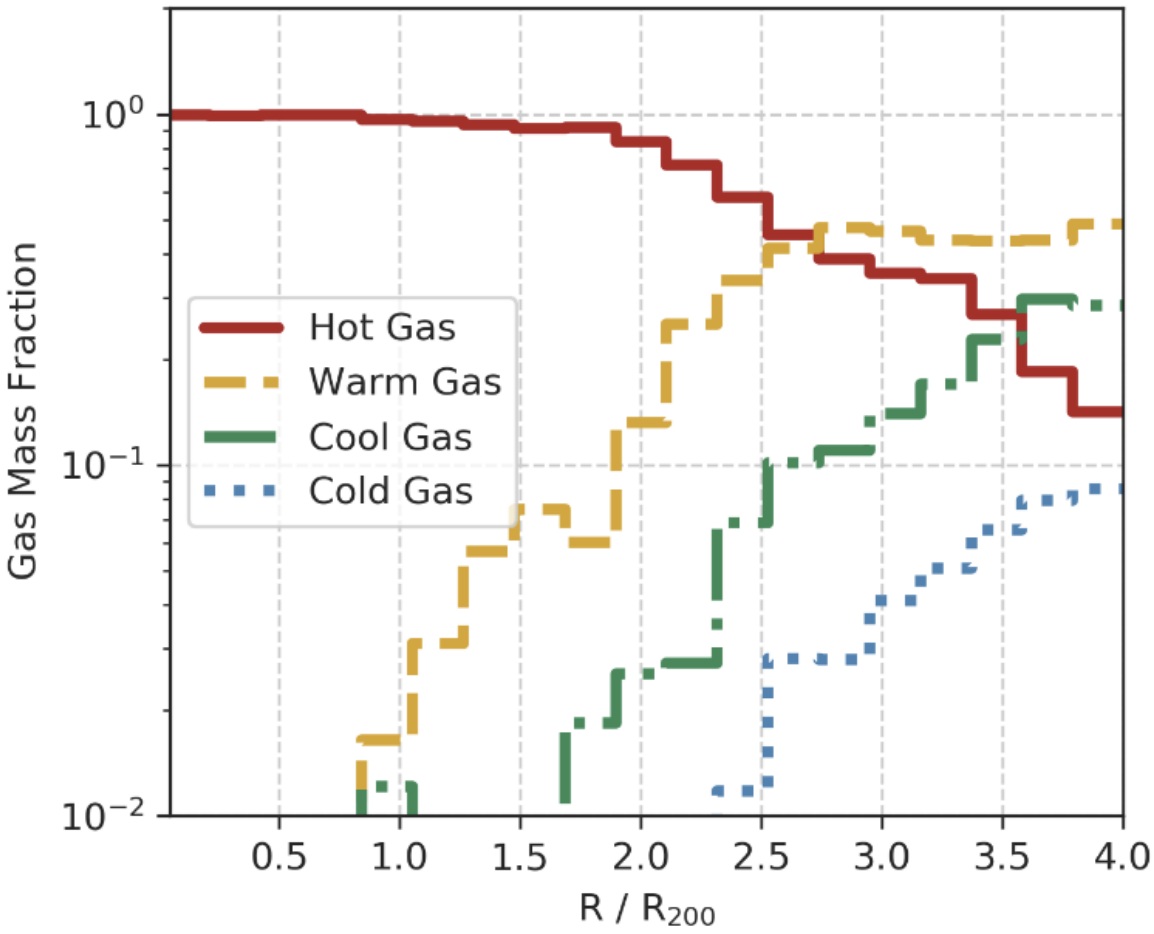

Figure 1.5: Gas mass fraction of hot($T > 10^6$ K), warm($10^5 <$ K $T < 10^6$ K), cool ($10^4 <$ K $T < 10^5$ K) and cold gas ($T < 10^4$K) in galaxy clusters, as a function of radius in R200. (Butsky et al., 2019)

1999) or ROSAT (Voges, 1992) satellites. With more than ∼500 clusters observed in the eROSITA Final Equatorial Depth Survey (eFEDS) (Bahar et al., 2022), the satellite has provided X-ray properties for clusters and groups, improving current constrains on scaling relations probing mass and redshift of galaxy clusters (Chiu et al., 2022). In the future, the X-ray imaging and Spectroscopy mission (XRISM) (Williams, 2022), Athena (Nandra et al., 2013) will further improve our current knowledge of the ICM enrichment, while measuring radial profiles of the gas velocity dispersion and bulk velocities, and probing velocity amplitudes and scale (Zhuravleva et al., 2012).

1.2.4 Open Questions in the field of Clusters relevant for this work

The gas deficit and low star formation rate in galaxy clusters, the existence of a massive central galaxy and its properties, the missing baryons in galaxy clusters related to the λCDM baryon distribution expectations in the universe, are just a few of the unanswered questions regarding this field. Studying galaxy clusters allows us to more accurately describe our universe, shedding light on the thermodynamics and energetics from the growth of the large-scale structure, setting important constraints on energy sources and their interplay with the ICM and IGM and even smaller scale structures. Both simulations (Nelson et al., 2020) and observations (Anand et al., 2022; Mishra and Muzahid, 2022) also show that cold gas exists in small mass galaxy clusters. But on bigger masses, the ICM is mostly detected by their hot ICM in X-rays. Does the cold gas exist in high mass clusters as simulations seem to show (see e.g. Figure 1.5), and if so, what is the fraction? These are the main subjects to address in future research, and will be subject of Chapter 3 of this thesis.

1.3 Active Galactic Nuclei

There is by now general agreement that all massive galaxies contain a supermassive black hole (SMBH) that is powered by infalling matter, and have masses of $10^6 - 10^{10} M_\odot$ (Rees and Mészáros, 1998). Early observations of quasi-stellar objects (quasars or QSOs) in the early 1960s already indicated that these objects must be very distant, and that they had to be much smaller than galaxies but produced immense energies that power the observed optical emission and radio lobes. The only viable source for such energies was later proved to be accretion of interstellar gas into SMBHs (Murray et al., 1995). AGNs play a major role in the final stellar mass of the bulge, and the evolution of the host galaxy overall.

1.3.1 Definition and basic properties

Quasars are better defined as as processes rather than objects, they can be explained as what happens when the central black hole at the centers of massive galaxies are actively accreting new material (Lynden-Bell, 1969). These main features of the galaxies with accreting SMBHs called "active galactic nuclei" (AGN), distinguishes them from normal galaxies whose SMBH is not active by a display of differences in their basic spectroscopy and emission of jet like structures.

Some of the properties of the AGNs include the following (Netzer, 2015) :

- X-ray emitting corona, on scales of tens of gravitational radii.
- An accretion disk: subparsec rotation dominated accretion flow.
- Broad line region: high density, dust-free cloud regions moving at roughly Keplerian velocities.

- Central torus: an axisymmetric dust structure, on scales of 1-100 parsecs.
- Narrow line region: lower density, lower velocity outflows ionised gas.
- Thin molecular maser disk.
- Central radio jet.

1.3.2 AGN classification

There are several classification schemes for AGN that are based on high-quality observations of a large number of sources and a better understanding of the physics involved in accretion and line-emitting processes. The aspects of AGN structure revealed they are not different objects, but different manifestations of the same structure. This is called unification theory of AGN (Rowan-Robinson, 1977), and their classification can be based on orientation of the structure under what is referred to as the standard unification model. Nowadays the classification of AGN are almost entirely based on observational characteristics of the AGNs, such as the intensity of equivalent width of emission lines, the level of ionization of the line-emitting gas, the strength of the radio and X-ray source, evidence for non-thermal radiation or central obscuration, variability amplitude and time scale, among others. Here we describe the clasiffication scheme described by Netzer (2015).

- Type-I AGNs: In earlier years known as Seyfert 1 galaxies and radio-quiet QSOs, these AGNs are characterized by a blue Optical/UV continuum and by broad permitted (or semi-forbidden) emission lines, high ionization narrow emission lines (many of which are forbidden lines). The central point source shows no obscuration and is visible at all wavelengths. At the same time there can be subgroups that have characteristic intensities between narrow and broad components of Balmer lines, or being radio-loud, aka Broad Line Radio Galaxies (BLRGs).

- Type-II AGNs: Also known as Seyfert 2 galaxies, they have a completely obscured line of sight to the center. They show strong and narrow near infrared (NIR), optical and UV emission lines, which are indicative of photoionization by a non-stellar source. Like the type-I AGNs, the type-II also show a point X-ray source associated with the galactic nucleus, and they can also be divided into subgroups between radio quiet and radio loud (Narrow Line Radio Galaxies - NLRGs).

- Low Ionization Nuclear Emission-line Regions (LINERs): Also referred to as low-luminosity AGNs (LLAGNs), they represent up to one-third of all galaxies in the local universe. As the name suggests, they are characterized by low-ionization, narrow emission lines from ionized gas of nonstellar origin. These LINERs can also be divided into subgroups of broad emission lines (type-I LINERs) and only narrow emission lines (type-II LINERs) (Ho, 2008). Their spectral energy distribution (SED) are markedly different from high luminosity AGNs, where the pink line representing the

LINERs continuum emission follows a self-absorbed synchrotron spectra with a very steep IR-to-UV power-law slope.

- Lineless AGNs: There is a sub-population of AGNs with extremely weak, often undetected emisison lines. Sometimes also refered to as anemic AGNs, or dull AGNs (Netzer, 2015), they cover a large range of luminosities, from very faint to very luminous, with a non-stellar continuum and an observed X-ray point source which is a clear indicator for the active black hole. This category also includes BLLacs.

- Blazars and radio loud AGN: This group includes highly variable core-dominated radio-loud sources that show polarization both in optical and radio wavelengths. They can also be powerful gamma ray emmitters and could have one or more of the following: intense, highly variable high-energy emission in gamma-ray and radio; radio, X-ray and gamma-ray jets with relativistic motion; double-peaked SED with lower-frequency peak at radio to X-ray energies, and high-frequency peak at X-ray to gamma-ray.

1.3.3 Absorbers

Intrinsic

As mentioned in previous sections, AGN involve many physical processes. The standard unification scheme can explain both the properties of the emission lines and the absorption lines by the obscuring torus (Lawrence and Elvis, 1982), and it dependance on the viewing angle. Outflows launched by the accretion disk may also play an important role in the host galaxy's evolution. According to models, these outflows can start deep inside the central engine, and can be launched outside the accretion disk (Everett, 2005; Proga and Kallman, 2004). The winds remaining at high latitudes are low-density and highly ionized, while most of the rest of the material stays at low-latitude. In between these two phases, filaments of dense gas might form in the shape of mini broad absorption lines (BALs) or narrow absorption lines (NALs). In the low-latitude, the gas remains predominantly warm and weakly ionised, with a broad range of velocities which could potentially form broad absorption lines (BALs) (Culliton et al., 2019).

Absorption lines which are physically associated to quasars are called "intrinsic" (Hamann and Sabra, 2004). The chances that BALs or mini-BALs are from intervening objects or the ISM are very low, so they are attributed to be intrinsic to the quasars. NALs on the other hand can be associated to the IGM, ISM, or gas from the galaxies' disk winds mixed with quasars host galaxies' ISM (Ganguly and Brotherton, 2008).

Intervening

In the case the absorbers are clouds of gas distant from the emitting quasar and unrelated to it, they are called "intervening" absorbers. These are numerous, and can provide fundamental information about the CGM and IGM from redshifts 0 to beyond 5. They can be

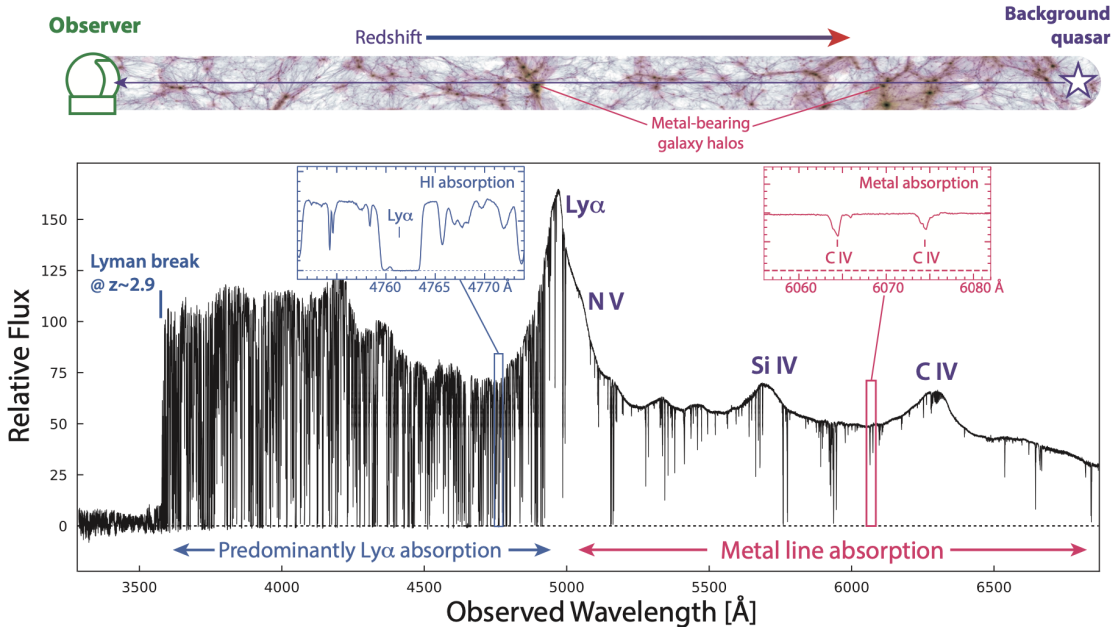

Figure 1.6: On the top of the figure we show another schematic of the technique used to observe the metals through absorption, using quasars as a background source. The darker areas represent the galaxy halos and filaments of the IGM. The bottom panel shows a sample of a high-resolution spectrum of a high redshift (z$\sim$ 3) quasar from UVES, VLT with a very high SNR and spectral resolution. At those wavelengths, the Lyα features dominates the spectra in emission. There are also many absorption features, where below 5000$\AA$ is mostly HI, and above that wavelength is mostly metal lines. Image ref: (Péroux and Howk, 2020)

divided in three groups according to the strength of the absorption: The strongest absorption is related to column densities of neutral hydrogen clouds with N(HI)$> 10^{20}\text{cm}^{-2}$ (Wolfe et al., 1986). These are called Lyman alpha (Lyα) systems, and comprise the majority of the neutral gas reservoir in the Universe used for the initial phase of star formation (Péroux and Howk, 2020). Their profile is shown in Figure 1.6. Often related to the CGM of a galaxy, or a filament of the IGM, they can also show lines of heavier and hotter elements.

The intermediate absorption systems are associated with neutral hydrogen column densities of $\sim 10^{17}\text{cm}^{-2}$, with traces of heavier elements as well, and are believed to have originated from the halos of galaxies.

The low column density systems are the most numerous and common, with column densities of $\sim 10^{12}\text{cm}^{-2}$ of neutral hydrogen gas clouds. They are referred to as the Lyα forest, since they are seen polluting the spectrum in the shorter area of the Lyα emission area, and are closely related to the IGM.

1.3.4 Open Questions in the field of AGN relevant for this work

Models of the AGN tori, disk wind models and their parameters still require adjustments. Although hydrodynamical simulations are more promising, they still do not include all processes and generally are limited to AGN with small BHs. The unification scheme in its simplest form does not seem to be able to explain black hole evolution, which makes it clear it required several major revisions. AGN radiative feedback and its role needs very high spatial and spectral resolution in order to be better understood, and new instrumentation, such as the James Webb Space Telescope, will continue to give us new fundamental constraints on these complex processes (Ford et al., 2014; Yung et al., 2021). Chapter 4 offers new insights into intrinsic properties of AGN by studying intrinsic outflows of a large sample of objects.

1.4 Instruments

In order to study multiphase baryon cycle in large quasar surveys, this work combines the use of multiple facilities. Earth's atmosphere presents a major challenge when it comes to energies around Ultra Violet (UV) and higher, infrared, and long radio wavelengths. Ground-based telescopes are then only ideal at a certain range of the electromagnetic spectrum. That is when exploring the universe becomes dependent on high altitude rockets or airplanes, satellites or balloons. In this section we will focus on the instruments that were used for in this thesis.

1.4.1 Very Large Telescope - Ultra Violet Echelle Spectrograph

The Very Large Telescope (VLT) (Dekker et al., 2000) is an optical observatory, operated by the European Space Observatory (ESO) in the Atacama desert, Paranal (Chile). The VLT is made up of four major telescopes with primary mirrors of 8.2m diameter each, plus an

additional four movable 1.8m mirror telescopes. When used together for interferometry, the four primary telescopes can reach very high angular resolution (0.002 arcseconds). Operating at visible and infrared, and equipped with more than 15 different instruments between adaptive optics corrected cameras and spectrographs, high-resolution and multi-object spectrographs, covering a broad range of wavelengths from UV (300nm) to mid-infrared (24μm).

One of the instruments used in this work is the cross-dispersed echelle spectrograph called Ultra Violet Eschelle Spectrograph (UVES) (Werner et al., 2009), mounted on the Nasmyth's platform (a Cassegrain like modified telescope) on the Unit Telescope 2 (UT2, Kueyen). UVES has two separate blue (UV to blue: λ 300 to 500 nm) and red (λ 470 to 11000 nm) arms with two CCD detectors. The resolving power reaches 40,000, although with adequate sampling using narrow slits the blue arm can achieve up to 80,000 and the red arm up to 110,000. UVES is key to this work because of the combination of ultra-violet coverage, high spectral resolution, and hundreds of quasar spectra observed and available in the European Southern Observatory archives.

1.4.2 Sloan Digital Sky Survey

The Sloan Digital Sky Survey (SDSS) uses a 2.5m wide-angle optical telescope located at the Apache Point Observatory (APO) Sunspot in New Mexico, United States. It is a modified Ritchey–Chrétien telescope (also modified Cassegrein telescope), equipped with a complimentary by three subsidiary instruments: a large hyperbolic secondary mirror, the Photometric Telescope (0.5m aperture) equipped with a filter and a CCD camera, a seeing monitor and a cloud scanner (Gunn et al., 2006). The imaging camera is made out of 60 CCD in 5 rows, where each row has an optical filter named u, g, r, i and z with average wavelength of 355.1, 468.6, 616.5, 748.1 and 893.1 nm respectively. The spectrograph on the other hand, covers a wavelength range of 3,800 to 9,200 Å at a resolution of 2,000, operates with an aluminium plate with drilled holes where individual optical fibers fit. The holes are specially targeted to specific areas of the sky, so each area requires a different plate. Starting the observations in the early 2000s as a major multi-imaging and spectroscopic redshift survey, it has evolved in five different major phases.

Relevant for the work presented here, as part of the eBOSS survey the SDSS-IV program also included a dedicated followup program of All-sky X-ray sources (clusters and AGN), called SPIDERS. The ongoing phase of SDSS (SDSS-V) is an all sky, multi-epoch spectroscopic survey targeting over six million objects. By systematically monitoring the whole sky spectroscopically, it will be able to reveal changes ranging from 20 seconds to 20 years, tracking the evolution of massive black holes at the center of galaxies. Designed also for tracking the history of the Milky Way, tracing the emergence of chemical elements, unvealing details of the origin of planets, and creating a spectroscopic map of the gas in the Galaxy and the Local Group (Kollmeier et al., 2017), and will continue to multiply the scientific output of major space missions like eROSITA and GAIA.

1.4.3 eROSITA

Moving to X-ray wavelengths, the latest and newest X-ray satellite telescope extended ROentgen Survey with an Imaging Telescope Array (eROSITA) was launched in 2019 as the primary instrument on board the Russian-German "Spectrum-Roentgen-Gamma" (SRG) mission (Predehl et al., 2021; Merloni, 2012). The X-ray instrument was developed and built by the Max Planck Institute for Extraterrestrial Physics (MPE), and is part of the Russian–German SRG space observatory, which also carries the Russian Astronomical Roentgen Telescope X-ray Concentrator (Mikhail Pavlinsky ART-XC). eROSITA is a successor of the Röntgen satellite (ROSAT) launched in 1990, which gave the first all-sky survey in X-ray of more than 130,000 objects, until after an extra four years of operations on top of the planned five year duration led to the end of the mission. The eROSITA instrument operates in a energy range of 0.2 up to 8.0 keV, with 7 Wolter-1 type mirror modules, each containing 54 nested golden-coated mirror shells. Being $\sim$ 20 times more sensitive than ROSAT satellite in the soft-energy range (0.2 to 2.0 keV), and creating the first time all-sky survey in X-ray hard band. With the first science results released in July 2021 (EDR), the satellite has already completed four of the planned 8 full-sky surveys, the first image of the first full-sky survey is shown in Figure 1.7.

1.5 This Thesis

Using absorption line spectroscopy from background sources such as distant quasars (Figure 1.8), we can study the elusive and diffuse gas that cannot be observed through emission. The goal of this work was to target the IGM, ICM and the environment of the AGNs at optical and UV wavelengths, serching for weak absorption lines in stacked optical/UV spectra from large samples of sources.

In Chapter 2 we study the IGM with data from the VTL-UVES. Using $\sim$ 500 fully reduced, continuum-fitted quasar spectra (Murphy et al., 2019), we select 155 identified Damped Lyman-α Absorbers (DLA) (Murphy et al., 2019) found in the line of sight. Using the stacking technique at the redshift of these known absorbers, we target the FeXXI line in absorption as a tracer of high-redshift 10^7K Warm Hot Intergalactic Medium (WHIM) gas. We place upper limits on the column density of the hot gas associated to DLAs, and provide an assessment of how large samples from future experiments can be used to further constrain WHIM models.

In chapter 3 we use quasar spectra from SDSS, with spectroscopically confirmed clusters compiled from the from the SPectroscopic IDentification of EROSITA Sources (SPIDERS) program (Clerc et al., 2016, 2020; Kirkpatrick et al., 2021a; Ider Chitham et al., 2020). Using the same stacking technique, we search for cold gas in the ICM using MgII doublet as a tracer of this 10^4K gas.

In chapter 4 we investigate the environment around AGNs, and focus on the intrinsic MgII doublet absorption occurring on top of the emission associated to the AGNs in a sample of X-ray selected AGN from the first eROSITA Performance Verification survey.

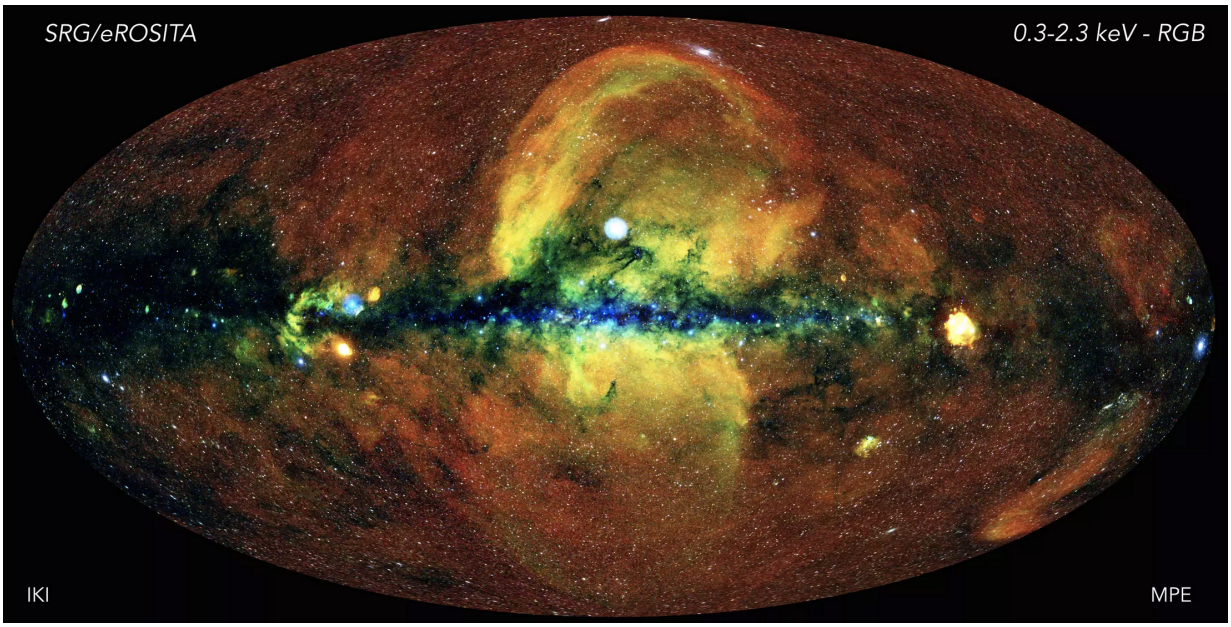

Figure 1.7: After 182 days of observation, the eROSITA completed the first full sky map of the hot, energetic universe. The emission of the hot gas in the vicinity of the solar system can be seen as a red diffuse glow outside of the plane of the galaxy. The plane shows in blue the high energy X-ray photons, that have enough energy to go through the dust and gas absorption at lower energy levels. The green and yellow in the centre of the galaxy show history of recent energetic processes driving gas out of the plane of the galaxy (Image credit: Jeremy Sanders, Hermann Brunner and the eSASS team (MPE); Eugene Churazov, Marat Gilfanov (on behalf of IKI).

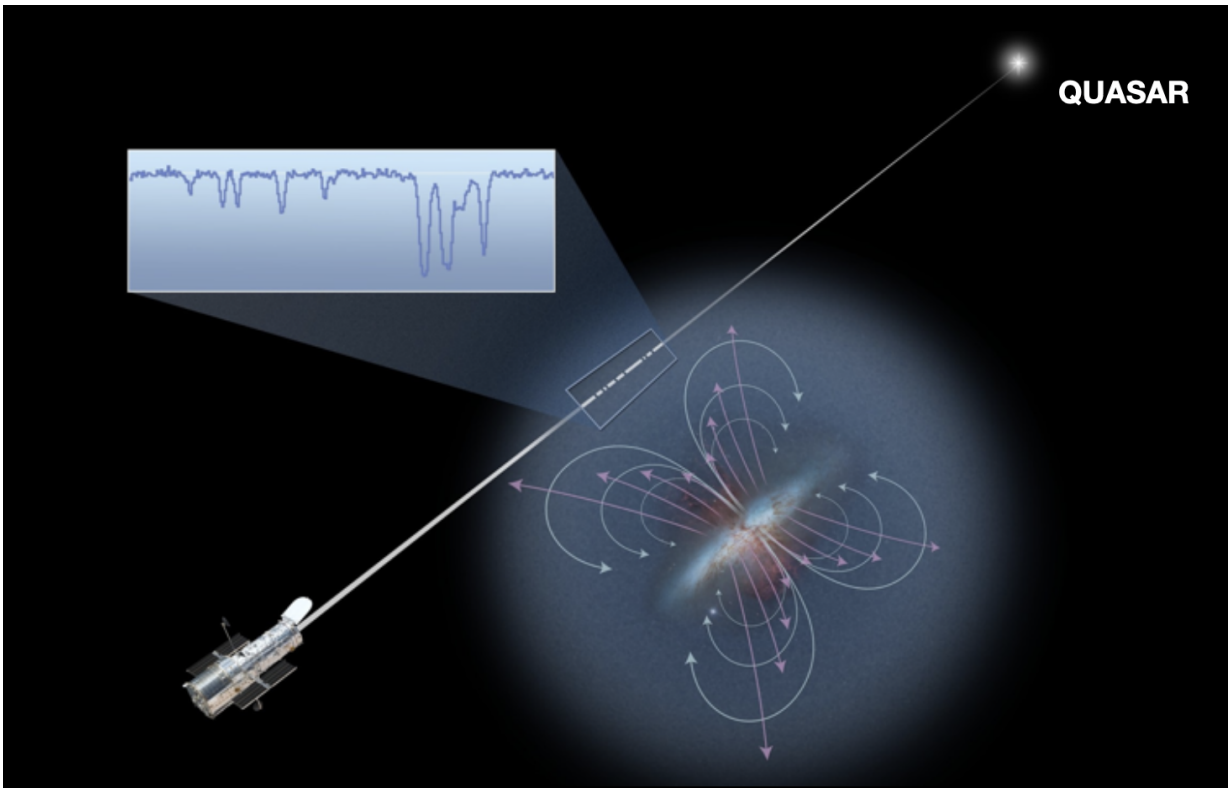

Figure 1.8: Technique used throughout the projects developed in this thesis, using AGNs as a background source, but instead of satellites (as seen in the image) we used ground telescopes. Image credit: NASA; ESA; A. Feild, STScI.

In chapter 5, we summarise the work developed throughout this thesis and discuss the possible future work that could be done to further expand our knowledge in these areas.

Chapter 2

WHIM Tracers at UV-wavelengths Tracing the 10^7 K Warm-Hot Intergalactic Medium with UV absorption lines

The contents of this chapter have been published in Fresco et al. (2020) Monthly Notices of Royal Astronomical Society

Abstract The majority of the cosmic baryons in the low redshift Universe are not observed directly, leading to the so-called "missing baryons" problem. Probing the missing baryons is essential to constrain the accretion and feedback processes which are fundamental to galaxy formation. Cosmological hydrodynamical simulations have indicated that a significant portion of them will be present in a Warm-Hot Intergalactic Medium (WHIM), with gas temperature ranging between 10^5–10^7K. While the cooler phase of this gas has been observed using O VI and Ne VIII absorbers at UV wavelengths, the hotter fraction detection relies mostly on observations of O VII and O VIII at X-ray wavelengths. Here, we target the forbidden line of [Fe XXI] λ 1354Å, which traces 10^7K gas at UV wavelengths, using more than one hundred high-spectral resolution (R$\sim$49,000) and high signal to noise Very Large Telescope (VLT)/UltraViolet Eschelle Spectrograph (UVES) quasar spectra, corresponding to over 600 hrs of VLT time observations. A stack of these at the position of known Damped Lyman Alpha systems lead to a 5-σ limit of log[N([Fe XXI])] <17.4 ($EW_{rest} < 22$mÅ), three orders of magnitude higher than the expected column density of the WHIM log[N([Fe XXI])] <14.5 for the WHIM component. This work proposes an alternative to X-ray detected 10^7K WHIM tracers, by targeting faint lines at UV wavelengths from the ground benefiting from higher instrumental throughput, enhanced spectral resolu-

tion, longer exposure times and increased number of targets compared to what is currently available in X-rays. The number of quasar spectra required to reach a column density that could be detectable with future facilities including 4MOST, ELT/HIRES and the Spectroscopic Telescope appears challenging. Considering all possible instruments, our calculations of number of spectra needed to achieve the detection of this gas show that the only plausible instruments that could attempt to detect hot gas via UV spectroscopy are MSE and/or Spectroscopic Telescope.

2.1 Introduction

The Standard Cosmological model predicts that the vast majority (more than 95%) of the matter is in the form of Dark Energy and Dark Matter. Only the remaining ≈4% is in the form of baryons, the normal matter which makes up stars and galaxies. The total baryon density of the Universe, $\Omega_{\rm baryons}$=0.0455 (Komatsu et al., 2011), is in fact well constrained from measurements of Cosmic Microwave Background (CMB) anisotropies, light element abundances coupled with Big Bang nucleosynthesis (Cooke and Fumagalli, 2018) and, in the near future, from observations of dispersion measures (DM) of Fast Radio Bursts (FRBs) (Qiang and Wei, 2020; Macquart et al., 2020). We note that results from these different experiments involving vastly different physical processes and observation techniques agree remarkably well (±0.005). However, 30 to 50% of the baryonic matter is not observed directly today (Persic and Salucci, 1992; Nicastro et al., 2018; Peroux and Howk, 2020). The latest baryon census shows that galaxies, groups and clusters together comprise only $\sim$ 10% of the expected baryon density (Salucci and Persic, 1999; Bregman, 2007; Shull et al., 2012; Nicastro et al., 2018; de Graaff et al., 2019a). Recently, a fraction of these baryons $10^5 - 6$K were found on the scales of the galaxy haloes, including in the Circumgalactic Medium (CGM) (Werk et al., 2013; Tumlinson et al., 2017). This still leaves a deficit of observed baryons relative to the predicted baryon density referred to as the missing baryons problem (Bregman, 2007; Shull et al., 2012).

At the turn of the century, cosmological hydrodynamical simulations of the large-scale structure have predicted the phase and location of these missing baryons (Springel et al., 2005; Dolag et al., 2017; Nelson et al., 2018; Pillepich et al., 2018). Baryons in intergalactic medium (IGM), although dominant at early epochs, remain challenging to observe. At high-redshift, the simulations indicate that the majority of the baryons are in the low-density ionised gas of the IGM. This phase is observationally traced by the Ly-α forest which only provides direct constraints on the neutral fraction of a gas which is mostly ionised (Kim and Kim, 2013). At lower redshifts, simulations of the matter distribution indicate that the baryons are related to a shock-heated phase of the gas with temperature range of $10^5 < \mathrm{T} < 10^7$ K, known as the Warm-Hot Intergalactic Medium (WHIM) (Cen and Ostriker, 1999; Davé et al., 2001). According to these simulations, at z = 0, the WHIM is the dominant baryon contributor and is located mostly in filaments and knots along the cosmic web, in which groups and clusters reside (Martizzi et al., 2019). A different simulations approach, using *Enzo* grid-code, not only doubles previous estimates of WHIM

baryon content, but also challenges the postulate that a significant amount of WHIM has been shock-heated to 10^7 K. Shull et al. (2012) found only a small hot plume at T$> 10^7$ K in the temperature-density phase diagram of IGM distribution of this shock-heated gas, whereas the rest of WHIM temperature falls in the range $10^5 >$ T$> 10^6$. Observational baryon-censuses also find that the Ly-α forest contains $\sim 30\%$ of the baryons, with similar amounts in gas at T$= 10^{5-6}$ K probed by O VI and broad Ly-α absorbers (BLAs). The speculation is that the remainder ("the missing baryons") reside at higher temperatures (T $> 10^6$ K) which are not traced by O VI and BLAs. Clearly, more stringent observational constraints of the hot phase of the IGM are needed.

Due to its diffuse nature, direct detection of the WHIM in emission poses a great observational challenge (Bertone et al., 2008; Frank et al., 2010; Augustin et al., 2019; Wijers et al., 2020). Different methods have been proposed to detect the hot, highly-ionized WHIM gas: detection in galaxy groups with the Sunyaev-Zeldovich effect (Hill et al., 2016; de Graaff et al., 2019b; Lim et al., 2020; Tanimura et al., 2020) using autocorrelation function measurements (Galeazzi et al., 2010), with absorption lines in quasar sightline (Kovács et al., 2019) and using the Cosmic Microwave Background (CMB) as a backlight (Ho et al., 2009).

To remedy this limitation related to diffuse nature, absorption lines detected against bright background objects offer the most compelling way to study the tempearture, ionisation state and column density of the gas. In these absorbers, the minimum gas density detected is set by the brightness of the background source and thus the detection efficiency is independent of redshift and the foreground object's brightness.

Oxygen is one of the most useful tracers of the WHIM because of its high abundance and because O VI, O VII, and O VIII excitation states span nearly the entire $10^5 - -10^7$ K temperature range. The doublet of C IV and Ly-α contribute at the low end as well, while Ne VIII (at 770 and 780 Å) is associated with collisionally ionised gas at T $\approx 5\times10^5$ K (Narayanan et al., 2011). The O VI doublet is observable in the UV with lines at 1032Å and 1038Å, which also makes them easy to identify (Howk et al., 2009). Unfortunately, the interpretation of O VI is complex. One issue is that O VI absorption turns out to be relatively easy to produce either from photoionization or collisional ionization (CIE). In CIE, the maximum fraction of Oxygen which is in O VI is only $\sim 20\%$, so the ionization correction are likely considerable (Werk et al., 2014; Prochaska et al., 2017). Additionally, we need to specify a metallicity in order to convert from O VI into a baryon mass, which is usually unknown. The WHIM can be traced by Ly-α absorption as well. These Ly-α lines look different from the narrow lines typical of the photoionized gas, since they are also appreciably thermally broadened. These are the BLAs, and overlap with the O VI-traced WHIM (Pachat et al., 2016).

Hotter collisionally ionized gas emits soft X-rays, but the emissivity is proportional to the square of the gas density, which again limits the effectiveness of emission as a probe of low-density gas. X-ray analysis traces metal emission lines (for the WHIM, primarily O VII and O VIII, but also Iron lines). Owing to the lack of telescopes with adequate sensitivity in the X-ray wavelengths, the hot phase of the WHIM traced by O VII and O VIII is as yet not well studied (Li, 2020). These lines, which correspond to a series of soft X-ray

features around 0.6-0.8 keV, are commonly detected at redshift zero, corresponding to the hot halo around the Milky Way (Gupta et al., 2012) (but see also Wang and Yao (2012)). At moderate redshifts, they are also accessible with the grating spectrographs on *XMM-Newton* (Arcodia et al., 2018) and *Chandra* (sensitive down about to 0.35 and 0.2 keV respectively). Unfortunately, current X-ray gratings have poor spectral resolution (700-800km s^{-1}), and effective areas of tens of cm^2 (compared to 1000-3000 cm^2 for *HST-COS* in the UV), so they have limited sensitivity to the WHIM (DeRoo et al., 2020). The detection of two X-ray absorbers towards 1ES 1553+113 by Nicastro et al. (2018) (but see Johnson et al., 2019, for a cautionary note) is the latest indication that the missing baryons are indeed in a diffuse WHIM phase, although it remains unclear which fraction of the missing baryons are traced by X-ray absorbers. Overall, there are only a few X-ray observed WHIM absorbers (Bonamente et al., 2016; Mathur et al., 2017; Nicastro et al., 2018; Johnson et al., 2019; Nevalainen et al., 2019). The next generation X-ray observatories such as *Athena* (Nandra et al., 2013) and its high spectral resolution micro-calorimeter with about an order of magnitude higher effective area than *XMM-Newton* and *Chandra*, will make significant progress in the next decade (Barret et al., 2020). Until then, it is extremely important to study the warm-hot gas, using the existing UV and X-ray facilities.

Given the challenges of X-ray data, observations at longer wavelengths (UV and optical) benefit from higher instrumental throughpout and enhanced spectral resolution. By reverting to ground-based facilities, longer exposure times and larger number of targets than available from space-based facilities become possible. Nevertheless, the UV lines from space have so far mostly been used to detect absorbing gas with temperature range $10^5 < T < 10^6$K from either O VI (Tripp et al., 2000; Danforth and Shull, 2005; Tripp et al., 2008; Danforth and Shull, 2008; Werk et al., 2014; Savage et al., 2014; Danforth et al., 2016; Kacprzak et al., 2016) or BLAs (Lehner et al., 2007; Danforth et al., 2010). Recently, Zastrocky et al. (2018) have constrained the Milky Way's hot ($T = 2 \times 10^6$ K) coronal gas using the forbidden 5302 Å transition of Fe XIV. Only recently, some highly ionised iron UV lines detected in emission have been used as diagnostics of gas at temperatures of $T=10^7$ K. Out of several forbidden lines in the UV that could trace this gas temperature range, and from various species of highly ionised iron, the emission of [Fe XXI] is the brightest (Anderson and Sunyaev, 2016). In particular, Anderson and Sunyaev (2018) report the discovery of [Fe XXI] in emission in a filament projected 1.9 kpc from the nucleus of M87 which validates the expected strength of the line. Theoretically, the highly ionised iron UV lines can be observed in absorption as well. The forbidden line of [Fe XXI], in particular, has the largest effective cross-section for absorption and a rest wavelength λ1354 Å, conveniently close to Ly-α λ1215 Å. Therefore the line is a sensitive UV-wavelength tracer of WHIM gas.

In this chapter, we target the [Fe XXI] line in absorption as a tracer of high-redshift 10^7K WHIM gas. Large optical spectroscopic quasar surveys available nowadays offer a new opportunity to statistically probe these filaments by detecting the matter between the high-redshift background quasar and the observer. Here, we make use of a large sample of high-spectral resolution quasar spectra with known intervening neutral gas Damped

Ly-α Absorbers (DLAs). Recent studies (Péroux et al., 2019; Hamanowicz et al., 2020) provide evidence for the paradigm of the origin of DLAs, showing that these objects probe overdensities (e.g. groups) in the Universe. We use these systems as tracers of foreground oversdensities, and to increase the sensitivity of the experiment we stack multiple quasar spectra at the DLA's redshifts (Mas-Ribas et al., 2017) to look for indications of T=10^7K WHIM gas traced by the [Fe XXI] absorption line.

This chapter is organized as follows: Section 2.2 presents the observations used for this study. Section 2.3 details the stacking method, while Section 2.4 summarizes our findings and future prospects with upcoming facilities. We adopt an H_0 =70 km s^{-1} Mpc^{-1}, Ω_M =0.3, and Ω_Λ = 0.7 cosmology.

2.2 A large sample of high resolution quasar spectra

To enhance the sensitivity to absorption line detection, this study focuses on the quasar spectra with the highest spectral resolution available. This work is based on a quasar sample observed with the Ultraviolet and Visual Echelle Spectrograph (UVES) of the European Southern Observatory's (ESO's) 8-metre Very Large Telescope (VLT) (Dekker et al., 2000). The UVES instrument is a two-arm (red and blue) grating cross-dispersed echelle spectrograph. Some observations are made using only one arm, but most observations use both arms simultaneously. The light is then split in two by a dichroic mirror and centered around to a standard or user-defined central wavelength.

Our study makes use of the first release of the Spectral Quasar Absorption Database (SQUAD) with 467 fully reduced, continuum-fitted quasar spectra (Murphy et al., 2019). Figure 2.1 shows an example of a VLT/UVES quasar spectrum, with a zoom on the Lyman-α quasar emission line. In this sample, the spectra were cross-matched with observations from the ESO UVES archives to include all quasars from literature up to August 2017 (Flesch, 2015). The redshift was also cross-matched with three databases (SDSS, NED and SIMBAD). In cases where no match was found, a measure of the redshift was derived directly from the UVES spectrum. Figure 2.2 illustrates the quasar redshift distribution of the whole sample. The redshifts range from $z_{em} = 0 - 6$, with a broad wavelength coverage range (3,050Å-10,500Å) with gaps depending on the chosen spectral settings. The mean resolving power of the exposures is R = 49,000. The corresponding resolution element is 6.1 km s^{-1}. The quasar spectra have on average a total exposure time of 5.9 hours, resulting in high signal-to-noise ratios per resolution element (hereafter snr_{ind}, for individual quasar spectra), reaching up to snr_{ind} >70. In other words, the full quasar sample is made of over 1450hrs of VLT time observations. Figure 2.3 displays the distribution of the snr_{ind} of the UVES quasar spectra.

Murphy et al. (2019) also provide a catalogue of 155 identified Damped Lyman-α Absorbers (DLA), out of which 18 are reported for the first time. The newly identified DLAs were found by visually checking the UVES quasar spectra. These DLAs are a class of quasar absorber tracing high H I column density cold (T=10^4K) gas, with N(H I)$\geq 2\times10^{20}$ (Wolfe et al., 1986). These systems comprise the majority of the neutral gas reservoir in the

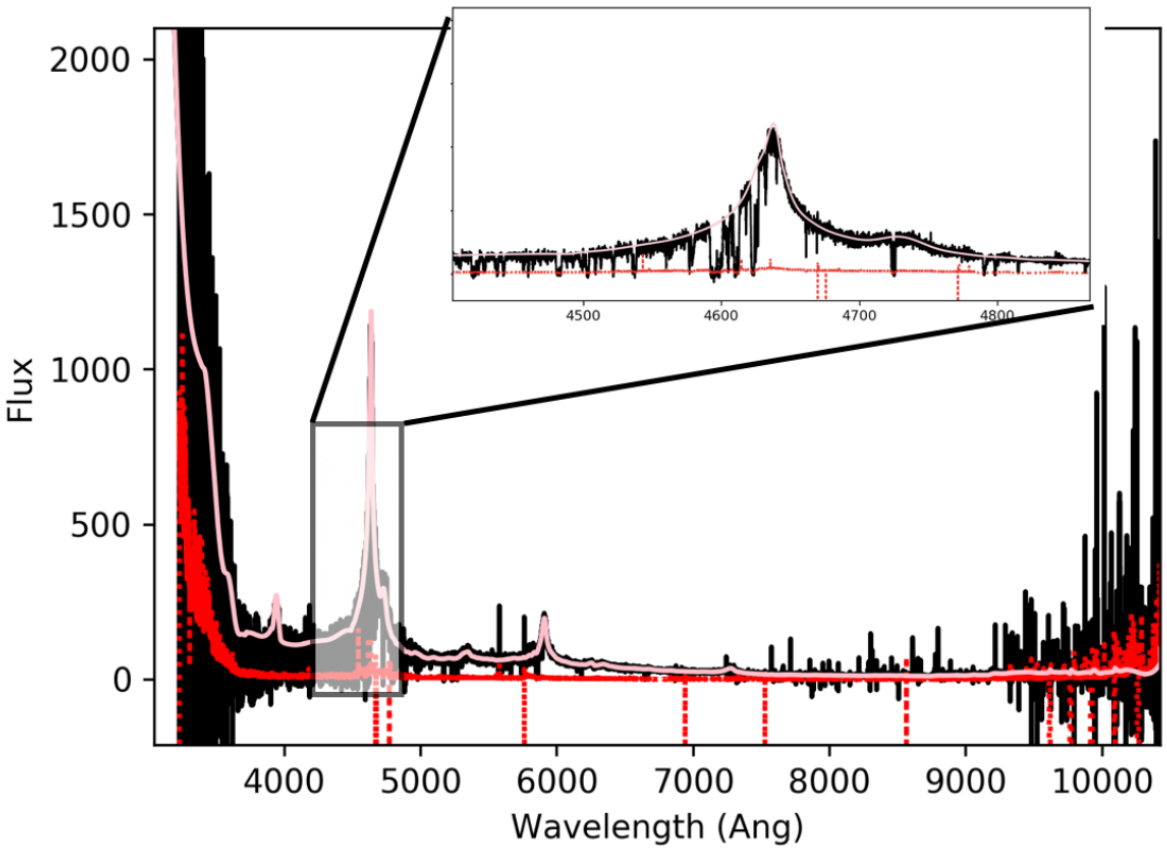

Figure 2.1: Example VLT/UVES quasar spectrum. The black histogram shows the full quasar spectrum at observed wavelengths and with arbitrary flux units. The quasar J000149-015939 at z_{em}=2.815 has a strong Lyα emission line at $\sim$ 4650 Å at restframe. The red histogram displays the corresponding error array. The pink line indicates the fitted quasar continuum. The inset zooms around the Lyman-α emission revealing the high snr_{ind}.

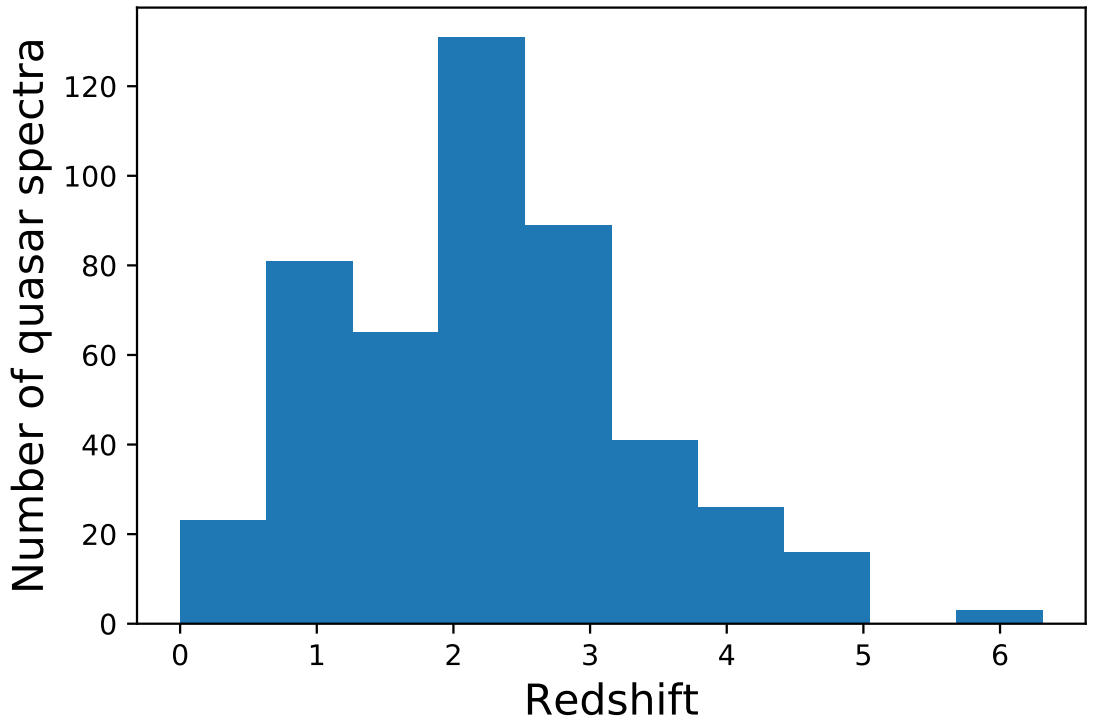

Figure 2.2: Quasar emission redshift distribution. The 467 UVES quasar spectra from the SQUAD sample cover a broad redshift range from $z_{em} = 0 - 6$, with wavelength coverage from 3,050Å to 10,500Å with gaps depending on the chosen spectral settings.

Universe used for the initial phase of star formation (e.g Peroux and Howk, 2020). Additionally, their metal content provides crucial information about the chemical evolution of galaxies. Figure 2.4 displays the redshift distribution of this sample of 155 DLAs. Orange (green/red) histograms indicate the redshift of $2^{nd}(3^{rd}/4^{th})$ DLA in those quasar spectra containing more than one. The mean DLA redshift for the sample is $z_{DLA} = 2.5$.

2.3 A stacked high-resolution DLA spectrum

At the high-resolution (R > 40,000) offered by UVES, the metallicity of individual DLAs is routinely well-measured (Kulkarni et al., 2005; De Cia et al., 2018; Poudel et al., 2020). In this work, we target weak metal lines which are not expected to be detected in a single spectra. In particular [Fe XXI] has an oscillator strength $f_{osc} = 5.3 \times 10^{-6}$ and a Doppler parameter $b_{Fe} = (2kT/m_{Fe})^{1/2} \approx (54.4 \text{ km s}^1)(T_7)^{1/2}$ where T_7 indicates at T = 10^7K. In order to probe these significantly weak absorption lines, we build a stack of more than a hundred high-resolution quasar spectra, shifted to the DLA redshifts.

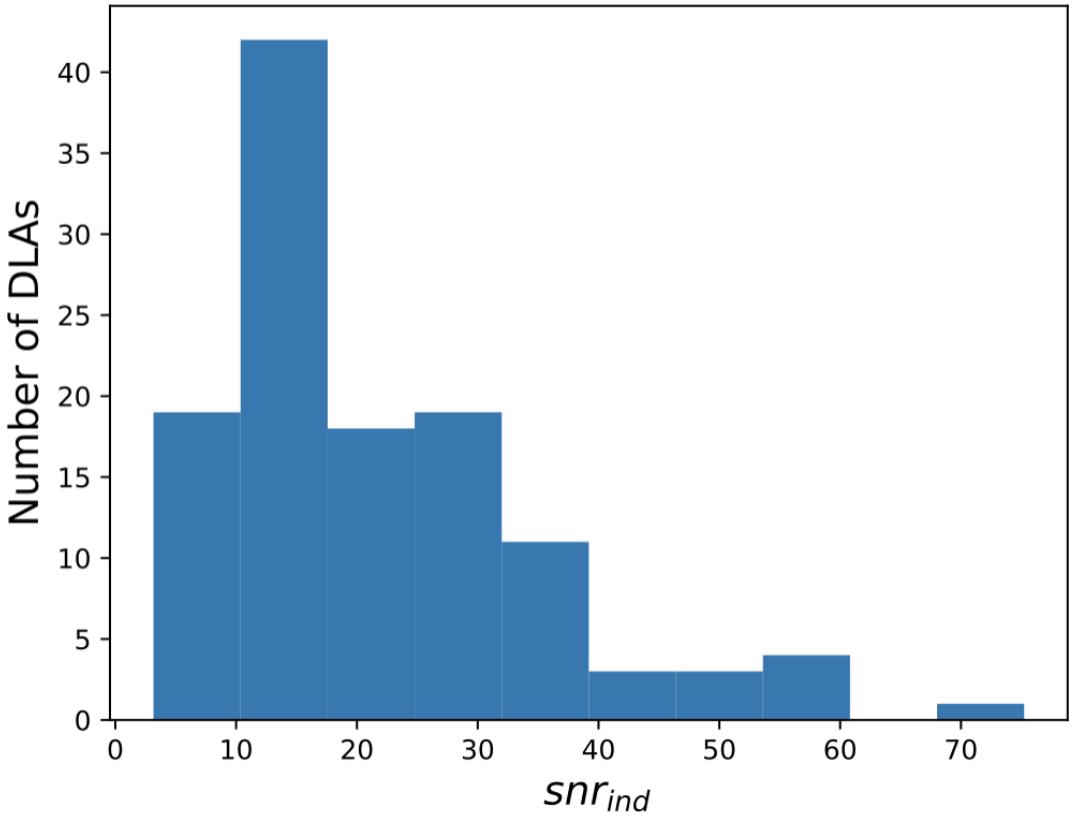

Figure 2.3: Signal-to-noise ratio per resolution element ($\mathrm{snr_{ind}}$) distribution. The histogram shows the 155 UVES quasar spectra containing at least one DLA. The mean resolving power of the UVES spectrograph (R > 40,000) combined with an averaged exposure time of 5.9 hours result in sizeable $\mathrm{snr_{ind}}$, reaching up to $\mathrm{snr_{ind}}$ >70.

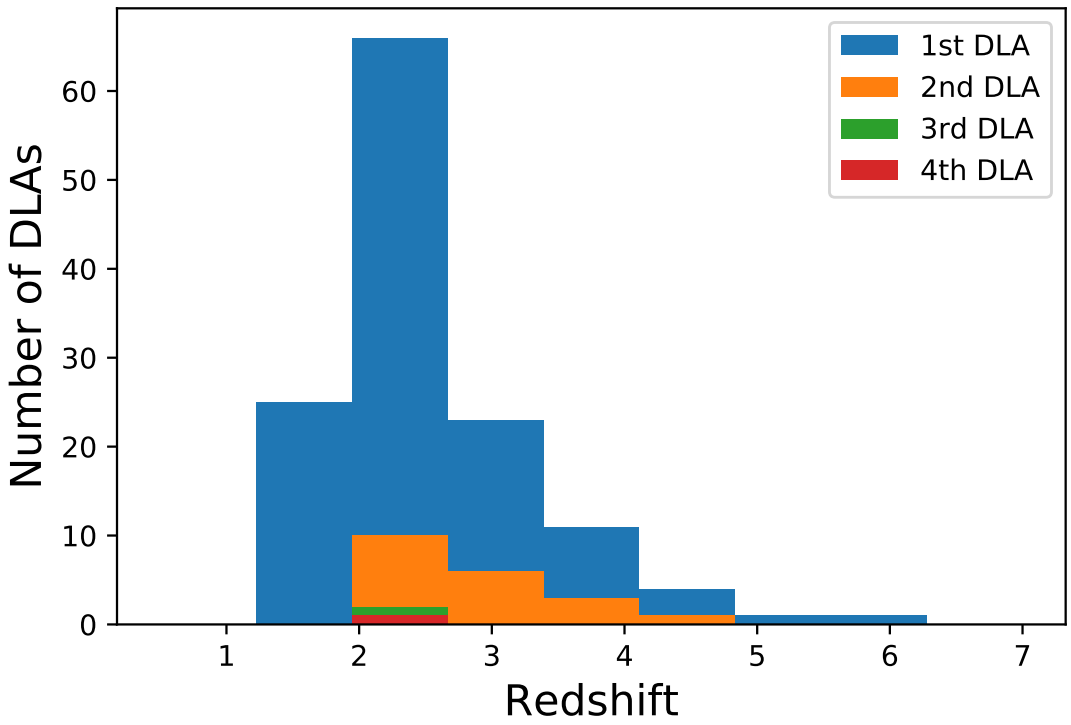

Figure 2.4: Redshift distribution of the 155 DLAs. Orange (green/red) histograms indicate the redshift of $2^{\mathrm{nd}}(3^{\mathrm{rd}}/4^{\mathrm{th}})$ DLA in one given quasar spectrum. The mean DLA redshift for the sample is $z_{DLA} = 2.5$.

2.3.1 Selecting quasar spectra

Targeting DLAs to search for metal lines limits the number of quasar spectra to be stacked to the ones containing known DLAs. This step results in a sample of 155 quasar spectra out of the 467 contained in the whole SQUAD quasar sample.

The dispersion of the UVES spectra, expressed in km/s per pixel also differs between five different values ranging from 1.3 km/s per pixel to 2.5 km/s per pixel. In order to avoid rebinning of the spectra during the stacking procedure, we elect to include only spectra with the same dispersion. A total of 137 spectra have a dispersion of 2.5 km/s per pixel which are then used in the subsequent study.

Finally, the spectral gaps in between the settings are evidenced by a visual inspection of the spectra. These gaps appear as flat lines in different parts of the spectra, where there is no signal. Only spectra with the appropriate wavelength coverage were included in further calculations depending on the location of the spectral gaps with respect to the targeted element at a given absorption redshift. This again caused a reduction of the number of spectra stacked depending on the element under study and its corresponding observed wavelength. For each metal line stacked, we compute the number of spectra covering the appropriate wavelength given the DLA's redshift and the quasar spectrum wavelength coverage (in the rest-frame ranging typically from $\lambda 1,200$ to $2,600\,\text{Å}$). The number of spectra included in the stack of each metal line are therefore different, and reported in each respective plot. For example, [Fe XXI] has a final number of stacked spectra of 106.

Note that some quasars contain multiple DLAs at different redshifts (with cases containing up to four DLAs in one quasar spectrum), so some quasar spectra are used multiple times (see Figure 2.4).

2.3.2 Stacking Procedure

We first shift the selected spectra to the DLAs rest-frame wavelength. We recall that all spectra have the same dispersion of 2.5 km/s per pixel, so that no rebinning is required in building the stack in velocity space. We then use the resulting quasar spectra sample to compute a median stack. We reject spectra which do not fully cover the wavelength range ± 500 km/s from the targeted metal feature. The corresponding number of quasar UVES spectra utilised are given in the legend of each of Figures 2.5, 2.6 and 2.7. At each pixel, we calculate the middle value of the ordered array of normalised fluxes from each quasar spectra. We also calculate mean and weighted-mean stacks. Our results indicate that the median stack recovers the normalised quasar continuum better, with a higher resulting SNR_{stack} (for signal-to-noise of stack spectra) and less prominent contamination from interlopers. The median stack therefore provides the most stringent limits and is used in the subsequent analysis.

2.3.3 Strong Metal Lines Detections

The neutral gas probed by DLAs contains a wide variety of metals with different ionization states. These trace gas temperature of the order 10^4K (Tumlinson et al., 2017). The metallicity of the DLAs evolves from $Z = 0.003Z_\odot$ solar at redshift $z = 4$, to $Z = 0.15Z_\odot$ solar at redshift $z = 1$ (Rafelski et al., 2012; De Cia et al., 2018; Poudel et al., 2020; Peroux and Howk, 2020), with no DLAs found with a metallicity below 0.0025 solar (Meiksin, 2009; Cooke and Fumagalli, 2018).

The median stack spectrum results in the detection of several strong metal absorption lines commonly reported in DLAs which demonstrates the sensitivity of our approach. Figure 2.5 shows an example of the median stack of 89 DLA spectra. The strong iron absorption line, Fe II ($\lambda_{\rm rest}$=1608), is undoubtedly detected. The following 15 lines were detected at the redshift of the DLAs with a wavelength interval between 1,200 Å and 2,600 Å: iron (Fe II 1608 Å, Fe II 2600 Å), silicon (Si II 1260 Å, Si IV 1393 Å, Si IV 1403 Å), carbon (C IV 1548 Å, C IV 1551 Å), sulphur (S II 1259 Å), zinc (Zn II 2026 Å), oxygen (O I 1302 Å), chromium (Cr II 2026 Å), manganese (Mn II 2577 Å), nickel (Ni II 1317 Å), aluminium (Al II 1671 Å, Al III 1863 Å). These detections are reported in the Appendix.

2.4 Probing the Warm-Hot Intergalactic Medium

2.4.1 Observed [Fe XXI] Column Density Limit

To search for tracers of the WHIM at UV-wavelengths, we also stack forbidden UV lines of highly ionized iron which trace T=10^7 K gas. The strongest of these lines is [Fe XXI] at rest wavelength λ1354.1 (Anderson and Sunyaev, 2016). This line is not detected in the stack spectrum as illustrated in Figure 2.6. Another 15 weak metal lines were searched for but not detected. These include absorption lines like chlorine, argon, titanium, chromium, cobalt, germanium, arsenic, and krypton (Prochaska et al., 2003; Ellison et al., 2010).

To compute the equivalent width (EW) upper limit for this non-detection, we use the following relation (Ménard and Péroux, 2003):

$$\mathrm{EW_{obs}} < \left[\frac{\sigma \times \mathrm{FWHM}}{\mathrm{SNR_{stack}}}\right] \approx (77\mathrm{mÅ})\left(\frac{\sigma}{5}\right)\left(\frac{\mathrm{FWHM}}{1.43}\right)^{-1}\left(\frac{\mathrm{SNR_{stack}}}{93}\right)^{-1} \tag{2.1}$$

where we assume a σ value equal to 5, and compute the signal-to-noise ratio (SNR_{stack}=93) of the stacked spectrum in the velocity range $-500 < v < 500$ km/s. The expected [Fe XXI] line is broad at the observed wavelength 4739 Å (1354.1Å at a mean redshift of $\langle z \rangle = 2.5$). At T = 10^7 K, the Doppler parameter b = 54.4 km/s and the FWHM = $2(\ln 2)^{1/2}$b = 90.6 km/s for a Gaussian line profile (Danforth et al., 2010; Keeney et al., 2012). We therefore assume a FWHM = 1.43 Å in equation 2.1. We compute the minimum observed equivalent width ($EW_{obs} < 77$mÅ) and convert it to rest-frame equivalent width $EW_{rest} < 22$mÅ. We compute the column density according to the linear relation between the equivalent width and the column density:

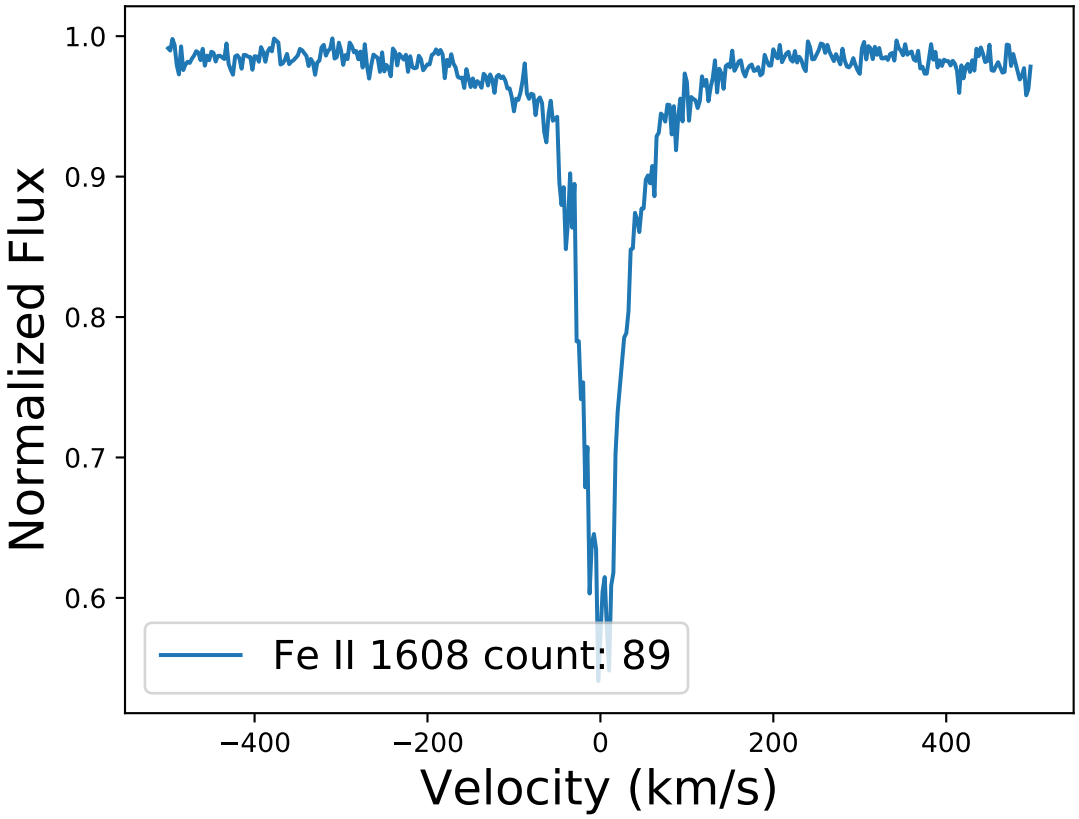

Figure 2.5: Example stack of a strong iron line. Stacking of 89 (as indicated in the legend) normalised UVES quasar spectra at the DLA position displays the detection of the Fe II $\lambda_{\text{rest}}1608$ line.

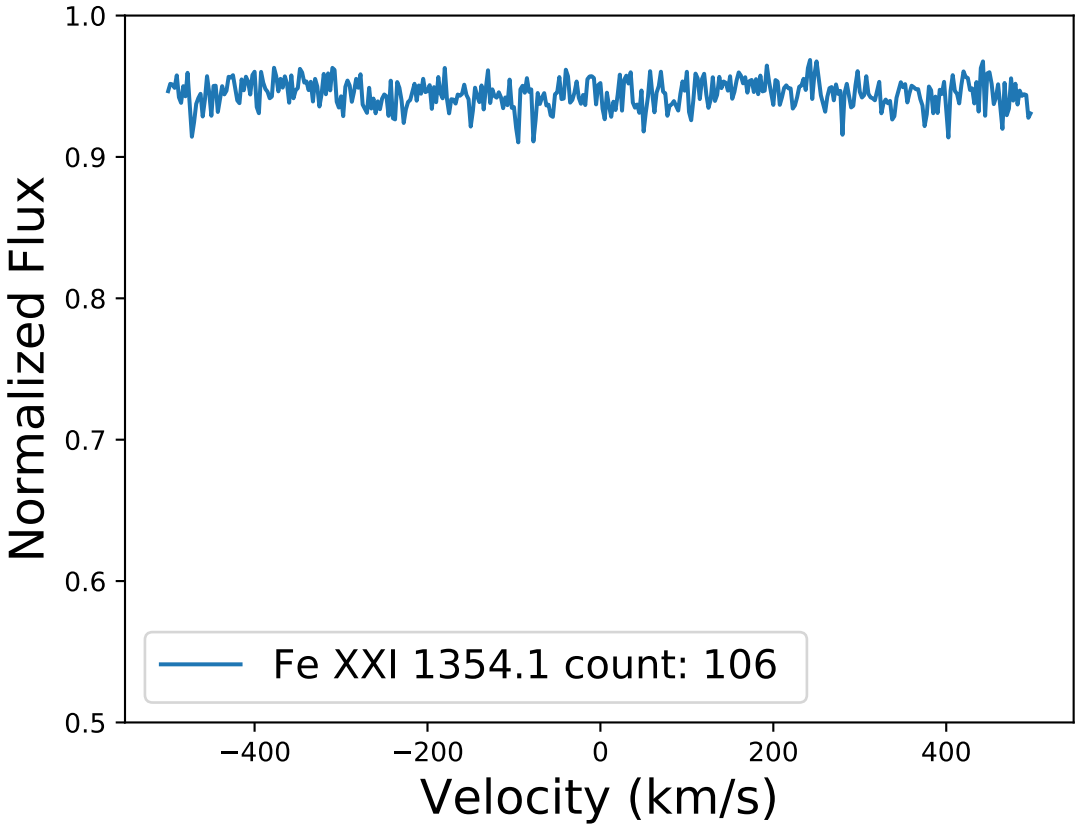

Figure 2.6: Stack of the weak [Fe XXI] line. Stacking of 106 (as indicated in the legend) normalised UVES quasar spectra at the DLA position leads to a non-detection of Fe XXI 1354Å. The y-axis values are set to match those of Figure 2.5.

$$\mathrm{EW_{rest}} = \left(\frac{\pi e^2}{m_e c}\right)\frac{N f_{osc}\lambda_{rest}^2}{c} \approx (0.860\mathrm{m\AA})\left[\frac{N([\mathrm{Fe\,XXI}])}{10^{16}\mathrm{cm}^{-2}}\right] \tag{2.2}$$

where c is the speed of light, m_e the electron mass, λ_{rest} is the rest wavelength of [Fe XXI], $\lambda_{\mathrm{rest}} = 1354\,\mathrm{\AA}$ and $\mathrm{f_{osc}} = 5.3 \times 10^{-6}$ is the oscillator strength for [Fe XXI].

Reverting the equation, we compute the corresponding column density log[N([Fe XXI])] using the value of $\mathrm{EW_{rest}}$ ($EW_{rest} < 22\mathrm{m\AA}$) as follows:

$$N([Fe\,XXI]) = (10^{16} cm^2)(EW_{rest}/0.860\,m\mathrm{\AA}) \tag{2.3}$$

The resulting column density limit in the stack of 106 DLAs observed in UVES quasar spectra at a mean redshift of $z_{DLA} = 2.5$ is log[N([Fe XXI])] < 17.4, where all column densities are expressed in units of cm^{-2}.

2.4.2 Expected [Fe XXI] Column Density

In order to put these results in context, we make two estimates of the expected column density of [Fe XXI] in gas typical of the WHIM, and its corresponding *EW*. In both cases, we assume that [Fe XXI] corresponds to 20% of the total iron abundance in the gas, i.e. an ionisation fraction of $(\mathrm{Fe}^{+20}/\mathrm{Fe})$=0.2. This assumption is justified from modelling of gas in collisional ionization equilibrium (CIE) using the CHIANTI database (Anderson and Sunyaev, 2016). We assume the metallicity of the gas to be $\mathrm{Z_{Fe}}$=0.1 $\mathrm{Z_\odot}$, i.e. $(\mathrm{Z_{Fe}}/\mathrm{Z_\odot}) = 10^{-1}$. Given a specific element, Fe, we refer to the usual relation (Peroux and Howk, 2020):

$$\mathrm{N_{FeXXI}} = \mathrm{N_{HI}}\left(\frac{\mathrm{Fe}}{\mathrm{H}}\right)_\odot\left(\frac{\mathrm{Fe}^{+20}}{\mathrm{Fe}}\right)\left(\frac{\mathrm{Z_{Fe}}}{\mathrm{Z_\odot}}\right) = 3.55 \times 10^{14}\mathrm{cm}^{-2} \tag{2.4}$$

where N(Fe) indicates the column density of iron (in atoms cm^{-2}), $(\mathrm{Z_{Fe}}/\mathrm{Z_\odot})$ is the logarithmic abundance relative to the assumed solar abundance, and $\mathrm{N(Fe)/N(H)_\odot}$ is the reference solar abundance of both the element and hydrogen in the Solar System. Here, we adopt values of the Solar System abundances of (Asplund et al., 2009) resulting in a column density of iron $\mathrm{log[N(Fe)]_\odot} = 7.5$ and column density of hydrogen $\mathrm{log[N(H)]_\odot} = 12$, meaning that $\mathrm{log(Fe/H)_\odot}$=−4.50.

Using the mean hydrogen column density of the DLAs in the sample: log[N(H I)] = 20.75, we calculate by assuming $(\mathrm{Z_{Fe}}/\mathrm{Z_\odot}) = 10^{-1}$ that the WHIM gas will have an expected column density of log[N([Fe XXI])] ∼ 14.5. In a second hypothesis, we assume that the metallicity of the WHIM gas is $(\mathrm{Z_{Fe}}/\mathrm{Z_\odot}) = 10^{-2}$, which then leads to an expected column density of log[N([Fe XXI])] ∼ 13.5. These column densities are about three orders of magnitude smaller than the upper limit derived from the stack of 106 UVES quasar spectra: log[N([Fe XXI])] < 17.4.

We note that in collisional ionisation equilibrium (Shull and van Steenberg, 1982), the ion fraction $f_{[Fe\,XXI]} = (Fe^{+20}/Fe) \sim 0.246$ peaks at logT = 7.0, but falls off rapidly at lower temperatures: $f_{[Fe\,XXI]} = 0.148$ ($\log T = 6.90$) and $f_{[Fe\,XXI]} = 0.026$ (logT = 6.80). Similar fall-off occurs at higher temperatures. Thus, the observed limits on $N([Fe\,XXI])$

are for a narrow temperature range, logT= 7.0 ± 0.1. The failure to detect [Fe XXI] could mean that the WHIM associated with the DLAs is cooler than T=$10^{6.8}$K. We note however that several recent studies have shown that DLA systems are primarily found in foreground overdensities (e.g. groups), which likely contain logT = 7.0 gas (Péroux et al., 2019; Hamanowicz et al., 2020). Alternatively, to be able to detect such [Fe XXI] column density, one would need to significantly increase the number of spectra in order to get a higher SNR_{stack}.

2.4.3 Future Prospects of Probing the WHIM at UV wavelengths

We now assess if this experiment with upcoming or planned facilities would reach the necessary sensitivity to detect the [Fe XXI] column density expected from the WHIM. First, we use equation 2.2 to compute the rest equivalent width corresponding to $\log[\mathrm{N}([\mathrm{Fe\,XXI}])] \sim 14.5$. We derive $\mathrm{EW_{rest}} = 0.03$mÅ. Assuming a mean DLA redshift for the sample $\mathrm{z_{DLA}} = 2.5$, we compute a corresponding observed equivalent width of typically $\mathrm{EW_{obs}} = 0.1$mÅ.

We look in turn into three future facilities with high-resolution spectroscopic capabilities. First, we focus on the Multi-Object Spectrograph Telescope (4MOST), a high-multiplex spectroscopic survey instrument currently under construction phase for the 4m VISTA telescope of the European Southern Observatory (ESO). 4MOST is expected to start its science operations in 2024. It has a wide field of view of 2.5 degrees diameter and nearly 2,400 fibers dividing in two different types of spectrographs. We here focus on the high-resolution fibers, offering nearly 800 spectra with a spectral resolution R$\sim$20,000 (FWHM=0.2Å at 6000Å) over a wavelength coverage λ3920Å to 6750Å (Quirrenbach and 4MOST Consortium, 2015). For a typical exposure time of 2hrs, 4MOST will deliver quasar spectra with an average individual spectra with signao-to-noise ratio $\mathrm{snr_{ind}}$=10 for a mag <19 object (de Jong et al., 2019). We note that the WEAVE instrument designed for the William Herschel Telescope (WHT) will offer comparable characteristics in the northern hemisphere (Pieri et al., 2016).

Secondly, we consider the High Resolution spectrograph (HIRES) for the 39m Extremely Large Telescope (ELT) currently under construction. HIRES (Marconi et al., 2018), which has successfully completed its Phase A, has a wide spectral coverage ranging from 4000 Å to 25000 Å with a spectral resolution R=100,000 (FWHM=0.04Å at 6000Å). HIRES is not a survey instrument, as opposed to the other facilities described here, being both a single-target spectrograph and a facility open to the community for small and medium-size proposals. However, the ESO open-archives policy (Romaniello et al., 2018) means that a significant number of quasar spectra will become publicly available after a few years of operations. Depending on the science goals, we expect quasar spectra to be recorded with $\mathrm{snr_{ind}}$ varying from 10 to 1000. Here, we assume a medium $\mathrm{snr_{ind}}$ per spectrum of $\mathrm{snr_{ind}}$=50.

Finally, we look further out in the future for upcoming facilities for multi-object spectrographs on 10m class telescopes. The Maunakea Spectroscopy Explorer (MSE) is being proposed to replace the Canada-France-Hawaii Telescope (CFHT) (The MSE Science Team et al., 2019). With a 1.52 $\mathrm{deg^2}$ field of view, it will have the capability of simultaneously

Table 2.1: Number of spectra needed for each facility to reach the SNR_{stack} necessary to detect [Fe XXI] in the WHIM at $\sigma = 3$. The first two rows indicate the spectral resolution of the facilities expressed as R and in Å as $FWHM$ at 6000 Å. The third row provides the required SNR_{stack} of the stack spectra to reach the $EW_{obs} = 0.1$m Å required to detect [Fe XXI]. The fourth row states the mean $\mathrm{snr_{ind}}$ of individual spectra foreseen for these facilities given a typical exposure time. Finally, the last row provides the number of quasar spectra required to achieve the corresponding SNR_{stack} in the stack spectra. Note that while the unmatched high spectral resolution of ELT/HIRES leads to a smaller number of spectra, this facility does not provide the multiplexing capabilities of other telescopes (4MOST, MSE/SpecTel).

Facilities	**4MOST**	**ELT/HIRES**	**MSE/SpecTel**
Spectral Resolution, R	20,000	100,000	40,000
FWHM [Å]	0.2	0.04	0.1
Required SNR_{stack} to reach $\mathrm{Ew_{obs}} = 0.1$mÅ	42,900	42,900	42,900
Individual $\mathrm{snr_{ind}}$	10	50	20
Number of Spectra	>18M	>700k	>4M

observing more than 4,000 objects. At low spectral resolution ($R \sim 3,650$), a $\mathrm{snr_{ind}}$ of 2 for magnitude 24 sources will be achieved in one hour observation. At high spectral resolution ($R \sim 40,000$; $FWHM$=0.1 Å at 6000 Å), a $\mathrm{snr_{ind}}$=20 for magnitude 20 source will be obtained typically in a little over 1-hour exposure. A conceptual design study for an analogous facility in the southern hemisphere has also been put forward. The so-called Spectroscopic Survey Telescope, here after SpecTel (Ellis et al., 2017), will offer a field of view of 5 deg^2 and will be equipped with 15,000 fibers covering a wavelength range of $3,600 < \lambda < 13,300$ Å.

The characteristics of each of these facilities are summarised in the first three lines of Table 2.1. We next estimate the SNR_{stack} of the stack quasar spectrum required to reach the expected observed equivalent width of $\mathrm{EW_{obs}} = 0.1$mÅ to detect a log[N([Fe XXI])] ~ 14.5 absorption feature at $\sigma = 3$. To this end, we revert equation 2.1 and derive SNR_{stack}=42,900. We note that given the width of the [Fe XXI] line (FWHM=1.43 Å), this calculation is independent of the spectral resolution of the instrument. We then compute the number of spectra, **N**, needed for each facility to reach the necessary SNR_{stack} in the stacked spectrum that will allow one to detect [Fe XXI] in the WHIM gas:

$$N > \left[\frac{SNR_{stack}}{\mathrm{snr_{ind}}}\right]^2 \tag{2.5}$$

We find that 4MOST, ELT/HIRES and MSE/SpecTel will require respectively >18M,

>700k and >4M quasar spectra to achieve the required sensitivity. The high-multiplexing capabilities of 4MOST, MSE and SpecTel mean that large samples can be acquired in a few years, although these large number of spectra are unrealistic at present. 4MOST quasar survey has scheduled 1M quasar spectra for understanding the baryon cycle with high resolution spectroscopy. Considering this, the number spectra we would require is more than one order of magnitude higher than the quasar survey that has been approved. The ELT is also highly unlikely to be able to collect 700k of individual quasar spectra in the next few years. Out of the three instruments, the only realistic option that would produce the number of spectra to achieve our objective would be MSE/SpecTel. The proposed alternative for finding this gas here would benefit from accumulating data from existing and upcoming quasar surveys (Liske et al., 2008; Merloni et al., 2019).

To put these results in context, we stress that this study is complementary to approaches planned at X-ray wavelengths with up-coming facilities. In coming decades, next-generation spacecraft aim to solve fully the missing baryons problem. The ESA *Athena* mission (Nandra et al., 2013) with spectroscopic and imaging capabilities in the 0.1–12keV range will significantly further our understanding of the baryons in the Universe, both inside the potential wells of groups and clusters of galaxies and in the WHIM in filaments between the densest regions in the Cosmos (Barret et al., 2020). Investigating how such potential wells formed and evolved, and how and when the material trapped in them was energised and chemically enriched, can uniquely be tackled by observations in the X-ray band, combining wide-field images with high resolution spectroscopy, both of high sensitivity. Similarly, *Lynx*, a mission proposed to NASA in the framework of the next flagship space telescope, will have total effective area greater than 2 m^2 at 1 keV (Falcone et al., 2018). One more option to consider for the detection of this T *sim* 10^7K gas is using soft X-ray grating spectrometer ARCUS (Heilmann et al., 2022). With improved resolving power compared to previous x-ray spectrometeres, ranging $6900 > R > 13000$, and an effective area of 150 and 800 cm^2 (Heilmann et al., 2022), this instrument would facilitate a survey of baryons at T 10^7K through absorption systems that have been so far only marginally detected with borderline statistical significance (Nicastro et al., 2018; Kovács et al., 2019). These facilities will provide a new window in our capability to characterise the physical processes of the WHIM. However, these exposures will reveal single WHIM detections, while the detection of [Fe XXI] in stack quasar spectra will offer a complementary way to characterise the physical properties of the WHIM in a statistical manner. By reverting to a statistical approach, this technique is less prone to uncertainties related to variation from object to object in the Universe (the so-called cosmic variance).

2.5 Conclusion

In this work, we target the [Fe XXI] line in absorption as a tracer of high-redshift 10^7K WHIM gas. We make use of a large sample of high-spectral resolution quasar spectra with known intervening neutral gas Damped Ly-α Absorbers (DLAs). To enhance the sensitivity to absorption line detection, this study focuses on high spectral resolution (R$\sim$49,000)

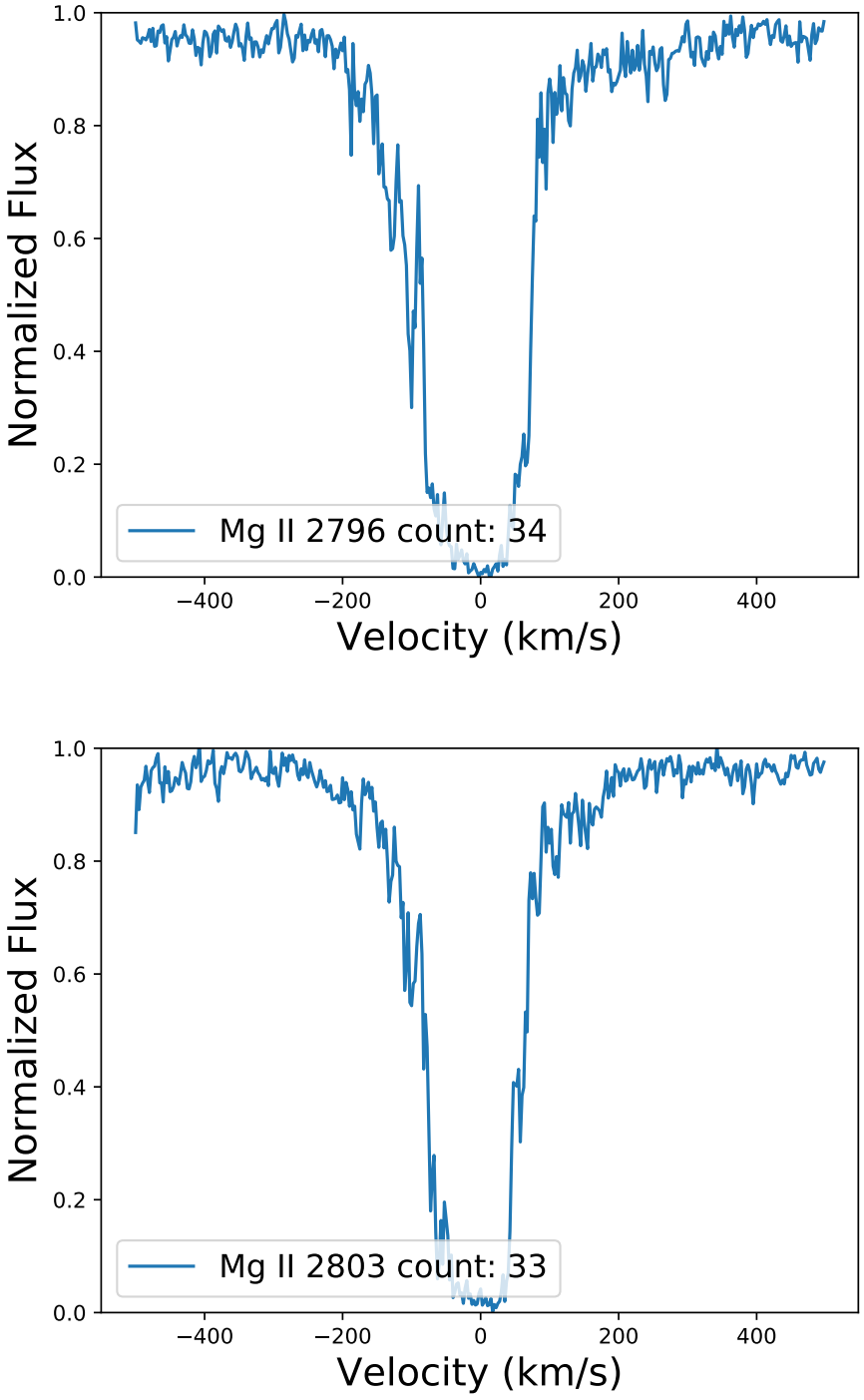

Figure 2.7: Stack of strong metal lines at the DLA redshift. The number of stacked normalised UVES quasar spectra are indicated in the legend for each element as well as the rest wavelength of the metal line. The mean redshift of the DLAs sample is $z_{DLA} = 2.5$.

quasar spectra from VLT/UVES. To increase the sensitivity of the experiment, we stack 106 quasar spectra at the DLA's redshifts to look for indications of 10^7K WHIM gas traced by the [Fe XXI] absorption line. We report a limit on the column density in the stack of

We then analyse the capabilities of future facilities, namely 4MOST, ELT/HIRES and MSE/SpecTel to detect such gas. We compute the number of spectra that would be needed from each of these facilities to reach the signal to noise ratio required for the detection of [Fe XXI] absorption line in 10^7K WHIM gas. We find that 18M high-resolution fibre 4MOST, 700k ELT/HIRES or 4M MSE/TechSpec quasar spectra are required. 4MOST quasar survey has scheduled 1M quasar spectra for understanding the baryon cycle (PI C. Peroux) with high resolution spectroscopy. The ELT is also highly unlikely to be able to collect 700k of individual quasar spectra in the next few years. Considering this, the number spectra we would require is more than one order of magnitude higher than the quasar survey that has been approved. Out of the three instruments, the only realistic option that would produce the number of spectra to achieve our objective would be MSE/SpecTel.

We have explored here an alternative method that this experiment could be initiated by cumulating samples from existing and planned quasar surveys with these facilities. In conclusion, we study here an alternative to X-ray detected WHIM tracers. While a significantly weak line, redshifted [Fe XXI] 1354 Å is observable at optical wavelengths from the ground, benefiting from higher instrumental throughput, enhanced spectral resolution, longer exposure times and increased number of targets.

Data availability

The data underlying this chapter are available at [doi:10.1093/mnras/sty2834]. The datasets were derived from sources in the public domain[1].

[1] `https://github.com/MTMurphy77/UVES_SQUAD_DR1`

Chapter 3

Searching for cold gas traced by MgII quasar absorbers in massive X-ray selected galaxy clusters

The contents of this chapter have been submitted to A&A (Fresco et al 2023 submitted)

Abstract Almost 50% of galaxies in the local Universe are in clusters or groups co-existing with both hot and cold components. Here, we observationally probe the cold gas content of X-ray selected massive galaxy clusters ranging from $M_{500} = 1 \times 10^{14}$ to 8.4×10^{15} with spectroscopic redshift from $0.3<z<0.67$ measured by the SDSS/SPIDERS survey. To probe the diffuse 10^4K gas in their intracluster medium, we utilise a large number of background quasar optical spectra from SDSS DR16. We first analyse a sample of spectra with known MgII absorbers, then blindly stack $\sim 16,000$ archival spectra at the redshifts of the foreground galaxy clusters. We tentatively (3.7σ significance) detect MgII in the clusters with an equivalent width EW(MgII λ2796) of 0.056±0.015 Å, corresponding to a column density log [N(MgII)/cm^{-2}]=12.12±0.1. We test our methodology by generating 22,000 mock SDSS spectra with MgII absorbers from Illustris-TNG50 cosmological magnetohydrodynamical simulation, combining photo-ionisation modelling and ray tracing. We also perform bootstrapping stacking at different cluster redshifts, and stack quasar spectra with no intervening clusters in the line of sight to measure the significance of our detection. These results are in line with recent similar observational studies but challenge predictions from Illustris-TNG simulations. Together, our findings indicate that large amounts of cold gas may be found in the most massive structures of the Universe.

3.1 Introduction

Galaxy clusters are an important laboratory for testing models of gravitational structure formation, for constraining the parameters of cosmological models, measuring the mean matter density of the universe, and to investigate galaxy evolution as well as plasma physics (Kravtsov and Borgani, 2012). Despite the advances of decades of observations and simulations, the interactions between the gas phases that make up the baryon content of clusters remain largely unknown.

The baryon budget in clusters within R_{500}[1], although not well constrained, is made up of approximately 70% of hot Intracluster Medium (ICM), 13% of cold gas from stars and galaxies, and 17% of warm hidden baryons still to be observed (Ettori, 2003; Fukugita and Peebles, 2004; Gonzalez et al., 2007a,b; Kravtsov et al., 2005). The ICM in galaxy clusters has been thoroughly studied in X-rays, with instruments like ROSAT, XMM-Newton, Chandra (see e.g. Sarazin, 1986; Rosati et al., 2002; Böhringer and Werner, 2010, and references therein), and now eROSITA (Merloni, 2012; Predehl et al., 2021). In the meantime, optical and near infrared observations from the Dark Energy Survey and the Hyper Supreme-Cam survey provide a different perspective on the growth and evolution of baryons in clusters (Aihara et al., 2018; DESI Collaboration et al., 2016).

Alongside to these developments, structure formation studies have progressively focused on the cycle of baryons. The physical processes by which gas is accreted into galaxies, transformed into stars and then expelled from galaxies into their circumgalactic medium (CGM) are of paramount importance for galaxy formation and evolution (Tumlinson et al., 2017). The vast majority of the CGM studies so-far have focused on field galaxies, while almost $\sim$50% of galaxies in the local Universe are in clusters or groups (Eke et al., 2004). In addition, simulations predict a major fraction of the baryons at lower redshift are found in gas 10^5-10^6K, the so-called warm-hot intergalactic medium or WHIM (Cen and Ostriker, 1999; Davé et al., 2001). Focusing on the Virgo cluster as a close-by laboratory, early results from Yoon and Putman (2013) have shown that the CGM surveys must consider the role of the environment. Clusters provide rather complex astrophysical and dynamical systems, where many different physical processes take place, such as galactic winds, active galactic nuclei (AGN) feedback, and gas stripping leading to mixing and redistribution of metals in the ICM (Simionescu et al., 2009; Kirkpatrick and McNamara, 2015). Yet, as mentioned above, the baryon budget in clusters is not well constrained mainly because it is unclear whether all baryonic constituents have been identified and quantified.

The ICM is an essential component for the assessment of the cosmic baryon and metal budgets, given that the ICM contributes even more to the overall baryon budget than stars (e.g. Gonzalez et al., 2013; Péroux and Howk, 2020). Within these large structures, the ICM material is composed and mixed with the CGM material of many group members. Galaxies are infalling and orbiting within halos, while their properties are likely affected by encounters with the warm and hot gas sitting in the gravitational well (e.g. Popesso

[1]We define R_{500} as the radius where the density is 500 times the critical density of the Universe at given redshift.

et al., 2015). The large amounts of hot gas trapped within their deep potential wells make clusters of galaxies shine in the X-ray waveband (e.g. Jones and Forman, 1999). However, determining the abundance of elements other than iron probed by X-ray observations is currently challenging and uncertain (Mernier et al., 2018; Frebel, 2018).

From a theoretical standpoint, modern cosmological hydrodynamic simulations show that cool-warm gas from the CGM of galaxies is stripped from the galactic potentials through ram-pressure forces of the hot ICM (Ayromlou et al., 2019; Yun et al., 2019). On the other hand, cosmic web filaments interact with galaxy clusters permeating gas streams of relatively metal-poor cool-warm gas. These and other mechanisms create an inhomogeneous and turbulent multi-phase ICM with a range of physical and chemical properties (Bahé et al., 2013; Simionescu et al., 2019; Kravtsov and Borgani, 2012; Kunz et al., 2022).

The hotter component ($T \sim 10^{6-7}$K) of this multi-phase gas emits at X-ray wavelenghts. Because the gas is diffuse, it is best probed using quasar absorption line spectroscopy which has proven to be a powerful probe of these environments. Absorption lines detected against bright background quasars offer the most compelling way to study the distribution, chemical properties and kinematics of CGM gas (Hamanowicz et al., 2020; Szakacs et al., 2021). In these quasar absorbers, the minimum gas density that can be detected is set by the brightness of the background source and thus the detection efficiency is independent of redshift (Tripp et al., 1998). While individual absorption measurements are limited to a pencil-beam along the line-of-sight, a sample of sightlines allows us to statistically measure the mean properties of galaxy clusters. These techniques have been extensively used to investigate the gaseous halos of isolated galaxies (Szakacs et al., 2021). Without a quantitative description of the most massive structures in the low-redshift Universe, however, one cannot reach a full census of baryons and metals in the Universe.

Among quasar absorbers, the low-ionisation MgII doublet is known to trace cold 10^4K gas. Because of its distinct doublet feature, MgII has been used extensively in a large number of spectroscopic surveys. In the last two decades, MgII absorption systems surveys have been used to study the physical properties of large samples of galaxies over a wide range of luminosities and morphologies (Lanzetta and Bowen, 1990; Nestor et al., 2005; Narayanan, 2007; Lopez et al., 2008; Seyffert et al., 2013; Anand et al., 2021). Absorption by MgII in cosmological galaxy formation simulations has been analysed (Nelson et al., 2020; Augustin et al., 2021), and is shown to closely relate to star forming regions, galactic outflow and galactic disks (Bowen and Chelouche, 2011). They are known to be associated with galaxies and their CGM (Bouché et al., 2006; Zhu et al., 2015), and individual absorption lines allow us to characterise the spatial distribution and physical properties of the cold gas clouds located in the vicinity of galaxies (Lan and Mo, 2018; Zhu et al., 2015).

Recently, large spectroscopic surveys have focused on the incidence of MgII in and around galaxy clusters, with different methods and samples, showing a wide range of detections (Anand et al., 2022; Mishra and Muzahid, 2022). Here, we build on these works to study the cold gas traced by MgII absorbers in a large sample of massive X-ray selected clusters.

The chapter is organised as follows: Section 3.2 presents observational data used in this

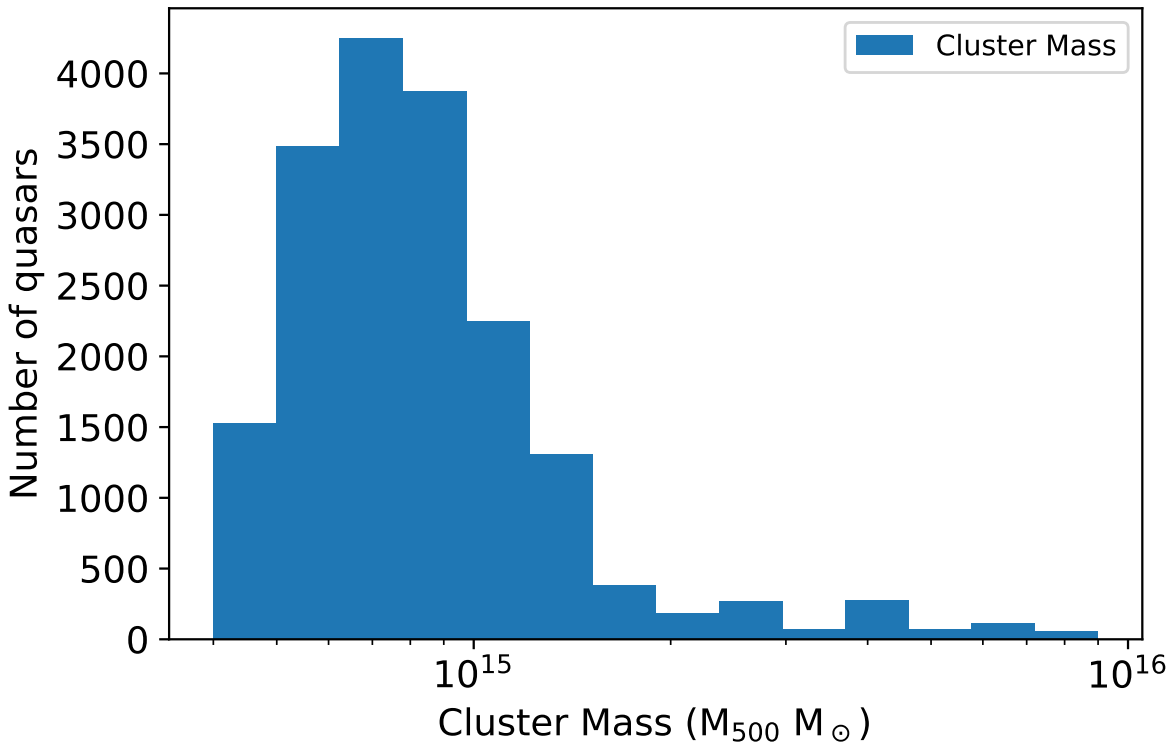

Figure 3.1: Distribution of number of background quasar spectra of the full sample used in the analysis as a function of the foreground cluster mass within R_{500}.

study. Section 3.3 details the analysis performed, while Section 3.4 focuses on the results. In section 3.5, we discuss our findings in the context of other works and state-of-the-art simulations. We summarise and conclude in Section 3.6. Here, we adopt an $H_0 = 67.74$ km s^{-1} Mpc^{-1}, $\Omega_M = 0.3089$, and $\Omega_\Lambda = 0.6911$ cosmology.

3.2 Observational Data

3.2.1 The foreground cluster sample

We start our analysis from the largest spectroscopically confirmed sample of massive clusters compiled from the Sloan Digitan Sky Survey (SDSS) from the SPectroscopic IDentification of EROSITA Sources (SPIDERS) program (Clerc et al., 2016, 2020; Kirkpatrick et al., 2021a; Ider Chitham et al., 2020). Cluster candidates for SPIDERS have been drawn from a subset of CODEX (Finoguenov et al., 2020), an X-ray selected catalogue of clusters from the ROSAT All Sky survey (RASS), specifically in the 5,350 square degree BOSS imaging footprint; 2,740 CODEX clusters are included in the SPIDERS sample. These are complemented by the X-CLASS cluster sample (based on serendipitous XMM-Newton ob-

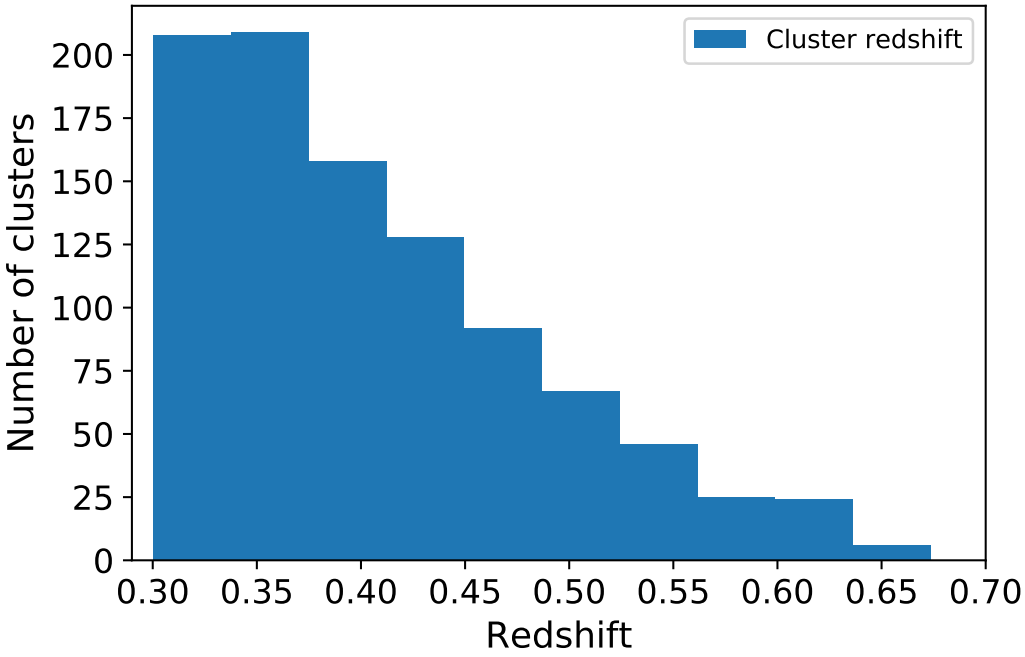

Figure 3.2: Distribution of cluster redshifts from the parent SPIDERS sample (Clerc et al., 2020) used in this study. The clusters constitute a sub-sample of the parent sample for which MgII absorption lines would fall within the observed SDSS spectral range.

servations) with 124 uniquely identified and confirmed clusters (Clerc et al., 2014). Visual inspections of individual spectra are carried out by trained astronomers to verify the existence of a cluster. After a first run with the redMaPPer (Rykoff et al., 2016) algorithm for automatic membership assignment, a minimum of three visual inspecting members are required to converge on a final redshift determination, the final condition being that these members lie close to each other in a velocity-distance diagram. Due to the uncertainty associated with the position of the detections, several measures are taken to ensure the closest possible estimation of redshift. The chances for a candidate to be validated are highly dependent on redshift, cluster richness, and number of spectra available. For example, in the spectroscopic redshift determination there are 622 instances where the mean spread in the measurements is $\delta_z = 0.00049$ (147 km s^{-1}), while the maximum is $\delta_z = 0.0055$ (1 650 km s^{-1}). All objects with velocities offset greater than 5000 km s^{-1} are rejected as members of the cluster.

Figure 3.1 shows the distribution of foreground cluster masses. Scaling from their X-ray luminosities, the average mass of these systems amounts to $M_{500c} = 2.7{\times}10^{14}$ $M_\odot$ (converted from $M_{200c} = 3.9{\times}10^{14}$ $M_\odot$). Here, we mainly express the cluster mass in units of M_{200c}, i.e. the mass within a radius R_{200c}. This corresponds to the radius enclosing an average density 200 times above the critical density of the Universe at the cluster's redshift.

It is expressed as follows:

$$R_{200} = \left(\frac{3M_{200c}}{4\pi 200 \rho_{cr}} \left(\frac{H_z}{100} \right)^{-2} \right)^{1/3} \tag{3.1}$$

In order to compare these results to the latest related published research, we use the public open-source package COLOSSUS to convert between M_{200c} and M_{500c} (Diemer, 2018), and continue to do so throughout the chapter for consistency.

The observed galaxy cluster distribution sample covers a redshift span of $0.03 < z < 0.677$ (a subset of which - systems with z>0.3 - is shown Figure 3.2), with a typical statistical uncertainty on each redshift of $\Delta_z/(1+z) = 6 \times 10^{-4}$ (Kirkpatrick et al., 2021b). The number of spectroscopic members per system ranges between 3 to 75, with a mean of 12.

3.2.2 The background quasar sample

We select spectra of background quasars from SDSS. The spectra are observed with the 2.5m Sloan Telescope as part of the BOSS and eBOSS surveys (Smee et al., 2013), covering a wavelength range of 3600Å to 10,400 Å at a spectral resolution of $\lambda/\Delta\lambda \sim 2000$, or with the SDSS-I instrument, covering 3800 Å to 9100 Å, with the same spectral resolution. The Data Release 16 of SDSS comprises a complete selection of spectroscopically confirmed quasars (Lyke et al., 2020; Ahumada et al., 2020). It includes 750,414 confirmed quasars.

3.2.3 Pairing background quasars with foreground clusters

A key component of the analysis is to determine which quasar sightlines pass close to a foreground galaxy cluster in projection on the plane of the sky. We determine the number of quasar-cluster pairs by cross-matching the foreground cluster sample with the background quasar catalogue. We select all SDSS spectra from the parent sample with a distance in Right Ascension and Declination within 3 times R_{200} (apparent R_{200c}) of the centre of a cluster, and a redshift of $z_{quasar} > z_{cluster} + 0.01$ for a total of 434,736 spectra. We make use of the cluster optical center from the DR16 catalogue. We note that the cluster centre is not always well constrained because of the uncertainty in the redshift of some of the members. Among these cluster-quasar pairs, we select the ones for which the foreground cluster will have a redshift such that MgII is covered by the SDSS spectra (z>0.3), and a redshift of the quasar $z < 5$. This leads to a total of 18,694 quasar-cluster pairs. Figure 3.3 shows the distribution of redshift of the foreground clusters of these pairs in blue. Where the green represents the quasar redshift, the yellor represents the MgII known absorbers redshift.

The signal-to-noise ratio (SNR) is computed following Mas-Ribas et al. (2017) for each spectrum as SNR= median(flux)/spread, where the spread is the standard deviation defined as the dispersion of the flux relative to the mean, and the median is calculated over the flux of the spectra. The distribution of signal-to-noise ratio (SNR) of the spectra is presented in Figure 3.4.

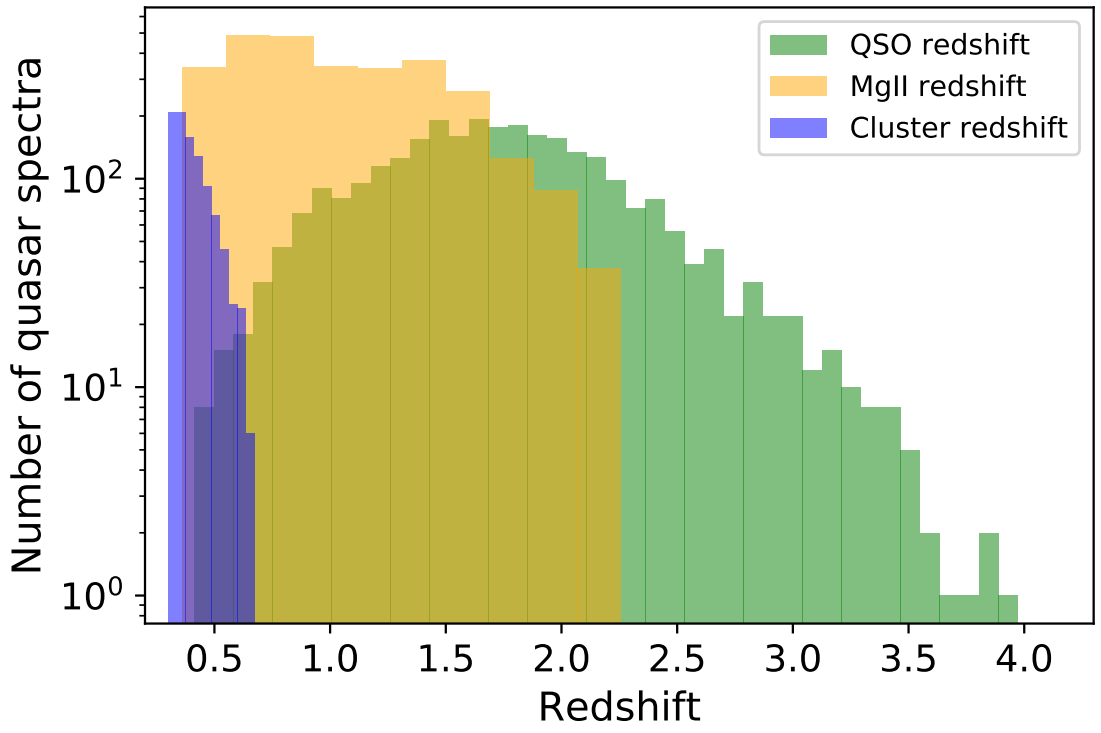

Figure 3.3: Histogram of the number of quasars as a function of their redshift (green), the redshift of their intervening MgII absorbers from Anand et al. (2021)(orange) and the redshift of the foreground clusters (blue).

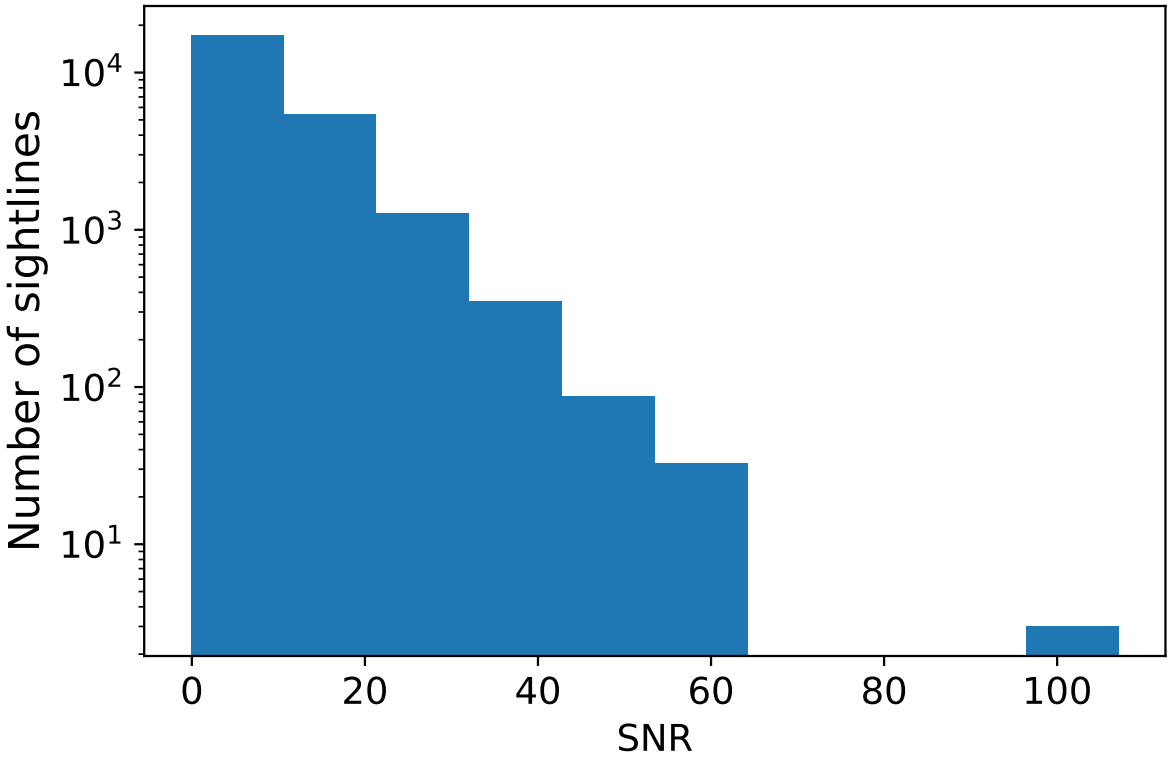

Figure 3.4: Distribution of the signal-to-noise ratio (SNR) of the spectrum of background quasars (see text) from the SDSS DR16 sample with foreground clusters. The mean signal-to-noise value of spectra is ∼2.31.

For each of the pairs, we calculate the angular separation between the foreground cluster and the background quasar projected on the sky plane. The angular separation is normalised by the R_{200} radius of the cluster. We stress that while we define units of R_{200}, all the figures presented in this work are in units of R_{500} in order to ease comparison with the literature.

3.2.4 Known MgII quasar absorbers sample

Our analysis also makes use of the MgII quasar absorption catalogue of Anand et al. (2021). The authors developed an automated pipeline to detect intervening metal absorption line systems with a matched kernel convolution technique and adaptive signal-to-noise criteria. By processing one million quasars from the SDSS DR16, they compile a sample of about ∼160,000 MgII absorbers in the redshift range $0.3 < z_{abs} < 2.3$. After cross-matching our sample of quasar-cluster pairs with this absorption catalogue, we get a match for 4,150 spectra. Figure 3.3 illustrates the redshift distribution of these MgII quasar absorbers matches in orange while the quasar spectra with foreground clusters are shown in blue, and the background quasars in green. We use the publicly available catalogue to estimate the velocity difference, Δv, between the absorption redshift ($z_{\rm abs}$) and the cluster redshift ($z_{\rm cluster}$). We express Δv as follows:

$$\Delta v = \frac{\Delta z \times c}{1 + z_{\rm cluster}} \tag{3.2}$$

where c is the speed of light in km/s and the $z_{\rm cluster}$ is the mean redshift of the clusters for a given sub-sample as tabulated in Table 3.1. These velocity differences can be very large, since the absorption redshifts are not necessarily close to the clusters. Fig. 3.5 displays the full range of Δv between [-5000:5000] km s^{-1}. Due to the high velocity dispersion expected in galaxy clusters (Girardi et al., 1993) we chose to focus on the range of [-2000:2000] km s^{-1} around the clusters. In total, we found 32 absorbers associated with the clusters in our sample, resulting in an overall incidence of $32/16224 \approx 0.2\%$.

3.3 Analysis

3.3.1 Normalising the background quasar spectra

In order to retrieve the quasar absorption systems, we remove the intrinsic spectral signature of the background quasars. To this end, we model each of the SDSS quasar spectra with the highly flexible Python QSO fitting code, PyQSOfit (Guo et al., 2018). This algorithm fits the spectral features, broad emission lines and continuum slope, of the quasars. Figure 3.6 displays an example spectrum showing both the quasar continuum fit and the ratio between the original data and the fitted continuum, resulting in a normalised spectrum. For some objects, the emission lines cannot be perfectly modelled and after normalisation, some residuals remain. We note in particular the noise of the SDSS spectra

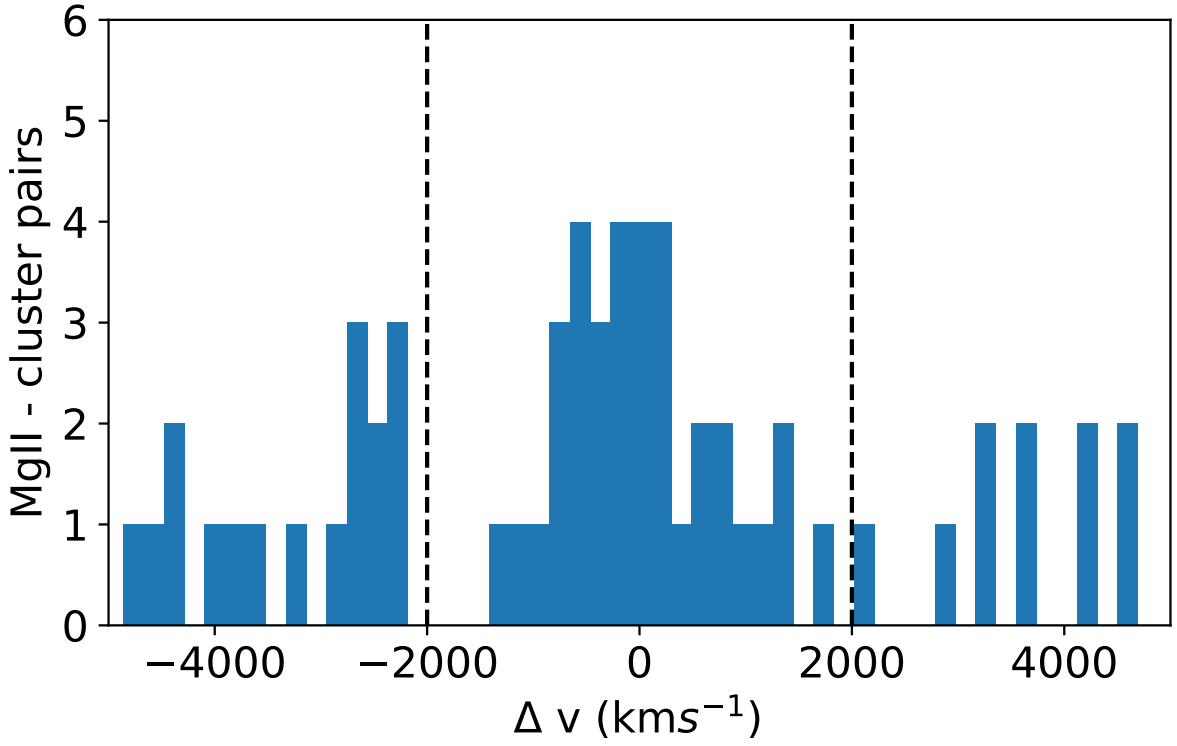

Figure 3.5: Velocity difference, Δ v, between the known MgII absorber from Anand et al. (2021) and the cluster redshift, as defined in equation 3.2. The figure displays the full range of Δ v between [-5000:5000] km s^{-1}. In the subsequent analysis, we chose to focus on the range of [-2000:2000] km s^{-1} around the cluster as indicated by the dashed lines.

increases at each end of the wavelength window, resulting in noisy edges in the normalised spectra. Nonetheless, the method proved very efficient to remove the features of quasar emission.

3.3.2 Stacking background quasar spectra at the position of foreground clusters

In order to detect the weakest tracers of the cold gas, we take advantage of the large amount of spectra available, by stacking the background quasar spectra at the redshift of the foreground clusters. We first shift the quasar spectra to the cluster rest-frame. We use the fact that all the SDSS spectra have a constant log step of 0.0001 (approximately 69 km s^{-1}) to avoid interpolating between pixels. We note here that for this specific cluster sample, Clerc et al. (2020); Kirkpatrick et al. (2021a) indicate that the typical statistical uncertainty on the cluster's redshifts is $\Delta z/(1+z) = 6 \times 10^{-4}$, which is about 180 km/s. This mean value does not reflect the distribution of the cluster's redshift uncertainties, which may depart from a Gaussian profile. Following the method of Fresco et al. (2020) described in Chapter 2, we perform a median stack in the velocity region that can be attributed to the foreground cluster within a window of [-2000:2000] km s^{-1}. After this process, a gaussian smoothing of 1 pixel was applied using GAUSSIAN SMOOTH from SPECUTILS.

In this analysis, we stack two independent sets of quasar spectra. First, we stack quasar spectra with known MgII absorbers which happen to be close in velocity space to a foreground cluster. Multiple stacks are performed as described in the previous section. We refer to this sample as the *MgII-selected sample*. This MgII-selected sample is used as a test for our methodology and to check that the stacked spectra recover the features even with the large velocity dispersions inherent to massive galaxy clusters, which will likely induce velocity offsets at the impact parameter where the quasar's line-of-sight pierces the cold gas traced by MgII. Table 3.1 summarises the (small) number of available spectra in the MgII-selected sample and the corresponding signal-to-noise of the resulting stacked spectrum.

Second, we "blindly" (i.e. without a priori knowledge of the presence of MgII absorbers) stack all the quasar spectra that have a foreground cluster, these corresponds to the so-called *blind sample* and is described in Table 3.1.

3.3.3 Measuring Equivalent Widths and Column Densities

We first search blindly for the minimum flux within the full velocity range [-2000:2000] km/s around the MgII 2796 Å line. The wavelength of the minimum flux is then set to the MgII 2796 Å line. We then use the precise 750 km s^{-1} velocity separation between the MgII lines of the doublet to materialise the position of MgII 2803 Å. To quantify the amount of cold gas, we measure the equivalent width of the MgII lines. By focusing on the MgII 2796 Å line, we offer a conservative measurement of the strength of the MgII doublet. The observed spectra can be seen in Figures 3.7 and 3.8 for the MgII-sample and blind

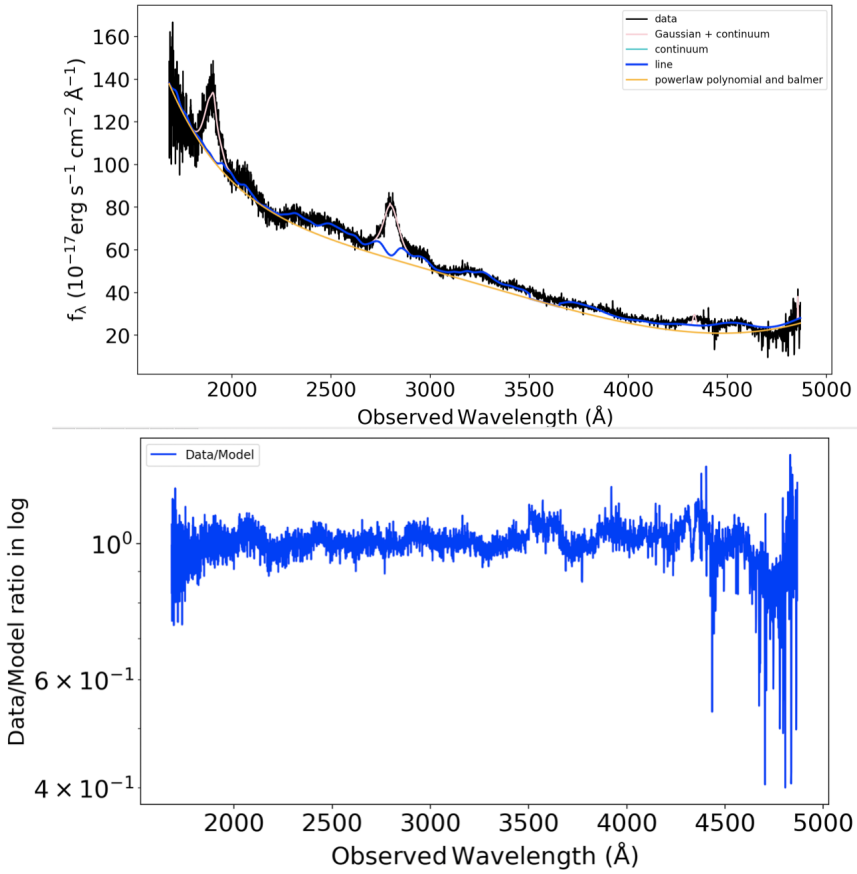

Figure 3.6: Example of observed-frame SDSS quasar spectra and data/model ratio spectra after removing the features of quasar emission and converting to unit average flux density with the package PyQSOFit (Guo et al., 2018). On top, we show the original SDSS spectrum and in colours the multi-component fit performed with PyQSOFit. The bottom panel displays the resulting quasar spectrum normalised to an arbitrary value of 1 by dividing the observed spectrum with the continuum.

sample, respectively. The EW is measured by integrating the area of the spectrum over the wavelength range defined by vertical lines around our first line of the doublet, which we fixed at the MgII 2796 Å line -500km/s blueward and +375km/s redward. Then we measure second line of the MgII doublet, the MgII 2803 Å line, which is located at +750km/s redward. The same method is applied to the MgII 2803 Å line which is integrated from -375km/s (blueward) to +500km/s (redward) of the rest-frame wavelength. These measures result in estimates of the strength of the detected MgII absorbers. We make use of the LINETOOLS software package (Prochaska et al., 2017) to calculate the EW. The estimates of the uncertainties are based on simulations of mock spectra as described in section 3.4.4.

For the conversion of observed-frame EW to rest-frame equivalent width, we follow the usual relation:

$$\mathrm{EW_{rest}} = \frac{\mathrm{EW_{obs}}}{(1 + \mathrm{z_{cluster}})} \tag{3.3}$$

where the redshift $\mathrm{z_{cluster}}$ is the averaged cluster redshift of each of the stacked subsamples as listed in Table 3.1.

The MgII column density is then computed according to the linear relation between the equivalent width and the column density using the following equation from Zhu et al. (2014):

$$\mathrm{N[MgII]} = 1.13 \times 10^{20} \left(\frac{\mathrm{EW_{rest}}}{\mathrm{f_{osc}} \lambda^2_{\mathrm{rest}}} \right) \mathrm{cm^{-2}} \tag{3.4}$$

where λ_{rest} is the rest wavelength of each of the MgII lines of the doublet, $\lambda_{\mathrm{rest}} = 2796\,\text{Å}$ and $\lambda_{\mathrm{rest}} = 2803\,\text{Å}$. The corresponding oscillator strengths are $\mathrm{f_{osc}} = 0.615$ and $\mathrm{f_{osc}} = 0.306$. For saturated absorbers with EW$> 0.15\,$Å, we derive a lower limit on the MgII column density (see Table 3.1).

3.4 Results

3.4.1 The MgII-selected sample

We used the method describe in the previous section to compute the equivalent width of the detected MgII feature in the MgII-selected stack. The corresponding measurements are tabulated in Table 3.1 and the stacked spectrum in Fig 3.7. The detection of the MgII doublet in the stack validates the methodology by showing the very strong absorption of the MgII doublet present at the redshift of the clusters, and demonstrates despite the high velocity dispersions within the clusters, that the cold 10^4K gas can be traced by MgII absorbers observed in the spectrum of background quasars. The detected lines are strong and show indication of saturation. Given the saturated equivalent widths in the range 0.15 $<$ EW $<$ 2 Å(Churchill et al., 2000), we calculate a lower limit for the column density using equation 3.4. The resulting EW is of 0.35±0.015 Å for the MgII 2796Å line, with a column density $10^{12.92}$ cm^{-2}.

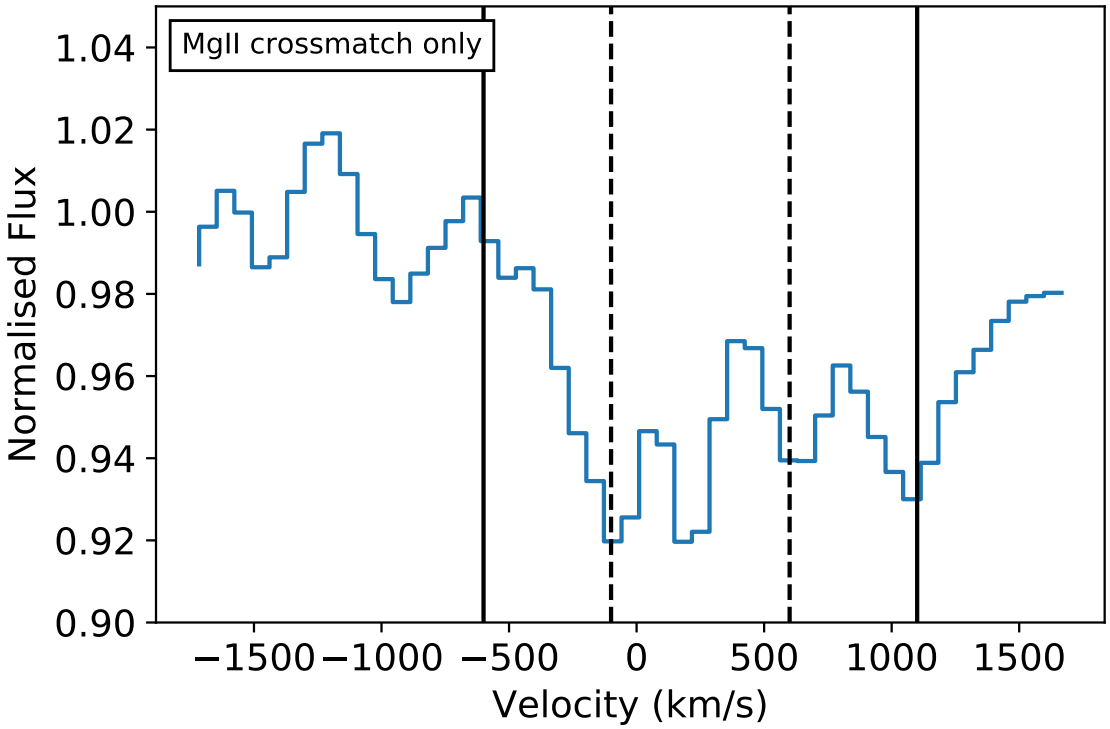

Figure 3.7: Stack of the spectra from our sample with known MgII absorbers from the MgII absorption catalogue of Anand et al. (2021), showing the normalised flux in velocity space. The first dashed line at -100km/s is fixed at the location of the minimum flux within [-2000:2000]km/s of the redshift of the known MgII absorber. The second dashed line is placed at +750km/s from the first dashed line, which corresponds to the separation of the two MgII lines in the doublet. The solid lines are fixed at -500km/s from 2976 and +500km/s from 2803 line.

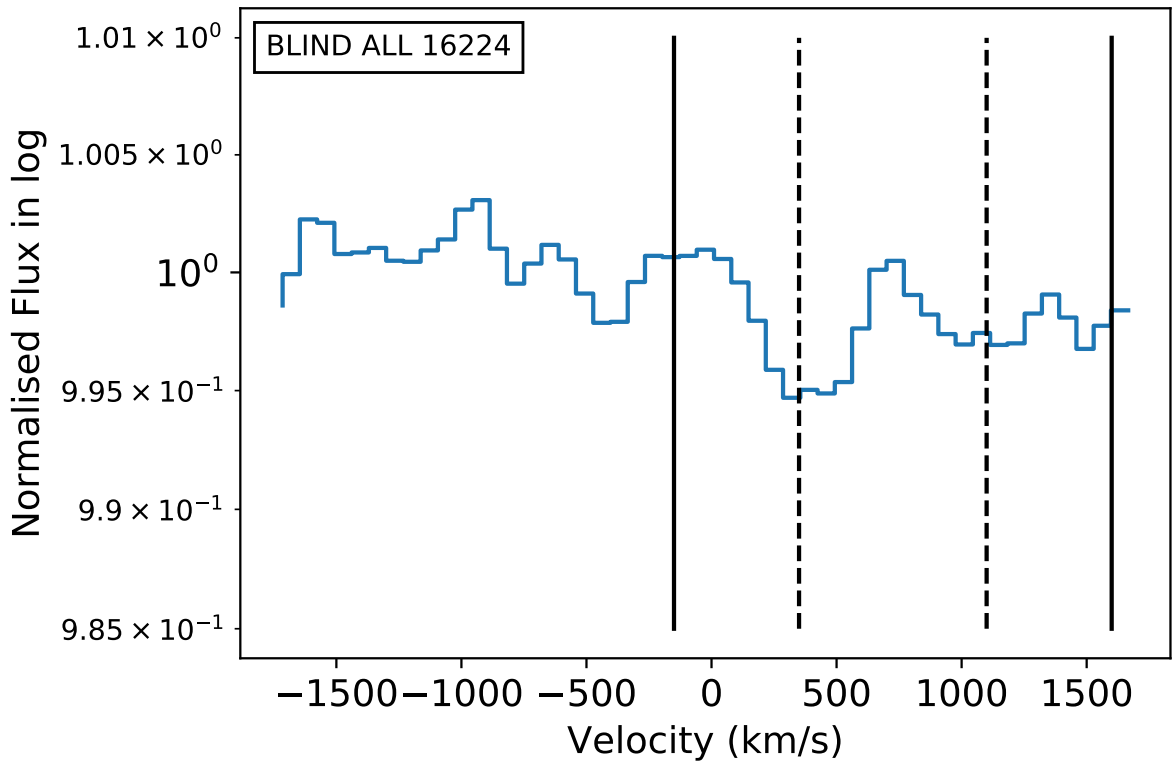

Figure 3.8: Blind sample stack of all the background quasars spectra available at the cluster redshift showing the normalised flux in log in velocity space. This sample comprises a total of 16,224 spectra and leads to a SNR of the stack of 195. The detection has a rest equivalent width of EW(MgII 2796)=0.056±0.015 Å (3.7σ significance), corresponding to a column density of log [N(MgII)/cm^{-2}] = 12.12 ± 0.1.

To remove the effects inherent to the a-priori knowledge of MgII, we also compute the *frequency-weighted* equivalent widths and column densities as follows: EW = EW$_{\rm rest}$f$_{\rm c}$, where the covering fraction, f$_c$, is defined as the number of spectra with known absorbers over the total number of spectra available for each bin of mass and angular separation. These values are listed in Table 3.1.

3.4.2 The blind sample

Figure 3.8 displays the stack of all the spectra with a total of 16,224 quasar-cluster pairs. It shows an absorption of the MgII doublet at the redshift of the cluster center, with a rest equivalent width for MgII λ2796Å of 0.056 ± 0.015Å (3.7σ significance), and a column density of log [N(MgII)/cm^{-2}]=12.12 ± 0.1 . We note that the absorption is redshifted from the cluster center, by 350 km s^{-1} from the absorption line center. The uncertainty in the measurements was calculated by randomizing the redshift of the clusters and doing

Table 3.1: Properties of the two stacks performed. The table lists the number of background quasar spectra stacked. The column of number of quasar spectra corresponds to the fraction quasars over the entire number of spectra with its representative percentage. The column density for the MgII selected sample is frequency-weighted, considering the number of spectra used. Possible saturation (at EW > 0.15 Å) leads to a lower limits for the column density for the MgII selected sample. MgII absorption is tentatively detected in the blind stack. This tentative detection provides a measure of the column density which relates to the amount of cold gas in galaxy clusters.

Sample	# Quasar Spectra	Mean MgII Redshift	SNR MgII sample	EW MgII 2796 Å	EW MgII 2803 Å	MgII Doublet Ratio	Col Den 2796 log N(MgII) cm^{-2}	Col Den 2803 log N(MgII) cm^{-2}	Frequency Weighted 2796 log N(MgII) cm^{-2}
MgII selected	32/16224=0.2%	0.51	73	0.35 ± 0.015	0.19±0.015	1.8	12.92	12.95±0.1	≥ 10.22
Blind	16224 =100%	0.45	195	0.056 ± 0.015	0.024 ± 0.015	2.3	12.12 ± 0.1	12.05 ± 0.1	12.12 ± 0.1

the stacking repeatedly as described in section 3.4.4.

The mean mass of clusters contributing to the stacked spectra is 9.7×10^{14} M$\odot$ (M_{500}), and a mean angular separation of the quasar-cluster pairs is about $2 \times R_{200}$.

The detection is broad, ranging over 1,000 km/s in width for each line. This is likely the result of the offset in velocities in the different clusters along the background sightlines. In addition, we computed the stack of the blind sample after removing the known MgII absorbers. We find that the absorption features remain largely unchanged.

3.4.3 Mock Sloan spectra with Simulated MgII Absorbers

In order to quantify the systematic uncertainty of the method and derive an error on the equivalent width measurements, we use 22,000 SNR=200 mock Sloan stacks representative of the signal-to-noise ratio achieved with our observed stack. We additionally inserted MgII absorber doublet from Illustris-TNG50 cosmological magnetohydrodynamical simulations. To compute MgII, we take the total magnesium mass per cell as tracked during the simulation, and use CLOUDY (Ferland et al., 2017) to calculate the ionisation state assuming both collisional and photo-ionisation following the modeling approach of Nelson et al. (2020). We then ray-trace through the simulated gas distribution to create synthetic absorption spectra, akin to those in real observations (Szakacs et al. submitted, Nelson, in prep). This is similar in spirit to several other techniques for creating absorption spectra from hydrodynamical simulations, e.g. SPECWIZARD (Theuns et al., 1998; Schaye et al., 2003), TRIDENT (Hummels et al., 2017) and PYGAD (Gad, 2021). The absorbers are inserted at a given wavelength position but with different equivalent widths, ranging from 0.05 to 5 Å. We used these mock spectra to run the same search and measurement algorithm as the one used for analysing the observations. Our results show that in 22,000 mock MgII stacks, only 3% of the detected absorption as found by the minimum-flux pixel approach are not associated with a simulated input MgII line. This means the code finds the min-

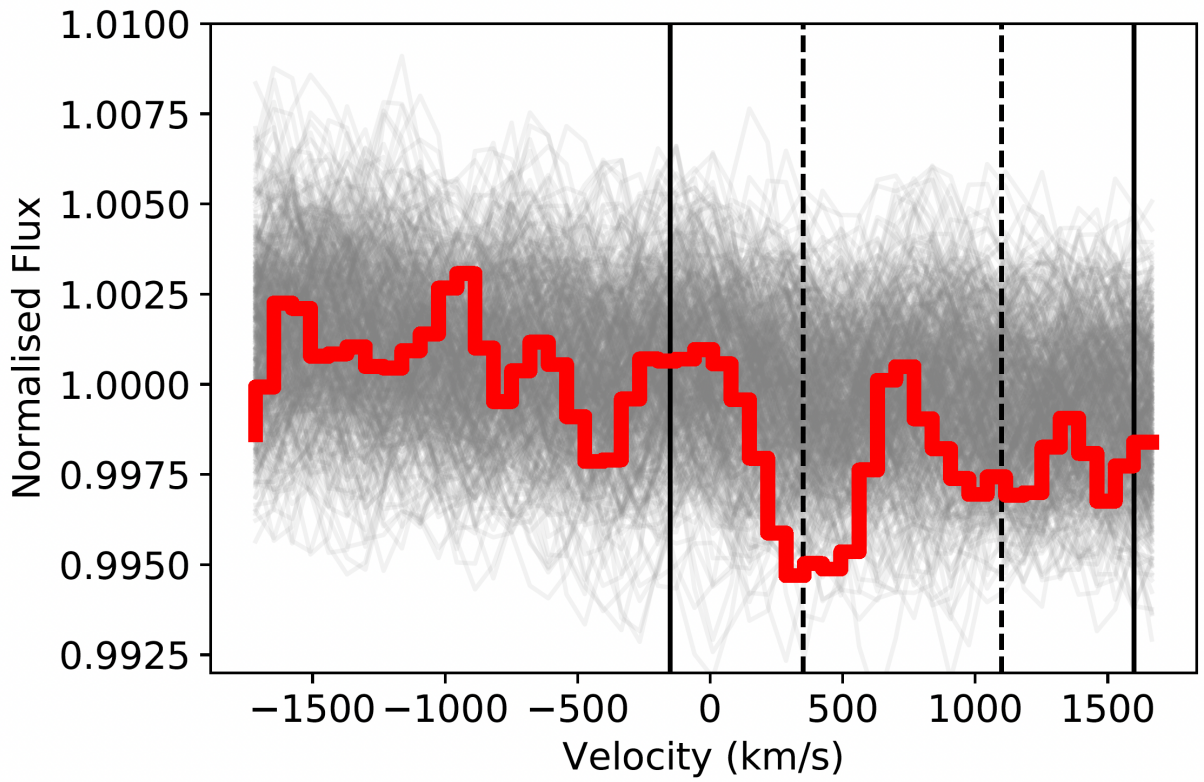

Figure 3.9: Plot of 500 random stacks from the bootstrapping in grey. The stacks are from the same sample of 16,224 quasar-cluster pairs, stacked at randomised redshifts from the full redshift distribution. On top, we overplot in red the original blind stack from Figure 3.8 to illustrate the difference.

imum flux outside of the area [-2000:2000]km/s where the MgII doublet should be located at a given redshift.

We then measure the EW of the simulated spectra with the method used to analyse the observations. We find that the equivalent width measurement from our analysis are consistent with the input equivalent width from the simulations. The analysis also indicates that the mean difference between the measured values and the input equivalent width is 0.013 Å for equivalent widths typical of the one we measure in the blind stack. This is similar to our estimated error in the blind stack of 0.015Å.

3.4.4 Uncertainty assessment from bootstrapping

In addition to using the mock spectra with simulated absorbers to quantify possible systematic errors of our method, we also performed non-parametric bootstrapping experiment, by stacking 500 times the full sample of quasar-cluster pairs at cluster redshifts that have been randomised. We then repeat the same measurement process mentioned in section 3.3, where we first find the minimum in the flux, and measure the equivalent width of

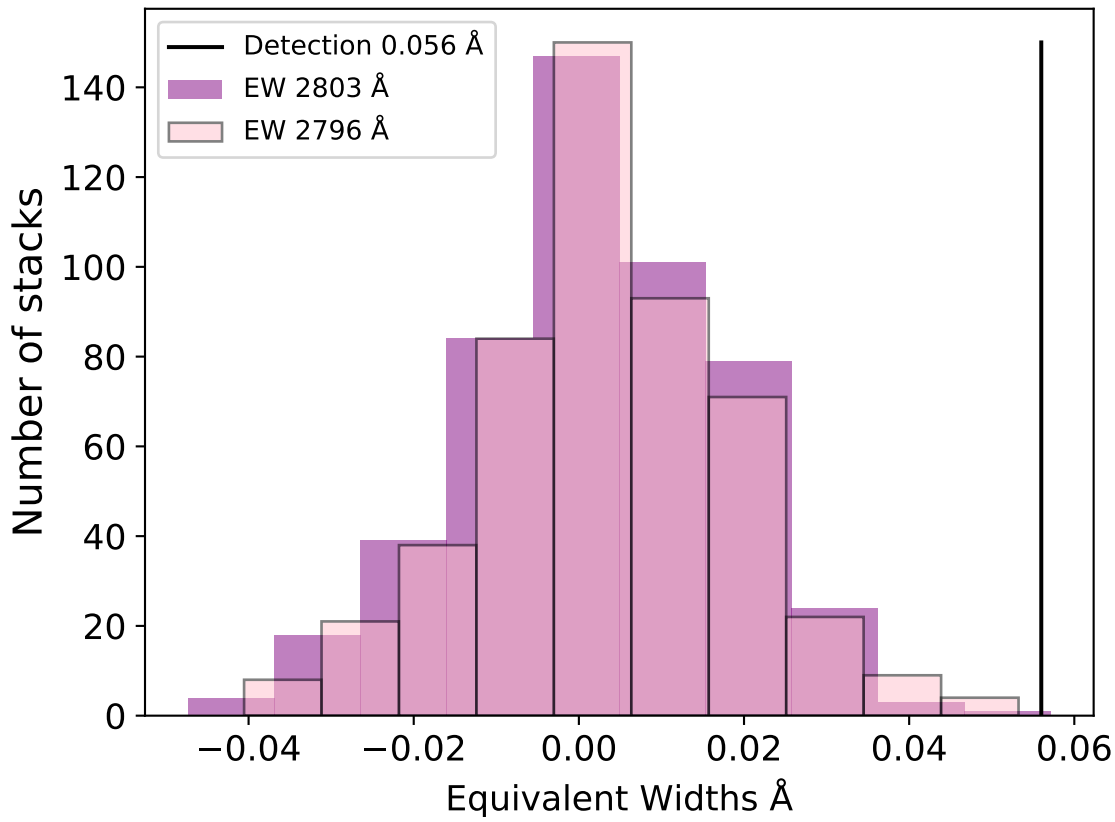

Figure 3.10: Histogram of the measurements of the equivalent widths of the 500 random stacks from bootstrapping for the MgII 2793 an 2803 Å lines, stacked at random redshifts from the cluster redshift distribution. We mark with a vertical line the position of our measurement from 2796 corresponding to 0.056±0.015 Å. We measure a standard deviation from the distribution of EW MgII 2796 of 0.015Å, which considering our tentative detection gives us a significance of 3.7σ.

the possible absorption feature. The results are shown in Figure 3.9, where the grey lines are the 500 stacks from the randomised cluster redshifts, and we overplot in red the blind stack from Figure 3.8. The results show that the stacks at random redshifts do not display absorption features at the level of the blind stack shown in red. This demonstrates that the detection is significant. Indeed, the measurement of the equivalent width of the blind stack is higher than the distribution of the measured equivalent width of the absorption features of the random stacks as seen in Figure 3.10. As expected, the distribution peaks around 0, since we do not expect any absorption feature at the random redshift we are considering.

Assuming a normal distribution we get a standard deviation from the equivalent width distribution of 0.015Å. Taking this as our measurement uncertainty, gives us a 3.7σ significance for the MgII 2796Å absorption feature.

3.5 Discussion

3.5.1 Evidence of cold gas in X-ray selected clusters

The detection of strong MgII absorption in the MgII-selected sample validates our approach of stacking many medium signal-to-noise background quasar spectra to increase the sensitivity to cold gas in clusters. This detection further demonstrates that, despite the high velocity dispersions within the clusters, the 10^4K gas can be traced by the MgII absorbers observed in the spectrum of background quasars. Our findings based on the blind stack of the full sample also indicate the presence of some cold 10^4K gas traced by MgII in the intra-cluster environment. We note that the CGM has a rather loose definition, so that whether these MgII absorbers are associated with the circumgalactic gas of individual galaxy members or the intracluster gas is somehow subjective. More important in this work is the total amount of 10^4 K cold gas that is being detected in the dense cluster regions.

To put our results into perspective, we plot in Figure 3.11 the equivalent width (left y-axis) and column density (right y-axis) of MgII absorbing gas as a function of the foreground cluster mass (upper panel) and the angular separation (lower panel), in comparison with similar studies, which we discuss further below.

3.5.2 Cold gas in galaxy clusters

Lopez et al. (2008) were the first to look for cold gas in foreground galaxy clusters using background quasar spectra, using a sample of 442 quasar-cluster pairs. To this end, the authors made use of the third data release of the SDSS with high-redshift cluster/group candidates from the Red-Sequence Cluster Survey. Lopez et al. (2008) found that there is proportionally less cold gas in more massive clusters than in low-mass systems, when using models of galaxy counts. This refers to the relation between overdensities of MgII absorbers in clusters with much denser galaxy environment. When considering the stellar

baryon fraction, studies still disagree on the exact slope of stellar and total baryon fraction as a function of cluster halo mass (Gonzalez et al., 2013). Nevertheless, the Lopez et al. (2008) results are in agreement with our findings, for the more massive structures of their sample ($M > 10^{14}$ $M_{\odot}$) the absorber overdensity is approximately twice as high as that of the less massive ones. At the same time, they point out that the more massive clusters contain a factor of 5 times more galaxies than the less massive ones. While searching for this cold gas through MgII absorption lines, their results show a sub-sample of their massive clusters yields a stronger and significant signal. Recently, Lee et al. (2021) performed a quasar-cluster cross-correlation with SDSS DR14 quasars and redMaPPer clusters, with a total of 82,000 quasar-cluster pairs. Although that work does not perform stacking of quasar spectra, the authors report that the MgII absorber detection rate per quasar is 2.70±0.66 times higher inside the clusters than outside the clusters. This shows that Mg II absorbers are abundant in clusters compared to the field.

Using galaxy clusters identified from Dark Energy Spectroscopic Instrument (DESI) LEgacy Imaging Survey cluster catalogue, a follow-up study led by Anand et al. (2022) cross-correlates the MgII absorption catalogue (Anand et al., 2021) with cluster and luminous red galaxies with a mass range between $10^{13.8}$ to $10^{14.8}$ $M_{\odot}$. Furthermore, Mishra and Muzahid (2022) cross-match the SDSS cluster catalogue of Wen et al. (2012) and SDSS quasar catalogue of Lyke et al. (2020). The median impact parameter of the clusters from the quasar sightlines is 2.4 Mpc (median 3.6 R_{500}). The authors were the first to resort to the stacking of the background quasars to increase the sensitivity of the experiment. In that work, the authors measured the total equivalent width and assumed that the observed MgII line falls on the linear part of the curve-of-growth so that the EW(MgII 2796) is 2/3 of the total EW.

Figure 3.11 displays our results together with the equivalent widths of Anand et al. (2022). The upper panel of Figure 3.11 shows these quantities as a function of cluster mass. Clearly, their work probes a lower mass range than our study. We compare the median of the two closest numbers in angular separation (~ 2 R_{500}) from Anand et al. (2022), and the closest point from Mishra and Muzahid (2022) with our tentative detection (orange hollow circle), in mass range. Our higher equivalent width measurements and limits could be associated to the higher mass in our sample, as shown in the figure.

The lower panel of Figure 3.11 displays the equivalent width from the blind sample in our work, compared to the values reported by Anand et al. (2022) and Mishra and Muzahid (2022) in different values of angular separation.

Despite the difference in approaches, the reported equivalent width is in line with results from Anand et al. (2022). The cluster masses in our study range from $M_{500} = 1 \times 10^{14}$ to 8.4×10^{15}, with a median EW of 0.056±0.015 Å of MgII 2796 line. Using three times the number of quasar cluster pairs, the rest EW from Mishra and Muzahid (2022) remain one order of magnitude smaller than our measured rest equivalent widths from both of our MgII-selected and blind sample (Figure 3.11). The authors report a clear trend of decreasing EW with impact parameter.

Galaxy cluster outskirts are multiphase structures, where new infalling material could flow inwards along filaments and the cooler clumps could become more important (Reiprich

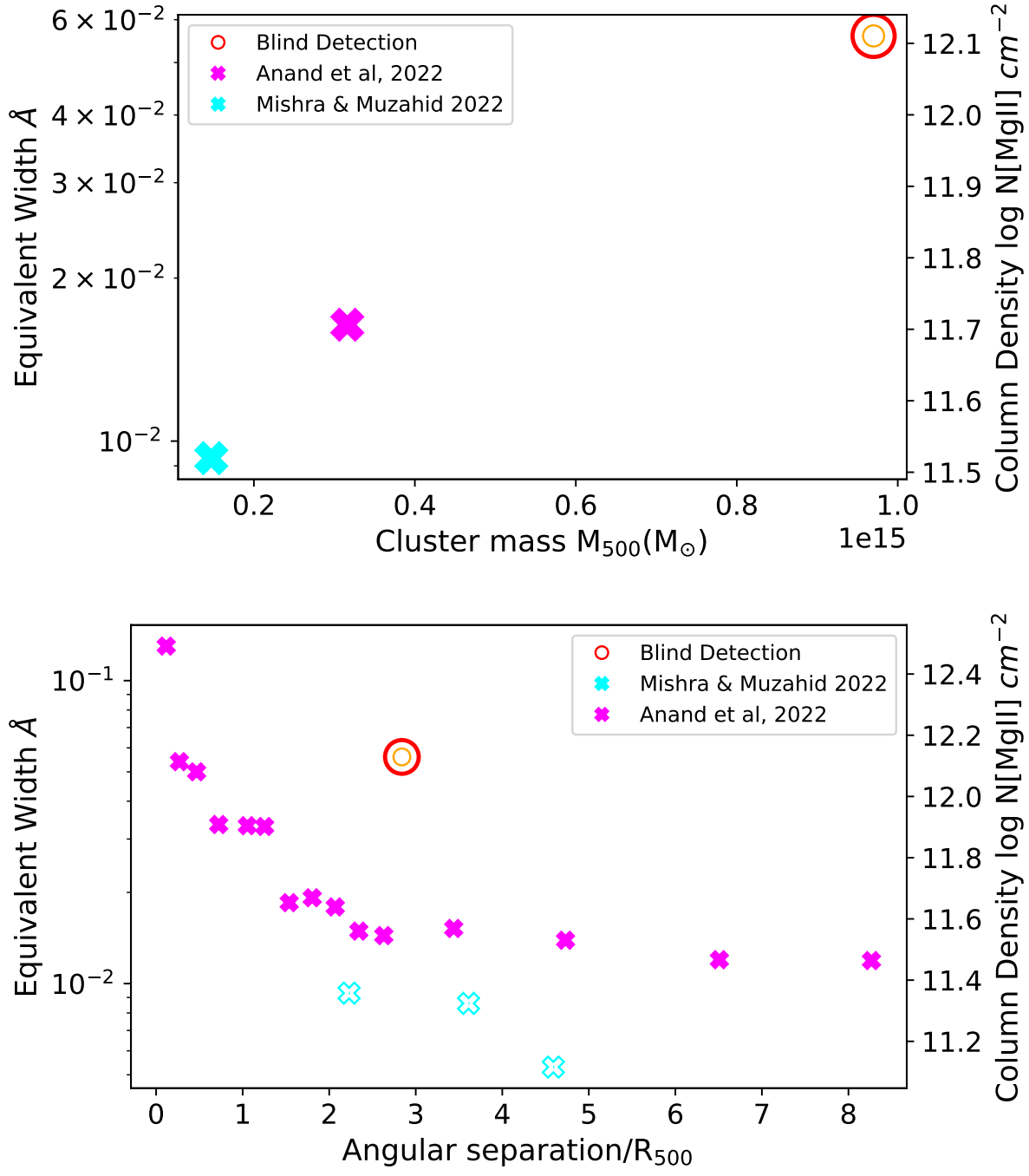

Figure 3.11: Equivalent width and column density from the blind sample compared with results from the literature (Anand et al., 2021; Mishra and Muzahid, 2022). The Figure shows the detection in the blind stack with a red circle. We also plot the mean of the two points of Anand et al. (2021) closest to the same points in angular separation, and the point of Mishra and Muzahid (2022) from the same angular separation in the upper panel. This highlights the difference in mass range between samples. The lower panel displays the detection in the blind sample as a function of angular separation.

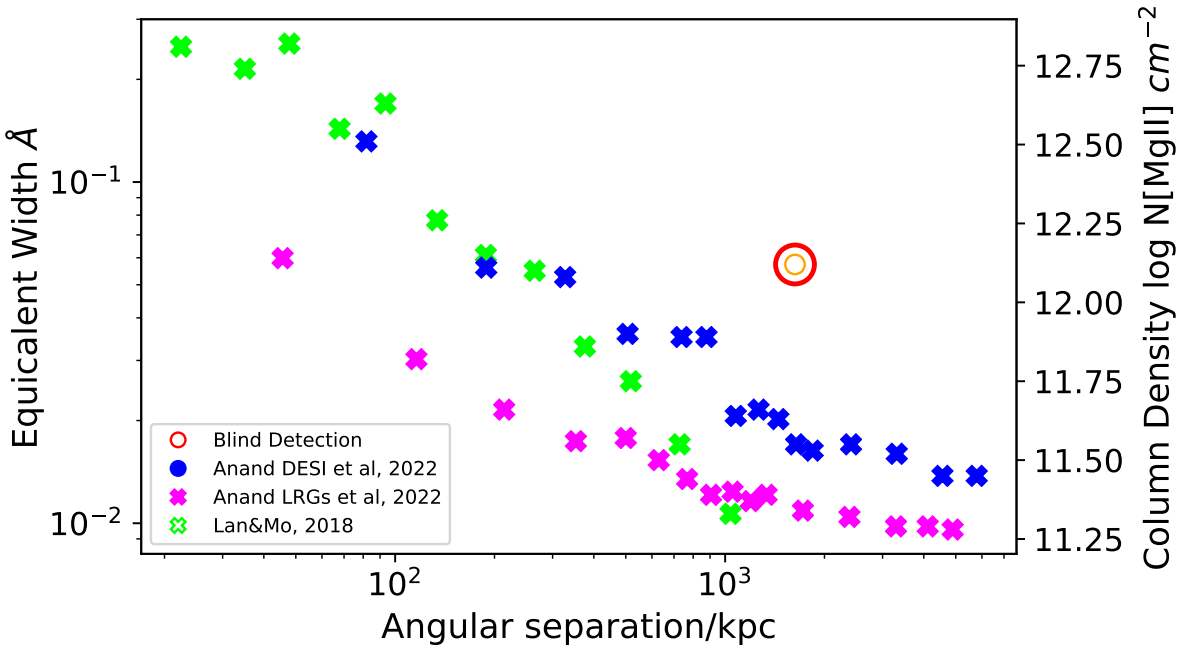

Figure 3.12: Comparison between our results with measurements of column density and equivalent width of MgII absorption in LRGs from Lan and Mo (2018), LRGs and cluster samples from Anand et al. (2022), and our tentative detection from the blind sample.

et al., 2013). The gas density distributions in this multiphase structure depend on several properties such as temperature and dynamical state, and there exists a very steep relation between gas mass and temperature that implies a decrease in the total gas mass content of cooler clusters relative to higher mass systems (Croston et al., 2008).

Finally, Figure 3.12 contrasts our results with both observations and simulations of lower mass structures as traced by Luminous Red Galaxies (LRG). Anand et al. (2022) also compare the EW from the DESI clusters with Luminous Red Galaxies (LRGs) from SDSS DR16 as a function of projected distance, where the LRGs, with lower masses ($\sim 10^{11.2}$ $M_\odot$) are shown to have on average lower MgII absorption strength than the clusters. Although they seem to converge at large projected distances, they report this difference as being due to the larger halo masses and denser environments in the cluster sample. In comparison, our tentative detection has an EW similar to the highest measurement found closest to the cluster centre in the sample of Anand et al. (2022). We may also attribute the difference in EW to the mass difference, since our sample of clusters has a higher mean mass than theirs (see upper panel of Figure 3.11).

While there still exists disagreement in the trend of total baryon fractions as a function of cluster mass (Gonzalez et al., 2013; Laganá et al., 2013), the difference in mass from all the previously mentioned studies with our work, in connection with the higher measurements from equivalent width from our higher cluster mass sample, shows the dependence of increased baryon fraction at higher cluster masses. These differences in gas measurements for halos of different mass can also be seen when comparing galaxies versus galaxy clusters as shown in Figure 3.12. Similarly, Anand et al. (2022) perform a direct comparison of LRGs with the DESI cluster sample of MgII measurements, finding consistently higher equivalent widths in the cluster sample than in the LRGs, where the clusters are 2 - 3 times more massive than LRGs within R_{500}.

3.5.3 Comparison with simulations

Butsky et al. (2019) used the RomulusC simulations (Tremmel et al., 2019) to probe the nature of the multiphase cool-warm ($10^4 < T < 10^6$K) gas in and around one galaxy cluster of mass 10^{14} $M_\odot$. This study makes predictions for the covering fractions of key absorption-line tracers, both in the intra-cluster and in the circumgalactic medim of cluster galaxies using synthetic spectra. Butsky et al. (2019) finds there is a significant quantity of multiphase gas in the cool (10^{4-5}K) at all clustocentric radii. Their results indicate that the column density of all ions decline from the cluster center out to 1 Mpc, but remain relatively flat towards the edge of the halo.

In Figure 3.13, we compare our results with the TNG50 simulation (Pillepich et al., 2019; Nelson et al., 2019), from the IllustrisTNG suite (Marinacci et al., 2018; Springel et al., 2018; Naiman et al., 2018; Nelson et al., 2018; Pillepich et al., 2018). IllustrisTNG aims to study the physical processes that drive galaxy formation and to study how galaxies evolve within large scale structures. TNG50 is a gravomagnetohydrodynamics (MHD) cosmological simulation including a comprehensive model for galaxy formation physics (Weinberger et al., 2018; Pillepich et al., 2018) at the highest resolution. TNG50 includes

2×2160^3 resolution elements in a $\sim$50 Mpc (comoving) box. Nelson et al. (2020) make predictions of the physical properties of the cold gas traced by MgII in the circumgalactic medium of galaxies and groups at z = 0.5 based on these TNG-50 simulations. By identifying discrete structures of cool, MgII-rich gas, the authors found that cold gas in these massive halos is made up of thousands, to tens of thousands, of small (kpc), discrete clouds. The results also indicate a tendency where the most massive halos have the highest covering fraction, while the highest column densities are located near the halo centre, where the gas densities are greater. Figure 3.13 shows the results in terms of column density of MgII as a function of impact parameter from the cluster. The conversion of angular size from R_{500} in degrees to linear size in kpc, at a given redshift, was performed using cosmological parameters from Planck Collaboration et al. (2020). We note that the simulations probe significantly smaller impact parameters than our observations. Equally, we stress that there are large mass differences between the models and the data: the TNG50 highest mass bin ($\sim 10^{13.5}$ $M_\odot$) displayed in the figure is smaller than our smallest mass cluster (3.28×10^{14} $M_\odot$). Considering this mass difference, and the observed increase in the cold as column density as a function of cluster mass, we note here a possible disagreement and a likely excess of MgII-absorbing cold gas in the TNG50 simulations compared to observations.

3.5.4 Forward looking

The analysis presented here stems from the ambitious endeavours of the Sloan Digital Sky Survey, SDSS. This series of multi-object surveys, based on extremely large surveys of thousands of quasar absorbers have brought quasar studies to a new era (e.g., Noterdaeme et al., 2012; Bird et al., 2017; Parks et al., 2018). Such surveys advanced the field significantly because they produced homogeneous data products for well over one million low-resolution quasar spectra. In the near future, dedicated spectroscopic surveys on 4-m class telescopes will provide a wealth of new low and medium-resolution quasar spectra in extremely large numbers, notably the DESI experiment (DESI Collaboration et al., 2016), the WEAVE-QSO survey (Kraljic et al., 2022), and surveys with the 4MOST experiment (Merloni et al., 2019). In collaboration with new generations of X-ray missions, including the full eROSITA survey (Merloni, 2012), X-ray imaging and Spectroscopy mission (XRISM) (XRISM Science Team, 2022), ESA/Athena (Nandra et al., 2013), the study presented here can be expanded greatly by not only increasing the number of background quasar spectra, but also by increasing the spectral resolution of these data. We note that the latter is key as the equivalent width limit of detectable absorbers scales linearly with spectral resolution, and a 1 dex increase in equivalent width provides a factor of 10 more absorbers.

3.6 Conclusions

In this work, we have used background quasar spectra from the SDSS/SPIDERS survey, to explore the cold gas content of foreground massive X-ray selected galaxy clusters. To

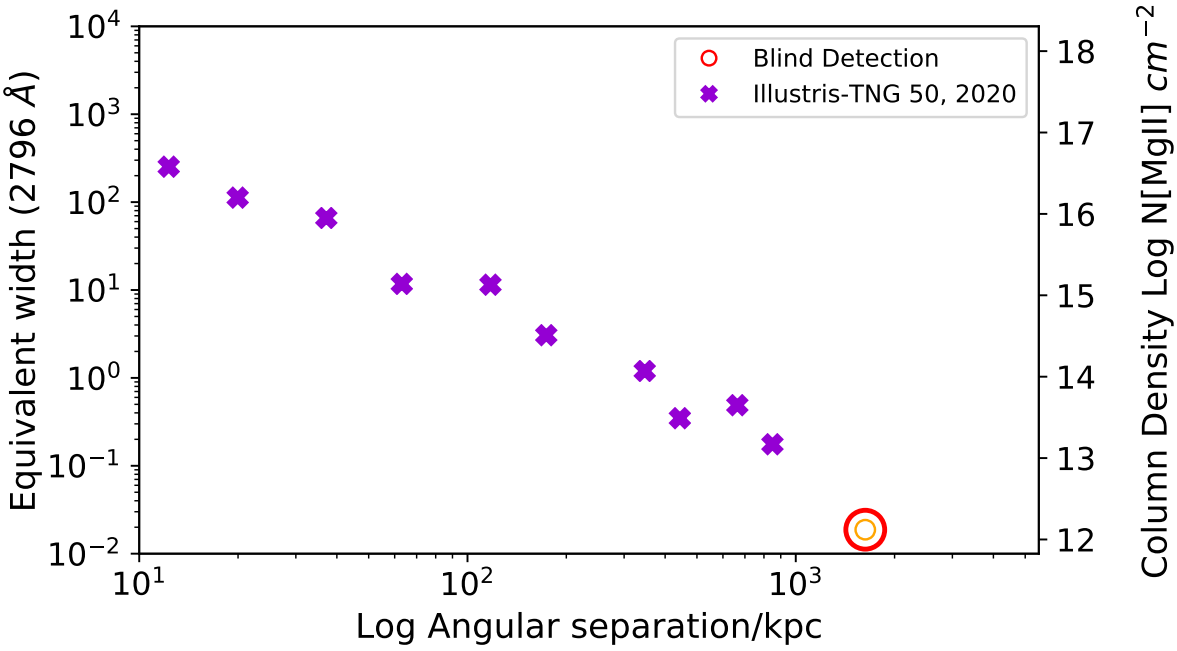

Figure 3.13: Comparison between our blind stack with hydrodynamical cosmological simulations from TNG50. The shape and colour of the symbols are as in previous figures. The purple symbols displays predictions of the MgII column density in TNG50. We stress that there are large mass differences between the models and the data: the TNG50 highest mass bin ($\sim 10^{13.5}$ $M_\odot$) displayed in the figure is smaller than our smallest mass cluster (3.28×10^{14} $M_\odot$). Considering this mass difference, we note there is a likely excess of MgII-absorbing cold gas in the TNG50 simulations.

this end, we stacked $\sim 16,000$ quasar spectra in the quasar sightline. Our main results are:

- From the sample of known MgII absorbers within [-2000:2000] km s^{-1} of the clusters, we detect strong absorption rest equivalent width for MgII λ2796 of EW=0.35±0.015 Å. The uncertainty is calculated through bootstrapping. Since the absorption lines are saturated (at EW>0.15 Å) we derive a lower limit for the column density of log [N(MgII)/cm^{-2}]≥12.92. These results validate the technique and demonstrate that despite the high velocity dispersions within the clusters, the cold 10^4K gas can be traced by MgII absorbers observed in the spectra of background quasars.

- We then stack quasar spectra without a-priori knowledge of the presence of absorption systems (so-called blind sample). We tentatively ($\approx 3.7\sigma$ significance) detect MgII absorption signal by stacking a total of 16,224 quasar absorber-cluster pairs within [-2000:2000] km s^{-1} from the clusters, with EW= 0.056 ± 0.015 Å, corresponding to a column density of log [N(MgII)/cm^{-2}]=12.12±0.1 cm^{-2}.

- While we are probing a different cluster mass range, our results are in line with observational findings previously published in the literature (Lee et al., 2021; Anand et al., 2022; Mishra and Muzahid, 2022). We also report an excess of MgII gas in the predictions from TNG50 hydrodynamical cosmological simulations (Nelson et al., 2020) compared to our work, and to others with lower mass objects in their sample (Anand et al., 2022; Lan and Mo, 2018).

Using a similar approach of stacking in up-coming surveys with increased spectral-resolution and number of background spectra (DESI, DESI Collaboration et al., 2016), WEAVE (Kraljic et al., 2022) and 4MOST (Merloni et al., 2019) combined with new generation of X-ray facilities (most notably eROSITA (Merloni, 2012) on-board SRG) will likely provide additional insight into the cold gas content of galaxy clusters. On the simulation front, TNG50 profiles could be extended out to angular separation of 4000 kpc, so as to overlap with the observations. Further, using TNG100 or TNG300, would - thanks to their larger cosmological volumes - provide a sample of halo masses which overlap with our observations, so as to assess the importance of the reported halo mass mismatch.

Chapter 4

Tracing AGN outflows through intrinsic MgII absorption

4.1 Introduction

Luminous quasars are powered by accretion onto billion solar mass black holes, that have existed already since the Reoinization epoch (Bischetti et al., 2022). Any model of active galactic nuclei (AGN) needs to be able to explain a wide range of spectroscopic properties and the physical processes responsible for them (Elvis, 2000). Among these properties are broad emission lines, broad absorption lines, narrow absorption lines, caused by the excitation of various line and continuum-emitting regions, and by the launching mechanisms of outflows, which can provide feedback energy to the host galaxy (Temple et al., 2023).

Studying absorption systems with redshift close to the QSOs can yield important information for understanding the energetics and kinematics of matter near the black hole, as well as the ionization structure, dust content and metal abundances that remain under the influence of QSO radiation. We call the absorbers physically associated with the QSO against which they are detected "intrinsic absorbers". These systems are located within a few kpc of the galactic nucleus, or in the very core of the AGN. They manifest themselves as narrow or broad absorption lines within several thousand km/s of the emission redshift of the QSO. Direct evidence for a close physical relationship between these absorption systems and the AGNs can be time-variability of the line strengths, observations of partial coverage of background emission source or smooth and broad line profiles.

Tremendous amount of effort has been put into trying to understand and explain the differences in continuum and emission-line of quasars (Richards et al., 2011). Among the most common prominent features in quasar spectra from the resonant ultraviolet transitions are HI, OIV, NV, CIV and SiIV (Murray et al., 1995). Broad absorption line (BAL) quasars are an important sub-population of AGNs, and the broad absorption lines are generally blueshifted with respect to their emission counterparts (Weymann et al., 1991). BALs can also be classified into subcategories according to these absorption features. High ionization

BALs, showing absorption in NV 1238Å , 1242Å , Si IV 1393Å , 1402Å and C IV 1548Å , 1550 Å make up for the majority of the BAL quasars (around 85%). The remaining 15% are low ionization BAL (LoBALs) show Mg II 2796Å , 2803Å , and Al III 1854Å , 1862Å on top of the HiBALs features (Liu et al., 2015).

Since the majority of BALs exhibit highly ionized CIV λ1549 (Rankine et al., 2021), there are a large number of studies that have been using this broad absorption feature over the years (Wills et al., 1993; Brotherton et al., 1994; Kruczek et al., 2010; Rivera et al., 2020; Rankine et al., 2021; Temple et al., 2023). These studies focus on analysing the line width of broad CIV absorption line, the equivalent width and peak-to-continuum intensity ratio, the profile shape, the line asymmetry, and the ratio with other lines changes (Wills et al., 1993) in order to describe AGN properties. Among these, two properties of CIV stand out: equivalent width (EW) and blueshift. The changes in their properties can describe models of a two-component structure of disk-wind in AGNs (Richards et al., 2011; Wang et al., 2011).

High-ionization lines such as CIV tend to be blueshifted with respect to low-ionization lines, as well as showing strong blue excess asymmetry (Baskin and Laor, 2005). Other emission lines can also be used to measure more accurately the CIV line properties, such as He II, Al III, Si III, C III, and Mg II (Rivera et al., 2020). In an attempt to reconcile models of outflows and gravitationally bound broad emission lines that are usually contradictory (Gaskell et al., 2008), direct comparison of line properties of MgII and CIV have been studied. One study found that although these two lines coexist in tbe emitting region of AGNs, there are structure and kinematic differences from the CIV high-ionization lines, and the MgII low-ionization line regions, and interpret MgII region as gravitationally bound, making an outflow model of low-ionization regions unlikely (Wang et al., 2011). Other studies of MgII broad line region itself also revealed the broad line originates from two subregions: one which contributes to the line core, and the other with outflows-inflows that are nearly orthogonal to the disc, which become suppressed with stronger gravitational influence (Popović et al., 2019).

In this chapter we target the MgII intrinsic absorption line close to the quasar redshift, and stack the spectra of a large number of quasars, searching for evidence of outflows connected to the AGN. The chapter is organized as follows: Section 4.2 presents the observational data. Section 4.3 details the stacking method. In Section 4.4 we summarise results and present future ideas on how to continue further in this work. Throughout the work, we adopt an H_0 =70 km s^{-1} Mpc^{-1}, Ω_M =0.3, and Ω_Λ = 0.7 cosmology.

4.2 Observational Data

The eROSITA Final Equatorial-Depth Survey (Brunner et al., 2022) was a Performance Verification program from the SRG/eROSITA telescope meant to demonstrate the survey science capabilities of eROSITA. The observations of the 140 deg^2 survey field were performed in 4 days of November 2019, reaching an X-ray depth of $\sim 6 \times 10^{-15}$ erg/s/cm^2 in the soft eROSITA band (0.2-2.3 keV), and detecting more than 27,000 distinct X-ray

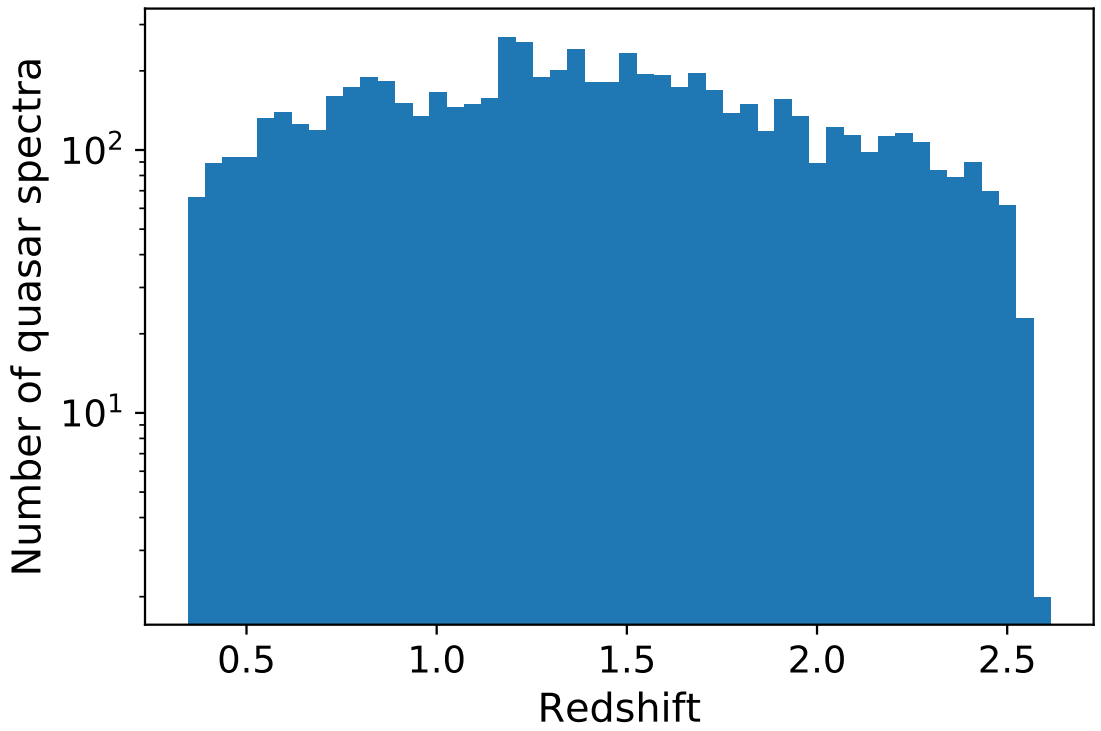

Figure 4.1: Histogram of number of quasars as a function of redshift for the eROSITA early data release SDSS DR18 sample $\sim$ 7100 quasar spectra used in this work.

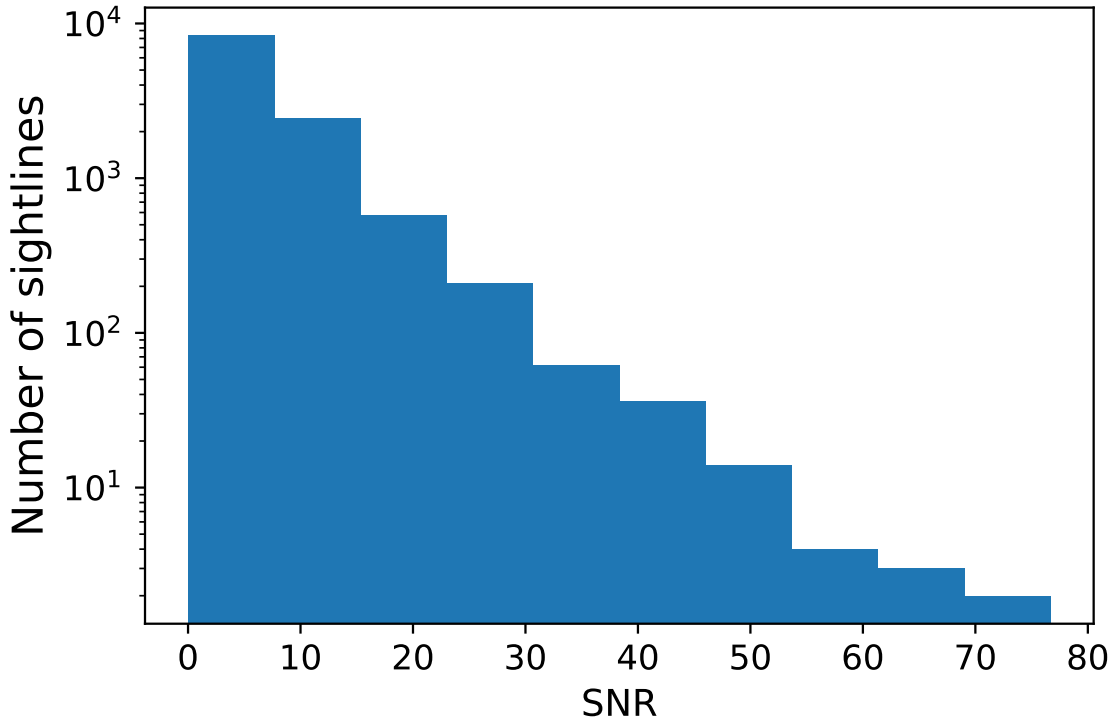

Figure 4.2: Distribution of the median SNR of the individual quasar spectra from SDSS eFEDS QSO sample.

point sources. In this work we made use of the quasar spectroscopic observations from SDSS (DR18) covering the fields of eFEDS, with a total of 11,000 quasar spectra (Merloni et al., in prep.). The redshift distribution of the spectra used ranges from z$\sim$ 0.5 to $\sim$ 2.5, constraints that come from the wavelength coverage and the quasar redshift, and the histogram is displayed in Fig 4.1. The spectra cover a wavelength range from 3600Å to 10,400 Å at a spectral resolution of $\lambda/\Delta\lambda$ $\sim$2000, or with the SDSS-I instrument, covering 3800 Å to 9100 Å, with the same spectral resolution. As mentioned above, the SDSS spectra have a common grid of logλ_{i+1}-logλ_i =0.0001, which translates to an average Δv= 69km/s. Considering the location of MgII λ 2796 Å and λ 2803 Å at the redshift of the AGN, the total number of AGN spectra available where MgII is observable over a velocity range of [-15000:15000] km/s around the systemic redshift is $\sim$7100 spectra. The signal to noise ratio from the chosen spectra is shown in Fig 4.2, where the median SNR is < 10. We do not set a minimum SNR below which data is rejected.

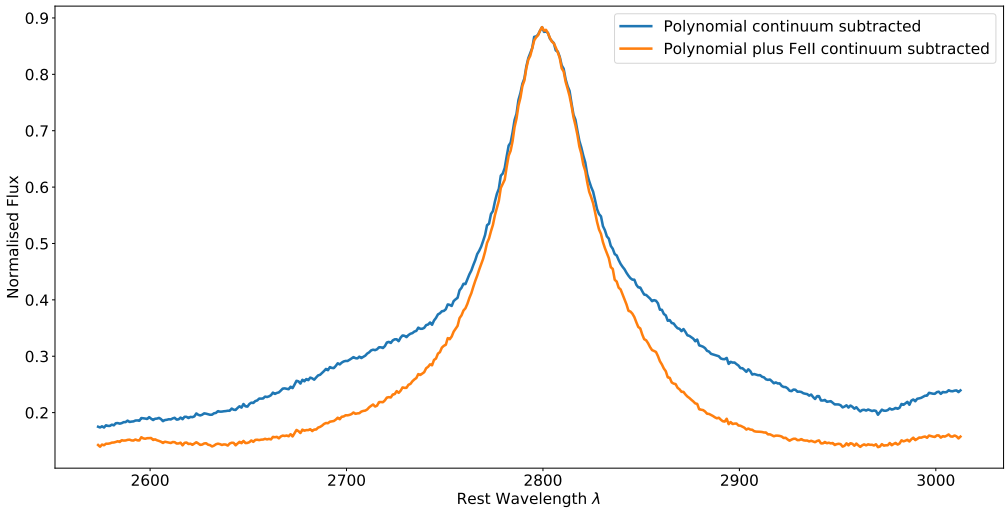

Figure 4.3: Plot of the full stack of 7100 SDSS QSO spectra in the region of MgII emission, using different continuum subtraction from PyQSOfit. The blue line includes a fitting of the polynomial continuum, where no FeII emission is included in the continuum fit. The orange line shows the polynomial plus FeII continuum subtracted. There is a clear excess in flux in the former case compared to the orange line in the area of the wings on both sides of the peak of the MgII line, as is expected due to the FeII.

4.2.1 Fit of the individual quasar spectra

In order to retrieve the quasar absorption systems, we remove the spectral signature from the background quasars. To this end, we model each of the SDSS quasar spectrum with the highly flexible Python QSO fitting code, PyQSOfit (Guo et al., 2018) in order to normalise the data. This algorithm fits the spectral features such as broad emission lines with multiple gaussians, and continuum of the quasars. By removing the emission features we can detect the absorption, by fitting and subtracting the quasar continuum (before stacking) from the original data results in a continuum-free spectrum, which is the approach we followed to study the MgII region. For some objects, the emission lines cannot be perfectly modelled, and after normalisation some wiggles remain. We note in particular that the noise of the SDSS spectra increases at each end of the wavelength window, resulting in equally noisy quasar spectra at these edges after normalisation. Nonetheless, the PyQSOfit proved very efficient to normalise a large number of quasar spectra with modest signal-to-noise.

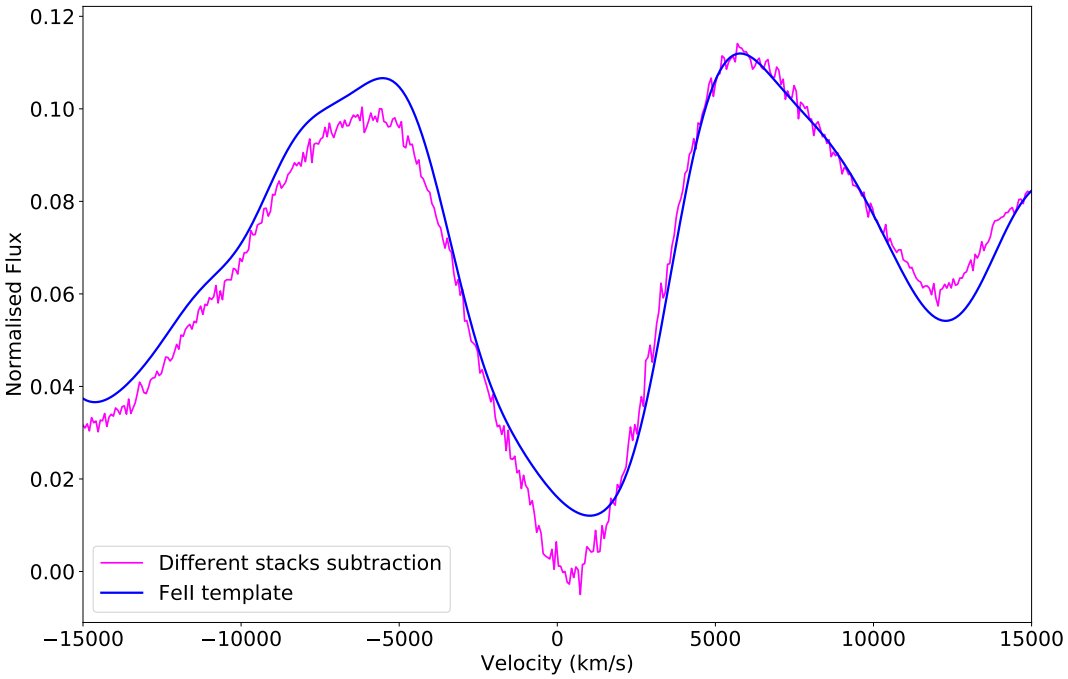

Figure 4.4: The pink line shows the flux in velocity space of the difference between the stack created using the polynomial continuum only and the stack obtained subtracting a continuum which includes the FeII emission (see Fig. 4.3). The blue line shows the FeII template which has been smoothed (with a Gaussian kernel and a dispersion of 10 pixels) and shifted in velocity space using the 2976 MgII line at Vel=0 km/s. The plot shows a similarity in the shape of the two curves, but with a noticeable difference between the two in the normalised flux.

4.2.2 Stacking at the quasar redshift

In order to detect the absorption lines on top of the emission lines, we take advantage of the large amount of spectra available, to stack quasar spectra. To this end, we stack the spectra at the redshift of the quasars. We use the fact that all the SDSS spectra have a constant log step to avoid interpolating between pixels. Following the method of Fresco et al. (2020), we perform a median stack in the velocity region within a window of [-15000:15000] km s^{-1} around the rest-frame MgII emission. After this process, a gaussian smoothing of 1 pixel was applied using GAUSSIAN SMOOTH in SPECUTILS.

4.2.3 Analysis

The continuum subtraction using the standard parameters from PyQSOfit did not fully remove the emission features around our area of interest in the wavelength range of the MgII doublet ($2500 < \lambda < 3000$ Å). For this reason, we proceeded to compare two different types of continuum subtraction in the stack as shown in Fig 4.3, one using a polynomial function to fit the continuum underneath MgII (blue line), and another using a more complex continuum which includes fitting a polynomial, UV Fe component on the continuum from 1200 to 3500Å (Boroson and Green, 1992), the optical FeII on the continuum from 3686 to 7484Å (Vestergaard and Wilkes, 2001), and Balmer continuum (orange line). It can be seen in the plot that, as expected, the main difference between the two stacks is due to a broadened FeII template. There is an excess in flux in the blue (polynomial continuum subtracted) when compared to the orange (polynomial plus FeII continuum subtracted) in the wings. There is also an asymmetry on the shape of the emission, where the right hand side shows a bump on the wing, while the left hand side shows a sharp drop in flux.

In order to probe the cause for the differences between the two cases, we subtract the polynomial continuum subtracted stack from the full continuum subtracted stack. The results can be seen in Fig 4.4, where the pink line is the result from the subtraction of the two stacks. The blue line shows a plot of the UV iron template used in PyQSOfit (Guo et al., 2018), smoothed with σ=10 pixels (or 690 km/s). The FeII template broadly reproduces the difference, with some notable residual offset between the two curves. This shows that there is indeed some residual iron even after the fitting, which becomes clearer after performing the stack. Since we are looking for absorption features of MgII doublet that are very close to these iron lines, we need to make sure we remove any contamination of iron as best as possible before being able to detect absorption features. To this end, we subtract an additonal FeII contamination to the MgII stack created by subtracting the full (polynomial plus FeII) continuum. We note that the subtraction is only done on the stacked spectra, and not on the individual spectra. The physical reason for this extra step is that while the main component of the FeII emission is broad, with dispersion comparable to that of the MgII line as seen in Figure 4.4, any additional narrower component of FeII will not be properly removed, as the PyQSOFIT continuum model include only one broadened FeII component.

In order to be able to optimally subtract the appropriate Iron template we interpolate

the FeII template to match the common grid of the SDSS spectrum. We then shift slightly the template both in y axis (flux) and x axis (velocity) to make the template fit the stacked spectrum correctly. To calculate the best fit of the iron template, we choose the area of the wings where the iron lines are more prominent vel[-12000:-8000] and vel[8000:13000] km/s. This reflects possible redshift uncertainties. We create a grid of possible x and y shifts for the FeII template, where the Velocity is moved in steps of 69km/s in the x axis 40 times, and the flux (y axis) is multiplied in steps of 0.01 for 60 times, for 6 different iron templates using smoothing from standard deviations ranging from 2 to 9 pixels (i.e. from $\sim$ 140 to $\sim$ 810 km s^{-1}). The variance of the subtraction of these shifts in the iron templates is then subtracted from the stack on the negative and the positive side of the array, and the sum of these variances is compared in this grid of 16000 possibilities. The minimum variance from the grid is y * 0.39 and x - 100km/s, with the iron template using the gaussian smoothing with standard deviation of 7 pixels (corresponding to $\sim$ 480 km s^{-1}). Figure 4.5 shows a zoom in on the wings of the polynomial continuum subtracted stack of the MgII line, with over-imposed models of the FeII UV templates, with the thick blue line representing the best FeII template fit from the variance grid. The other lines represent different shifts in the x and y axis of the iron template, to display the differences in the possible fits.

In Fig 4.5 we also see there is an emission feature around vel[-15000:-14000]. In a study using 2200 quasar spectra from SDSS, and applying the mean stacking of composite spectra (Vanden Berk et al., 2001), they identify common emission and absorption features in quasar spectra. They identify a strong emission of Al[III] and O[III] at $\lambda \sim 2750$Å. This emission looks consistent with the location of our emission feature.

On the right hand side of the initial stack in Fig 4.5, in the orange line around the area of vel[13000:15000], we can also see an emission feature that seems to fit the Iron template overplotted in the same figure. The SDSS composite spectra study (Vanden Berk et al., 2001) also identifies an absorption feature at the same location in the stacked spectra, at the right of the MgII emission at $\lambda \sim 2950$Å, confirming that this indeed might be related to FeII emission feature.

4.3 Results

Thanks to the large number of spectra, our MgII continuum-free emission line stack has a very high signal-to-noise (Fig. 4.3), and allowed us to further model (and remove) additional residual contamination from multiple FeII UV components of different velocity width.

After the subtraction of the residual iron UV template, we are left with a clean MgII emission line, and we would like to test whether any broad intrinsic absorption is present. In order to prove broad, blended absorption features, we search first for asymmetries in the emission line profile. To do this, we cut the flux from the right hand side of the emission at the peak of the emission and mirror it (4.6), in order to subtract the left hand emission side and thus test the level of asymmetry in the MgII emission line.

This means we grab the array of the flux from the right side (positive in velocity) and we

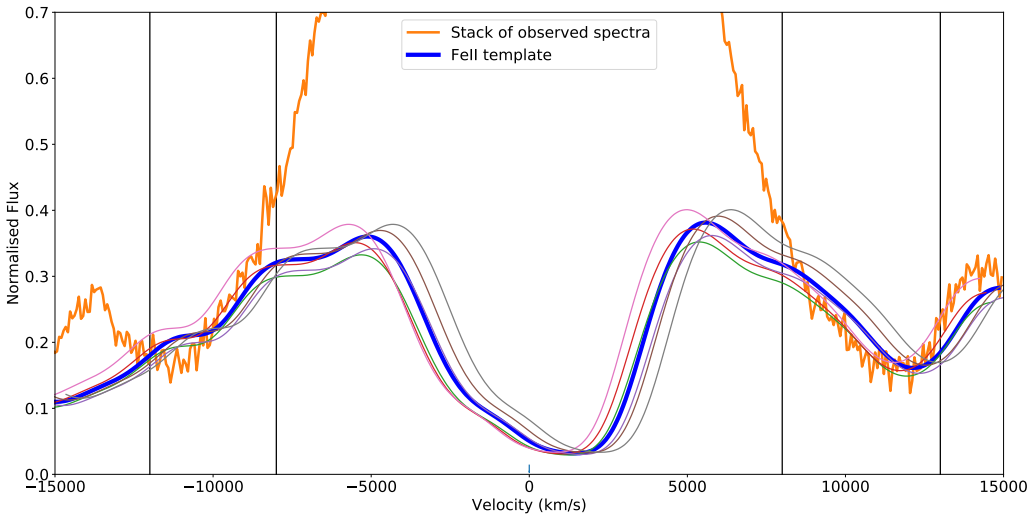

Figure 4.5: Zoom in on y axis of the polynomial plus FeII continuum subtracted from the from PyQSOfit as the orange line, with the best fit of the iron templates in a thick blueline that has a gaussian smoothing with standard deviation of 7 pixels (480 km/s), a flux * 0.39 and a velocity shif of -100km/s, and other fits of iron templates with different smoothing applied, the flux values in the range of x= 0.39 - 0.41, and a velocity shift in the range of +1000km/s and -1000km/s. The solid lines are fixed around our area of interest [-12000:-8000]km/s and [8000:13000]km/s, where we search for the minimal difference between the fittings of the FeII template and the stacked of the observed spectra in the grid. These values are the result of the best fit grid described in section 4.2.3.

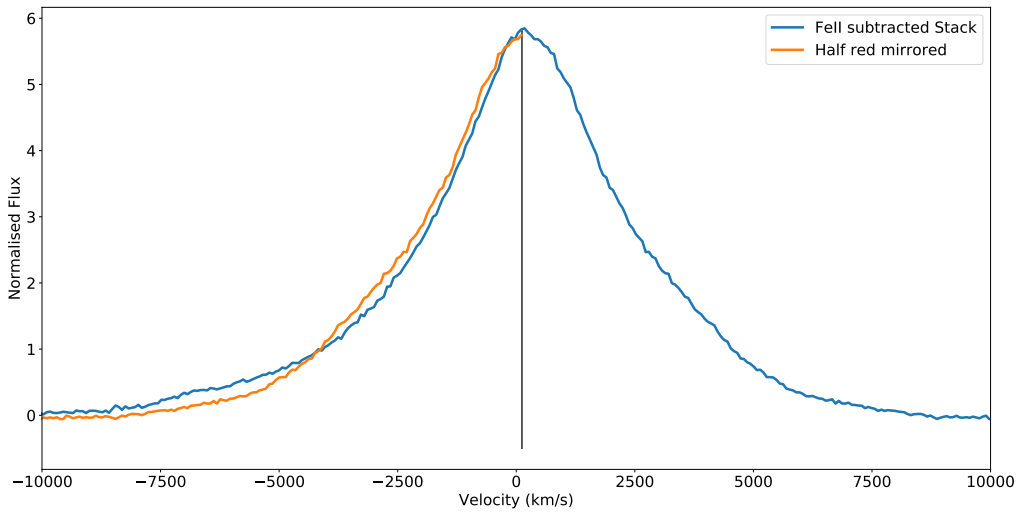

Figure 4.6: Stacked spectra after the subtraction of the best fit of FeII template as the blue line. The straight line shows the peak of the emission of MgII at ∼120km/s, which is where the peak of the flux is located. The orange line shows the red hand side of the emission mirrored and over-plotting the left hand side. This allows to clearly see the asymmetry in the emission, even after the removal of the residual iron.

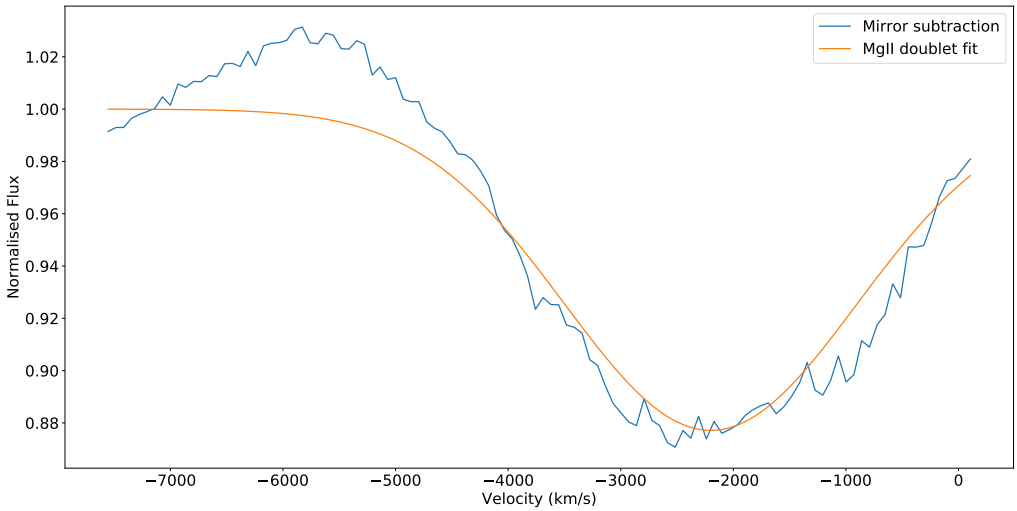

Figure 4.7: The blue line represents the flux of the stacked spectra in velocity space, using the continuum for the normalisation after subtracting the best fit of the iron template, and using the mirrored right hand side of the emission to subtract to the left side of the peak. The orange line is a gaussian fit using the two peaks of the MgII doublet, separated by 750km/s. Note that due to very large velocity width of the absorption, both lines are blended.

invert the values of the array to compare them with the right side (negative in velocity). Our final mirror subtraction shows a very strong, broad absorption feature, blueshifted from the quasar redshift at -2200km/s. The resulting flux can be seen on Fig 4.7 as the blue line. The orange line is a MgII doublet fitting (using the standard separation of 750km/s between the two lines). The fitting shows that the doublet is blended, and that there is a deep absorption, with a $\sigma = 1300$ km/s, and a peak of $\lambda 2976$ Å at -2200 km/s. The absorption feature has a total equivalent width of the MgII doublet of 4.7 Å.

4.4 Discussion

Our main result is the tentative detection of a strong, blue-shifted, broad intrinsic absorption against MgII broad emission line, or a mix of individual narrow absorption from MgII at the redshift of the QSOs.

A key element in our analysis is the modelling of the broad FeII emission. When included in the fit of the individual spectra and subtracted as part of the continuum, we found that the wings of the stacked MgII clearly contain a residual contribution which we interpret as coming from a narrower FeII complex, not accounted for in the individual (lower SNR) spectral fits. The FeII and MgII have similar ionisation potentials (7.90 eV and 7.64

eV respectively), and are likely to co-exist spatially in the electromagnetic spectrum. The difference between the asymmetries in the absorption profiles between these two species might be due to a larger amount of emission infill on top of the MgII absorption, causing the MgII λ2796,2803 Å to be blueshifted from their rest-frame by larger amounts.

Predictions of properties of emission and absorption features in a spherical model of gas outflows in galaxies show that the net effect of absorption and emission is always absorption (Zhu et al., 2015). The reason behind this is that, on the one hand, the absorption is inherently induced by the gas in front of the background light source; on the other hand, the observed emission originates from gas located everywhere except behind the galaxy (due to occultation effect of photons located behind the light source, that cannot penetrate the high-density regions at the galactic centre).

Another expected consequence from the occultation effect is that if outflows are dominant over inflows, the emission profile in velocity space is preferentially blueshifted. This is also due to the occultation of the redshifted emission side. Although this model was used for galaxies (Zhu et al., 2015), the area around AGNs could be extrapolated as a more dynamic region with similar basic characteristics. This could explain the similarity in the absorption of MgII doublet found in our stacked spectra, where the outflow velocities are one order of magnitude higher than the ones expected on galactic scales.

The physical properties of these outflows depend on their ionization states. The scenarios have different implications on how the feedback work, and simulations have demonstrated that the forces can be driven by thermal, magnetic or radiation, or a combination of these (Laha et al., 2021; Pillepich et al., 2019; Oppenheimer et al., 2020). The radiative mode of outflows is mostly detected through ionized blue-shifted absorption lines in UV and X-ray spectra, and are found on up to 65% of low redshift AGN (Reynolds and Fabian, 1995). Broad Absorption Line QSO (BALQSO) can be classified according to the absorption lines in the spectra. By exhibiting MgII absorption, the stacked spectra can be associated to low-ionization BALQSO (LoBAL), which typically show (Boroson and Meyers, 1992): 1) no or very weak OIII emission, 2) systematically weak HeI, 3) Na I D absorption, 4) the FeII continuum subtracted shows broad emissions that cannot be easily explained.

Our finding could suggest that a low-level LoBAL for MgII is common to QSOs. However, in order to confirm that this absorption feature is an outflow from the AGN, we would need to confirm with extra evidence such as these listed above, by analysing the full spectral stacks.

We also cannot exclude the possibility that this MgII feature found in the stack could correspond to multiple NALs blending from different but close enough velocities. These features could be difficult to distinguish from BAL-like absorption. On the other hand, the initial asymmetry could also be caused by multiple emission components which also have different velocities or widths. Interpreting the nature of this absorption feature presents many challenges, and there are several possibilities to continue this research that could confirm our results, which we comment on further in the next section.

4.5 Forward-looking

Current studies on detection and characterisation of both inflow and outflow of gas in the vicinity of AGN lack the spatial resolution of the inner parsec of the central engines, required to view the flows directly. To understand the impact of these outflows we need to estimate physical and dynamical parameters like outflow velocity, column density and ionization prameter, which can be derived from the spectral fitting of the absorption. This in turn will allow us to derive other quantities that cannot be measured from spectroscopy, such as mass outflow rate, momentum outflow rate, and kinetic luminosity. In some cases narrow emission lines can be spatially resolved in nearby AGN, allowing to estimate their distance and mass outflow rates (Revalski et al. 2018; Crenshaw et al. 2015). This would give us the tools and parameters needed to build physical models and measure quantitatively the amount of energy that is being expelled in this outflows.

Absorption spectroscopy shows promising results to study outflows in the region around AGNs. The large number of spectra used in this study enables to detect feature of MgII in absorption. Strong absorption lines in the UV are common in the rest-frame spectra of AGN, and the most common lines used are ions like CIV, NV, OVI, SiIV, CII, SiII and FeII. Ionization models can also give us ionization equilibrium and abundances information, using column density measurements from these and other absorption lines. This study shows that MgII can also be used to study these outflows, and opens the possibility of analysing other lines for the same use. In the future the large amount of spectroscopic data already available or up-coming from large surveys such as SDSS, 4MOST experiment (Merloni et al., 2019), and WEAVE-QSO survey (Kraljic et al., 2022) will allow to study large samples to derive statistically significant information such as this study. Simultaneous detections of UV and X-ray outflows will allow to deepen this study through the comparison of these outflows within different types of AGN, individual objects at higher spectral resolution, or also different energy ranges or wavelengths using various instruments like eROSITA (Merloni, 2012), and planned missions such as X-ray imaging and Spectroscopy mission (XRISM)(XRISM Science Team, 2022) ESA/Athena (Nandra et al., 2013), and concept studies such as Arcus, Lynx and the Large Ultraviolet Optical Infrared Surveyor (LUVOIR) (Domagal-Goldman et al., 2020).

4.6 Conclusions

In this work we made use of SDSS quasar spectra from DR18 of a highly complete X-ray selected AGN sample in the eROSITA Performance Verification eFEDS field (Brunner et al., 2022). We looked for AGN outflows by modelling in detail the intrinsic emission and absorption profile of the prominent MgII brod emission line. We stacked $\sim$ 7100 spectra aiming at detecting MgII absorption between vel [-15000:15000]km/s. We compared two different types of continuum normalisation with and without including an FeII template (Boroson and Meyers, 1992) in the individual spectral fits. We found evidence that the stacked spectra need additional modelling of a residual, which we interpret as due to narrow

FeII. To solve this, we first smoothed the template with a gaussian of different dispersions, and build a variance grid to pick the best fit to the stacked MgII wings around the areas of vel[-12000:-8000] and vel[8000:13000]km/s. We subtracted the best fit iron template from the stack, allowing for a free normalization and velocity shift.

After the removal of the residual iron signature, we mirrored the emission from the red side and subtracted from the blue side as seen in Figure 4.7. The clean average MgII broad emission is clearly asymmetric. Indeed, the final stack is consistent with a very wide absorption feature, with an equivalent width of 4.7Å and a dispersion of σ = 1300km/s and a velocity shift of -2000km/s. This signature is interpreted as MgII broad absorpion in the immediate vicinity of the accreting black holes, and due to this characteristic it can be related to outflows from AGNs.

Chapter 5

Summary and Future Perspectives

5.1 Thesis Summary

This concluding chapter aims to make a summary of the scientific results from the different projects carried out in the course of this thesis. The use of numerous quasar spectra as a background source was used throughout the different projects developed through the course of this thesis, and proves to be an essential tool in the study of the large scale structure of the universe.

The first chapter introduces the various large scale structure components and phases that were targeted in each project of this thesis, presenting an overall look of the methods and instruments used.

The second chapter is the first published paper from a project aiming to search for the Intergalactic Medium (IGM) using FeXXI λ 1354Å tracing 10^7K gas at UV wavelengths. Using more than one hundred high-spectral resolution ($R \sim 49,000$) and very high signal to noise quasar spectra from the Very Large Telescope (VLT) and the Ultraviolet Echelle Spectrograph (UVES), we stacked at the redshift of known Damped Lyman-alpha (DLA) absorbers which are tracers of intervening overdensities (galaxies). The results showed very strong absorption of FeII, SiII, OI, NiII, SiIV, CIV, AlII, AlIII, CrII Zn, MnII, MgII. We calculated a 5σ upper limit of column density log[N([FeXXI])]$<$ 17.4 (Equivalent width EW$_{rest}$ $<$ 22mÅ), three orders of magnitude higher than the expected column density of the Warm Hot Intergalactic Medium log[N([FeXXI])]$<$ 14.5.

In a second project, we used data from the Sloan Digital Sky Survey (SDSS) DR16 and X-ray massive galaxy clusters selected from ROSAT All Sky Survey (RASS) with spectroscopic redshift from the Spectroscopic Identification of eROSITA Sources (SPIDERS) program. Targeting the redshift of the clusters, we look for cold gas inside the usually hot environment of the Intra-cluster Medium, using MgII doublet as a tracer of this 10^4K cold gas. We then blindly stack 16 000 archival spectra at the redshift of the galaxy clusters. We also cross-match our sample with a MgII absorption catalogue that also uses SDSS DR16, and in this way confirm our methodology works. The MgII doublet is detected in the stack of both the MgII selected sample, and (tentively) in the blind stack of the full

16 000 QSO-cluster pair. From this, we derive a measurement of MgII absorption column density which is higher than that measured by studies of smaller haloes (groups).

For the third project we used the latest data from the SDSS DR18, with spectra covering the region of the eROSITA Final Equatorial-Depth Survey (eFEDS) fields, to study outflows in the region within a few kpc from the AGN. We search for intrinsic absorption of MgII by stacking a sample of 7000 quasar spectra, and subtracting an iron template to remove residual iron from the normalisation process. The final stack shows a very strong absorption feature at -2200km/s blueshift from the quasar, with a width of ∼1300 km/s, and an equivalent width of 4.6Å, interpreted as a MgII absorption feature that can be related to outflows from the AGN.

5.2 Future Research

This thesis has relied on the stacking technique for systematically exploiting large amounts of spectroscopic data searching for common signatures of gas of different temperatures, that can trace the large scale structure of the Universe, as well as un-resolved physical processes in the immediate vicinity of supermassive black holes. The results from these different projects show that the technique is reliable, and that it can be used to study weak signatures of gas from different energies through absorption spectroscopy.

Looking into each topic individually, simulations have shown the CGM to be multiphase, and thus can be studied in different instruments. As Anderson and Sunyaev (2018) have demonstrated by finding FeXXI at UV in emission on a filament of M87, and together with simulations that have shown that the closer to the CGM of galaxies the higher the temperature of the gas. Current missions like eROSITA (Merloni, 2012) with very high amounts of quasar spectroscopy data, and planned missions such as X-ray imaging Spectroscopy mission (XRISM)(XRISM Science Team, 2022) ESA/Athena (Nandra et al., 2013), can help achieve a multiwavelength approach with a large statistical sample.

Using WEAVE (Kraljic et al., 2022) we can also study the connection between the IGM and the CGM, by providing both kinematic and spectroscopic information about the objects. Targeting Damped Lyman-alpha absorbers through IFS have been found to be associated to multiple galaxies, widening the horizon given by single galaxy-absorber pairs. The origin of this gas could be the result of filamentary structures, or the remains of tidal interactions in a galaxy group, and could be disentangled with the help of analytical modelling.

The last project also showed that MgII could be used to study outflows in AGN, instead of other most commonly used high ionization ions. The same technique could also be applied on the same data to extend the analysis including other metals lines, or use the most common lines like CIV and check if there exists a correlation, and measure metal distribution. The sample could also be divided in different types of AGN, or it could be applied to different sets of AGN data altogether.

The common ground for the future work throughout these projects is to either increase the amount of data, and or to increase the spectral resolution of the data. In the short

term future we can already start doing so with future data from SDSS, and future surveys like 4MOST project (Merloni et al., 2019), and WEAVE-QSO survey (Kraljic et al., 2022); on longer terms with ELT/ANDES, SpecTel, MSE, Prime Focus Spectrograph (PFS) on the Subaru telescope (Tamura et al., 2016), will provide statistical analysis of the CGM that will allow for a better understanding on the formation and evolution of galaxies.

Appendix

.1 Strong Metal Lines Detections

In this section, we report on the detection of multiple strong metal lines in UVES stacked quasar spectra at the DLA redshift from Chapter 2. Figures show the normalized flux on the y-axis in velocity space. We mention the lines in the legend , together with the count of total number spectra stacked for each line.

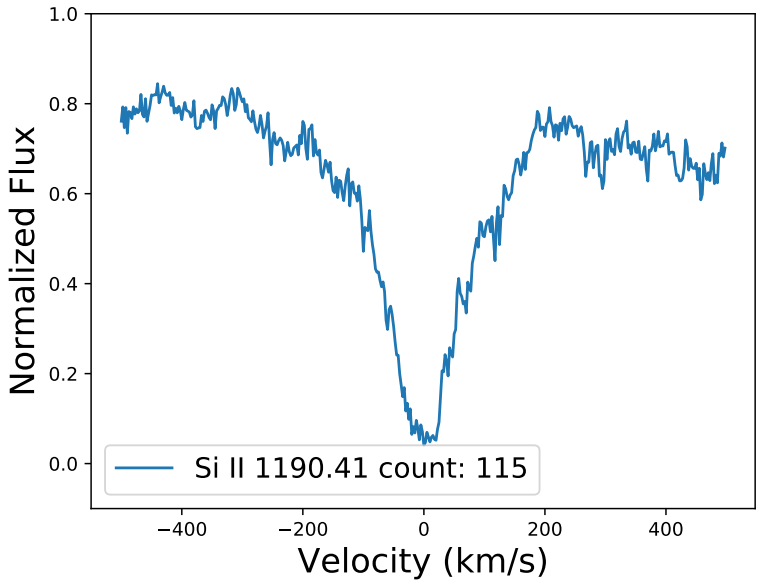
1.0
0.8
0.6
0.4
0.2
0.0
Normalized Flux
Si II 1190.41 count: 115
−400
−200
0
200
400
Velocity (km/s)

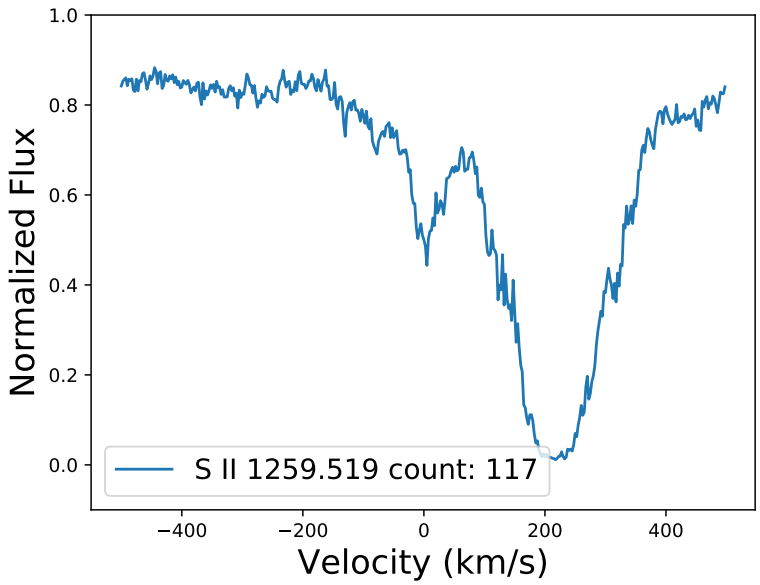
1.0
0.8
0.6
0.4
0.2
0.0
Normalized Flux
S II 1259.519 count: 117
−400
−200
0
200
400
Velocity (km/s)

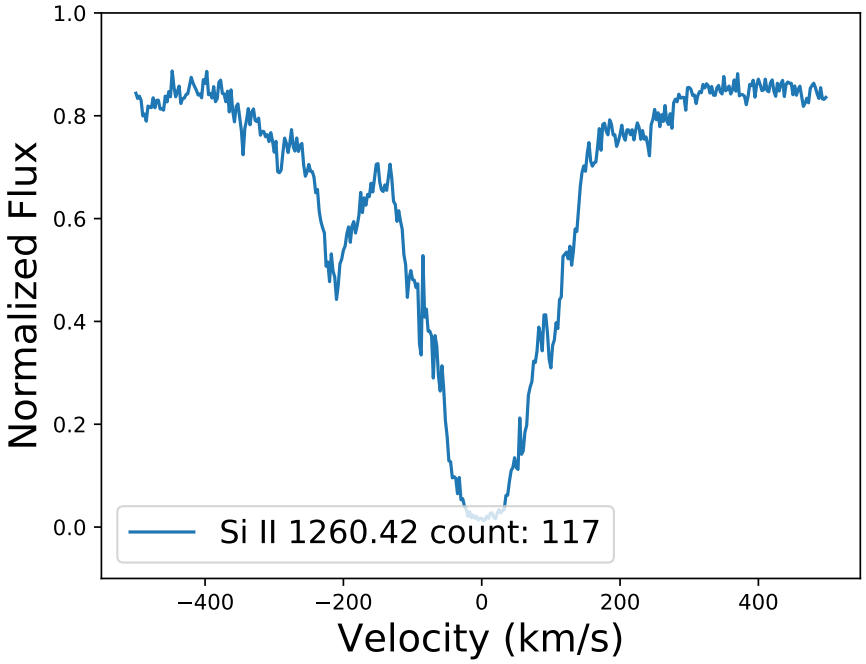
1.0
0.8
0.6
0.4
0.2
0.0
Normalized Flux
Si II 1260.42 count: 117
−400
−200
0
200
400
Velocity (km/s)

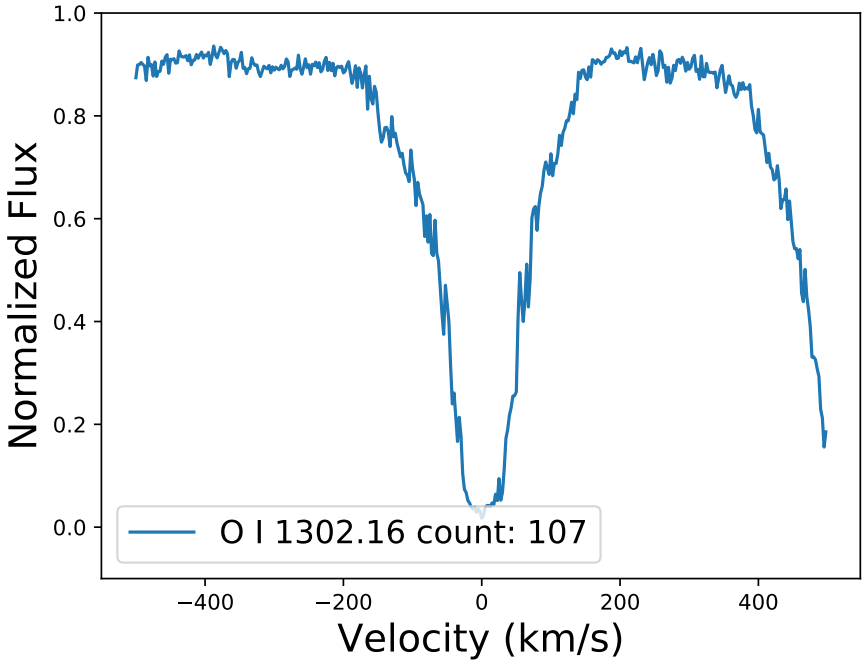
1.0
0.8
0.6
0.4
0.2
0.0
Normalized Flux
O I 1302.16 count: 107
−400
−200
0
200
400
Velocity (km/s)

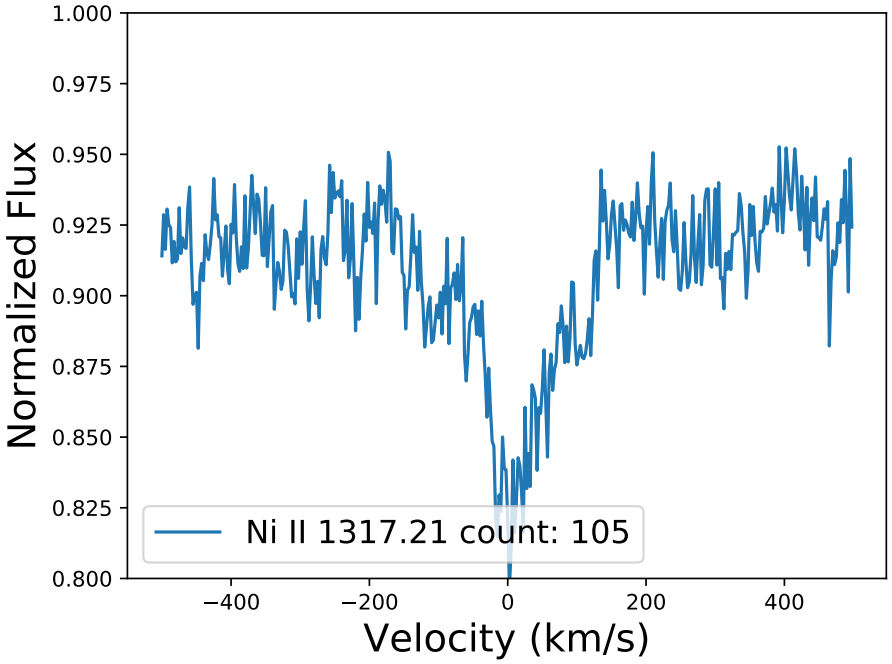
1.000
0.975
0.950
0.925
0.900
0.875
0.850
0.825
0.800
Normalized Flux
Ni II 1317.21 count: 105
−400
−200
0
200
400
Velocity (km/s)

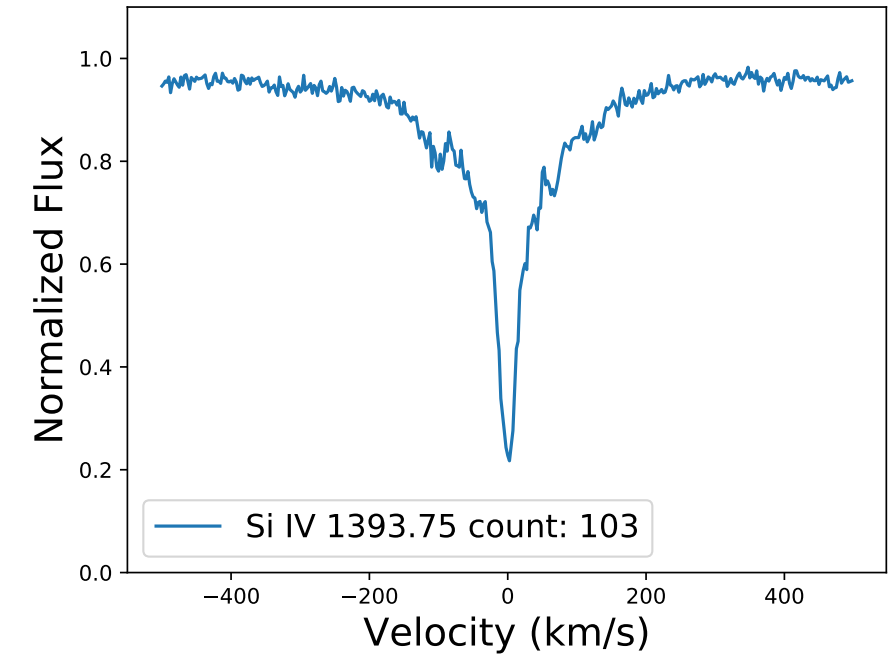
1.0
0.8
0.6
0.4
0.2
0.0
Normalized Flux
Si IV 1393.75 count: 103
−400
−200
0
200
400
Velocity (km/s)

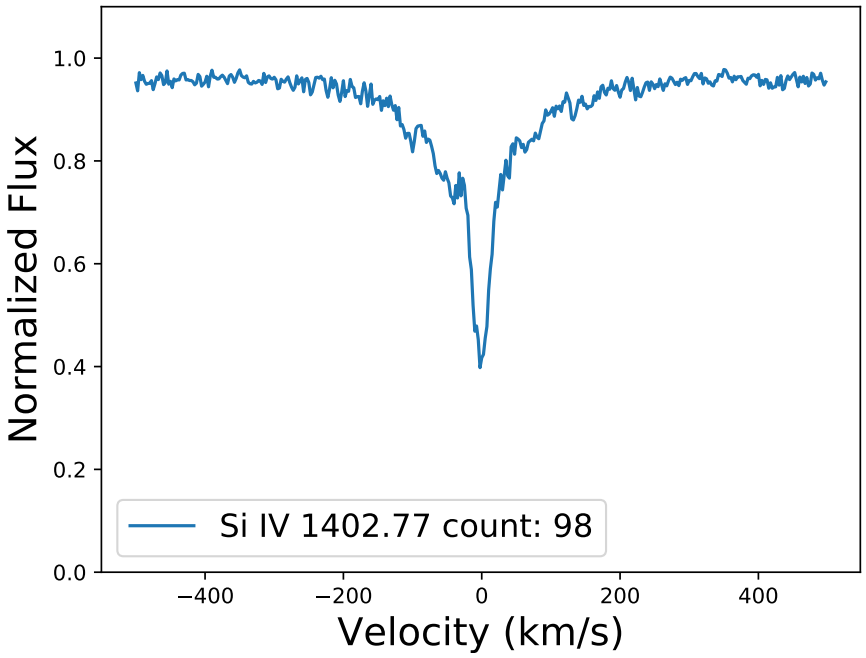
Normalized Flux
1.0
0.8
0.6
0.4
0.2
0.0
Si IV 1402.77 count: 98
−400
−200
0
200
400
Velocity (km/s)

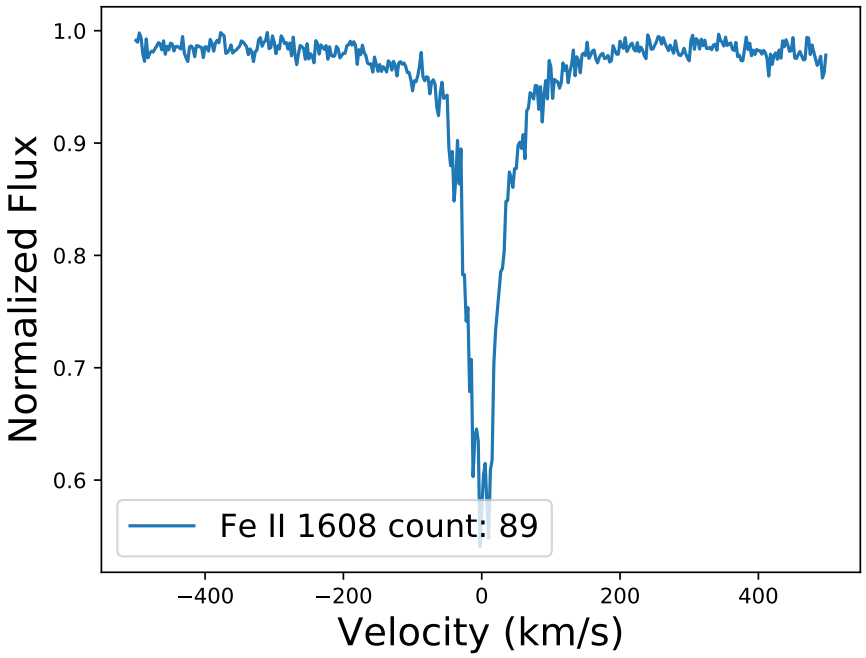
Normalized Flux
1.0
0.9
0.8
0.7
0.6
Fe II 1608 count: 89
−400
−200
0
200
400
Velocity (km/s)

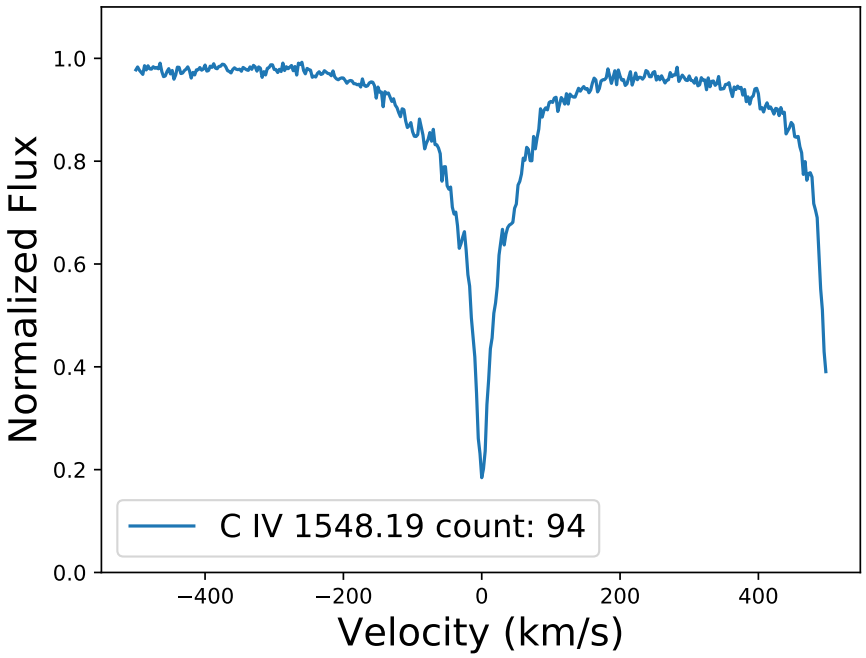
Normalized Flux
1.0
0.8
0.6
0.4
0.2
0.0
C IV 1548.19 count: 94
−400
−200
0
200
400
Velocity (km/s)

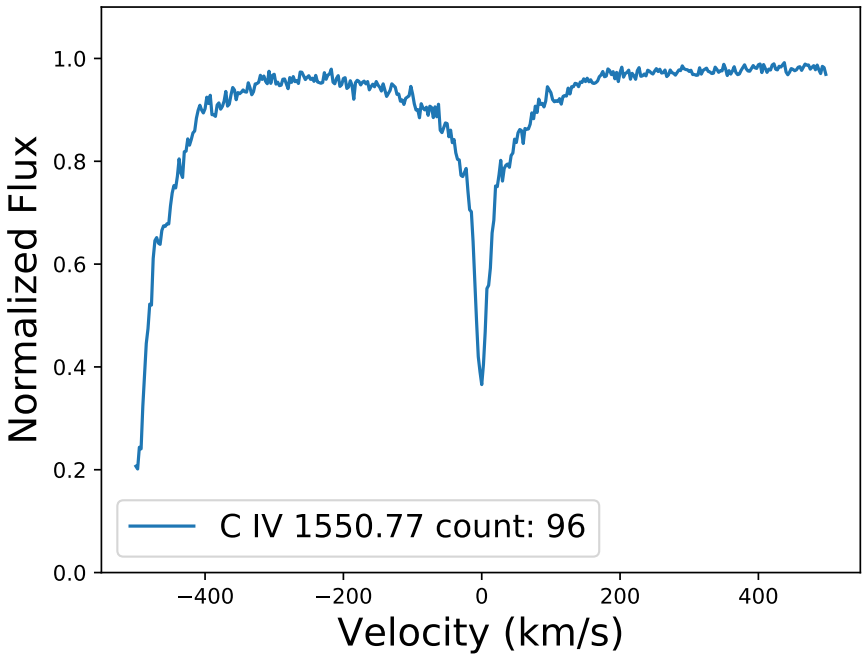
Normalized Flux
1.0
0.8
0.6
0.4
0.2
0.0
C IV 1550.77 count: 96
−400
−200
0
200
400
Velocity (km/s)

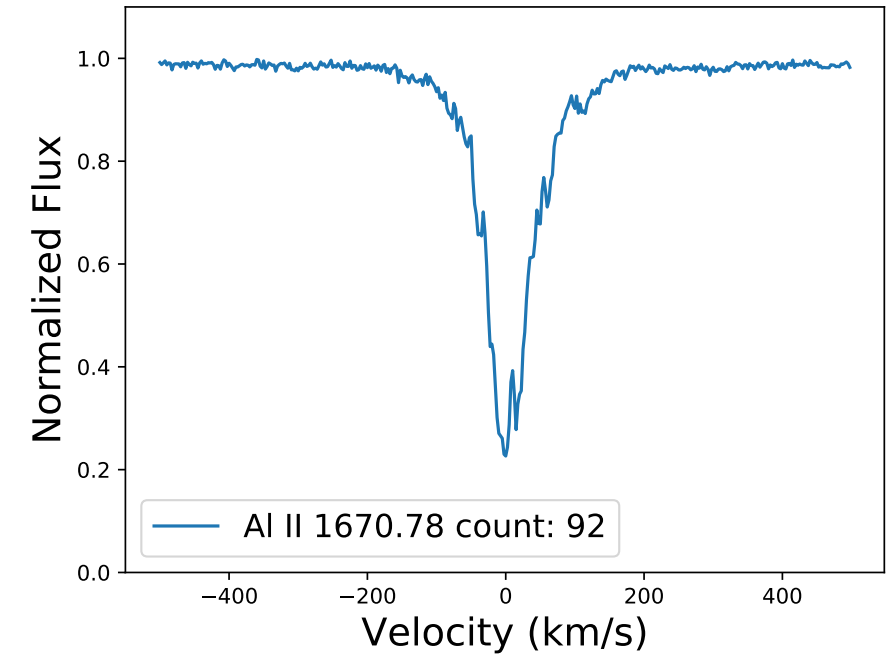
Normalized Flux
1.0
0.8
0.6
0.4
0.2
0.0
Al II 1670.78 count: 92
−400
−200
0
200
400
Velocity (km/s)

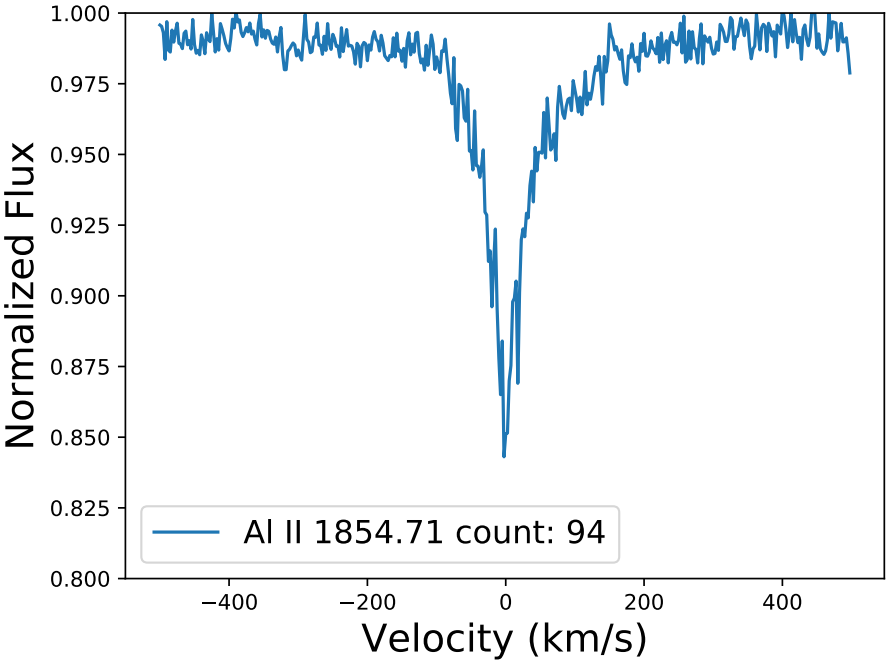
Normalized Flux
1.000
0.975
0.950
0.925
0.900
0.875
0.850
0.825
0.800
Al II 1854.71 count: 94
−400
−200
0
200
400
Velocity (km/s)

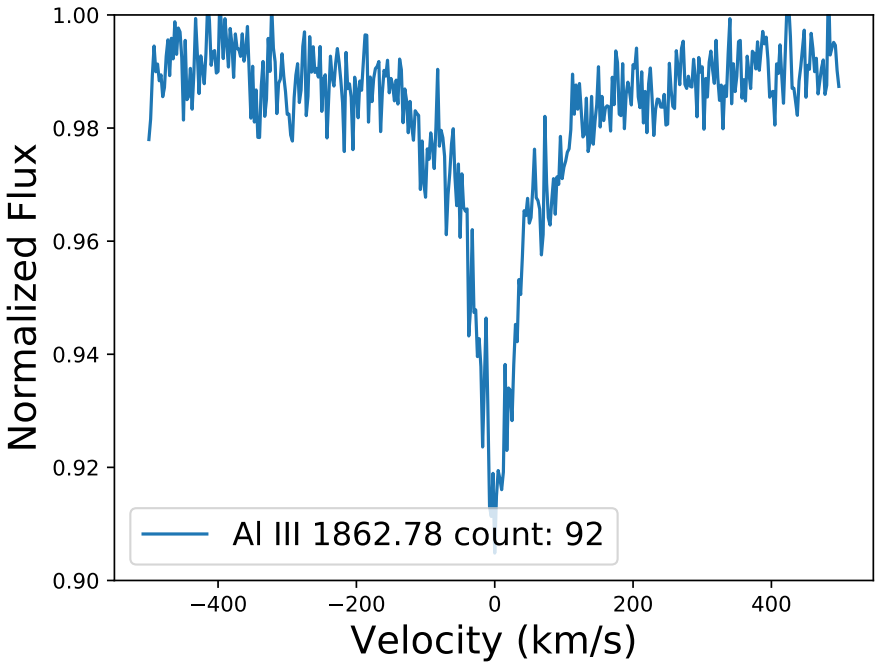
1.00
0.98
0.96
0.94
0.92
0.90
Normalized Flux
Al III 1862.78 count: 92
−400
−200
0
200
400
Velocity (km/s)

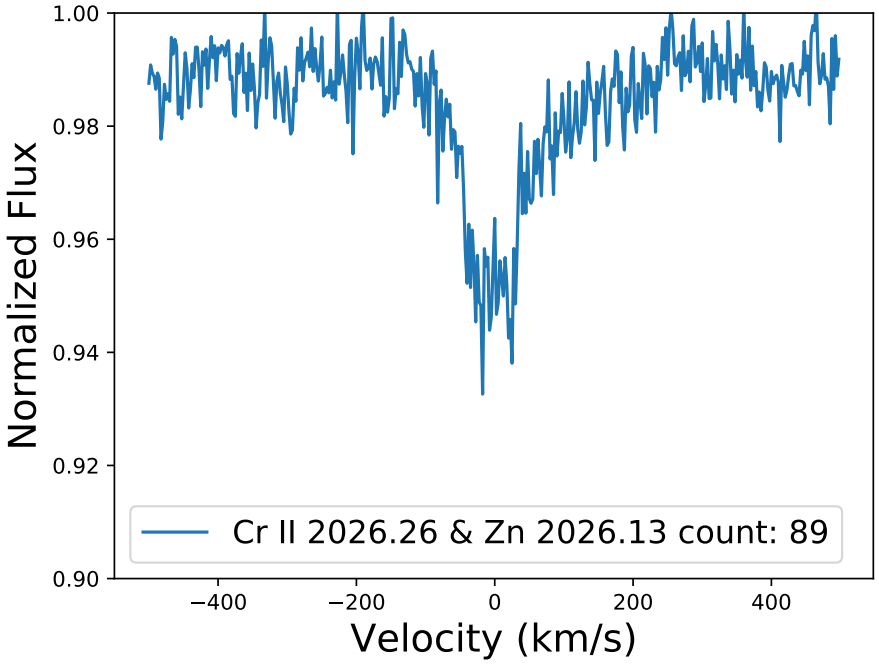
1.00
0.98
0.96
0.94
0.92
0.90
Normalized Flux
Cr II 2026.26 & Zn 2026.13 count: 89
−400
−200
0
200
400
Velocity (km/s)

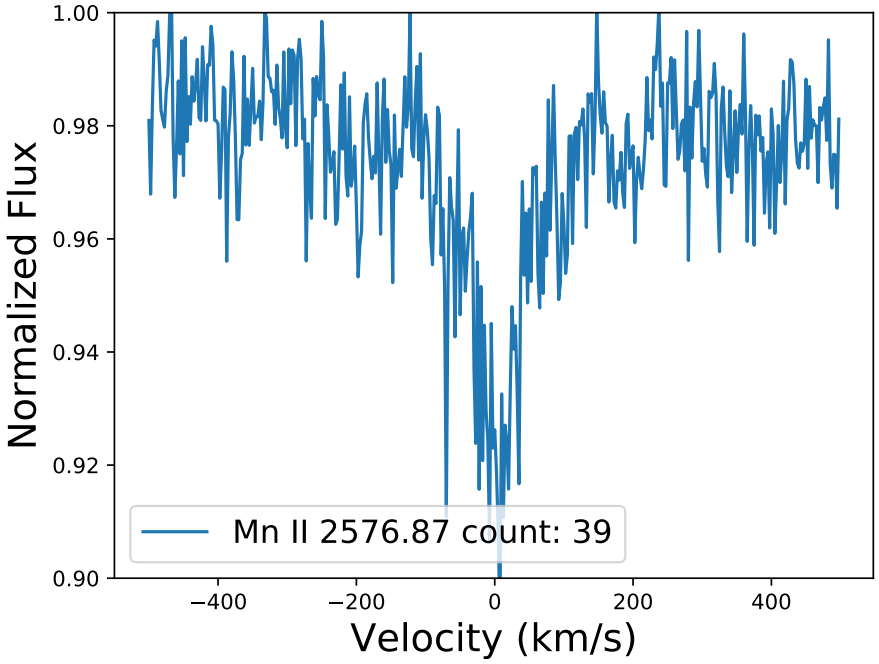
1.00
0.98
0.96
0.94
0.92
0.90
Normalized Flux
Mn II 2576.87 count: 39
−400
−200
0
200
400
Velocity (km/s)

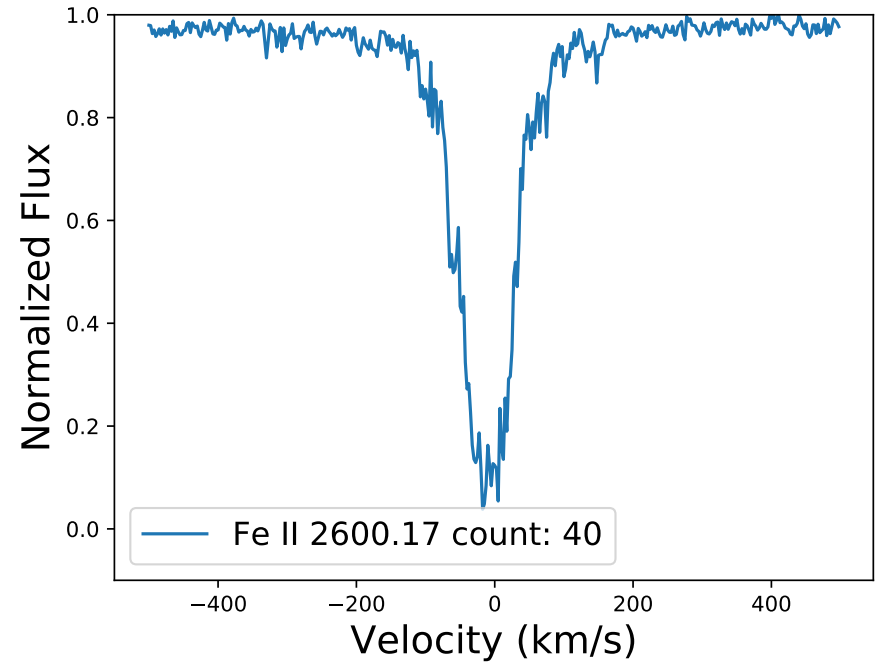
1.0
0.8
0.6
0.4
0.2
0.0
Normalized Flux
Fe II 2600.17 count: 40
−400
−200
0
200
400
Velocity (km/s)

Bibliography

Ahumada, R., Prieto, C. A., Almeida, A., Anders, F., Anderson, S. F., Andrews, B. H., Anguiano, B., Arcodia, R., Armengaud, E., Aubert, M., Avila, S., Avila-Reese, V., Badenes, C., Balland, C., Barger, K., Barrera-Ballesteros, J. K., Basu, S., Bautista, J., Beaton, R. L., Beers, T. C., Benavides, B. I. T., Bender, C. F., Bernardi, M., Bershady, M., Beutler, F., Bidin, C. M., Bird, J., Bizyaev, D., Blanc, G. A., Blanton, M. R., Boquien, M., Borissova, J., Bovy, J., Brandt, W. N., Brinkmann, J., Brownstein, J. R., Bundy, K., Bureau, M., Burgasser, A., Burtin, E., Cano-Díaz, M., Capasso, R., Cappellari, M., Carrera, R., Chabanier, S., Chaplin, W., Chapman, M., Cherinka, B., Chiappini, C., Doohyun Choi, P., Chojnowski, S. D., Chung, H., Clerc, N., Coffey, D., Comerford, J. M., Comparat, J., da Costa, L., Cousinou, M.-C., Covey, K., Crane, J. D., Cunha, K., Ilha, G. d. S., Dai, Y. S., Damsted, S. B., Darling, J., Davidson, James W., J., Davies, R., Dawson, K., De, N., de la Macorra, A., De Lee, N., Queiroz, A. B. d. A., Deconto Machado, A., de la Torre, S., Dell'Agli, F., du Mas des Bourboux, H., Diamond-Stanic, A. M., Dillon, S., Donor, J., Drory, N., Duckworth, C., Dwelly, T., Ebelke, G., Eftekharzadeh, S., Davis Eigenbrot, A., Elsworth, Y. P., Eracleous, M., Erfanianfar, G., Escoffier, S., Fan, X., Farr, E., Fernández-Trincado, J. G., Feuillet, D., Finoguenov, A., Fofie, P., Fraser-McKelvie, A., Frinchaboy, P. M., Fromenteau, S., Fu, H., Galbany, L., Garcia, R. A., García-Hernández, D. A., Oehmichen, L. A. G., Ge, J., Maia, M. A. G., Geisler, D., Gelfand, J., Goddy, J., Gonzalez-Perez, V., Grabowski, K., Green, P., Grier, C. J., Guo, H., Guy, J., Harding, P., Hasselquist, S., Hawken, A. J., Hayes, C. R., Hearty, F., Hekker, S., Hogg, D. W., Holtzman, J. A., Horta, D., Hou, J., Hsieh, B.-C., Huber, D., Hunt, J. A. S., Chitham, J. I., Imig, J., Jaber, M., Angel, C. E. J., Johnson, J. A., Jones, A. M., Jönsson, H., Jullo, E., Kim, Y., Kinemuchi, K., Kirkpatrick, Charles C., I., Kite, G. W., Klaene, M., Kneib, J.-P., Kollmeier, J. A., Kong, H., Kounkel, M., Krishnarao, D., Lacerna, I., Lan, T.-W., Lane, R. R., Law, D. R., Le Goff, J.-M., Leung, H. W., Lewis, H., Li, C., Lian, J., Lin, L., Long, D., Longa-Peña, P., Lundgren, B., Lyke, B. W., Ted Mackereth, J., MacLeod, C. L., Majewski, S. R., Manchado, A., Maraston, C., Martini, P., Masseron, T., Masters, K. L., Mathur, S., McDermid, R. M., Merloni, A., Merrifield, M., Mészáros, S., Miglio, A., Minniti, D., Minsley, R., Miyaji, T., Mohammad, F. G., Mosser, B., Mueller, E.-M., Muna, D., Muñoz-Gutiérrez, A., Myers, A. D., Nadathur, S., Nair, P., Nandra, K., do Nascimento, J. C., Nevin, R. J., Newman, J. A., Nidever, D. L., Nitschelm, C., Noterdaeme, P., O'Connell, J. E., Olmstead, M. D., Oravetz, D., Oravetz, A., Osorio, Y., Pace, Z. J., Padilla, N., Palanque-Delabrouille, N., Palicio, P. A., Pan,

H.-A., Pan, K., Parker, J., Paviot, R., Peirani, S., Ramŕez, K. P., Penny, S., Percival, W. J., Perez-Fournon, I., Pérez-Ràfols, I., Petitjean, P., Pieri, M. M., Pinsonneault, M., Poovelil, V. J., Povick, J. T., Prakash, A., Price-Whelan, A. M., Raddick, M. J., Raichoor, A., Ray, A., Rembold, S. B., Rezaie, M., Riffel, R. A., Riffel, R., Rix, H.-W., Robin, A. C., Roman-Lopes, A., Román-Zúñiga, C., Rose, B., Ross, A. J., Rossi, G., Rowlands, K., Rubin, K. H. R., Salvato, M., Sánchez, A. G., Sánchez-Menguiano, L., Sánchez-Gallego, J. R., Sayres, C., Schaefer, A., Schiavon, R. P., Schimoia, J. S., Schlafly, E., Schlegel, D., Schneider, D. P., Schultheis, M., Schwope, A., Seo, H.-J., Serenelli, A., Shafieloo, A., Shamsi, S. J., Shao, Z., Shen, S., Shetrone, M., Shirley, R., Aguirre, V. S., Simon, J. D., Skrutskie, M. F., Slosar, A., Smethurst, R., Sobeck, J., Sodi, B. C., Souto, D., Stark, D. V., Stassun, K. G., Steinmetz, M., Stello, D., Stermer, J., Storchi-Bergmann, T., Streblyanska, A., Stringfellow, G. S., Stutz, A., Suárez, G., Sun, J., Taghizadeh-Popp, M., Talbot, M. S., Tayar, J., Thakar, A. R., Theriault, R., Thomas, D., Thomas, Z. C., Tinker, J., Tojeiro, R., Toledo, H. H., Tremonti, C. A., Troup, N. W., Tuttle, S., Unda-Sanzana, E., Valentini, M., Vargas-González, J., Vargas-Magaña, M., Vázquez-Mata, J. A., Vivek, M., Wake, D., Wang, Y., Weaver, B. A., Weijmans, A.-M., Wild, V., Wilson, J. C., Wilson, R. F., Wolthuis, N., Wood-Vasey, W. M., Yan, R., Yang, M., Yèche, C., Zamora, O., Zarrouk, P., Zasowski, G., Zhang, K., Zhao, C., Zhao, G., Zheng, Z., Zheng, Z., Zhu, G., and Zou, H. (2020). The 16th Data Release of the Sloan Digital Sky Surveys: First Release from the APOGEE-2 Southern Survey and Full Release of eBOSS Spectra. *ApJS*, 249(1):3.

Aihara, H., Arimoto, N., Armstrong, R., Arnouts, S., Bahcall, N. A., Bickerton, S., Bosch, J., Bundy, K., Capak, P. L., Chan, J. H. H., Chiba, M., Coupon, J., Egami, E., Enoki, M., Finet, F., Fujimori, H., Fujimoto, S., Furusawa, H., Furusawa, J., Goto, T., Goulding, A., Greco, J. P., Greene, J. E., Gunn, J. E., Hamana, T., Harikane, Y., Hashimoto, Y., Hattori, T., Hayashi, M., Hayashi, Y., Hełminiak, K. G., Higuchi, R., Hikage, C., Ho, P. T. P., Hsieh, B.-C., Huang, K., Huang, S., Ikeda, H., Imanishi, M., Inoue, A. K., Iwasawa, K., Iwata, I., Jaelani, A. T., Jian, H.-Y., Kamata, Y., Karoji, H., Kashikawa, N., Katayama, N., Kawanomoto, S., Kayo, I., Koda, J., Koike, M., Kojima, T., Komiyama, Y., Konno, A., Koshida, S., Koyama, Y., Kusakabe, H., Leauthaud, A., Lee, C.-H., Lin, L., Lin, Y.-T., Lupton, R. H., Mandelbaum, R., Matsuoka, Y., Medezinski, E., Mineo, S., Miyama, S., Miyatake, H., Miyazaki, S., Momose, R., More, A., More, S., Moritani, Y., Moriya, T. J., Morokuma, T., Mukae, S., Murata, R., Murayama, H., Nagao, T., Nakata, F., Niida, M., Niikura, H., Nishizawa, A. J., Obuchi, Y., Oguri, M., Oishi, Y., Okabe, N., Okamoto, S., Okura, Y., Ono, Y., Onodera, M., Onoue, M., Osato, K., Ouchi, M., Price, P. A., Pyo, T.-S., Sako, M., Sawicki, M., Shibuya, T., Shimasaku, K., Shimono, A., Shirasaki, M., Silverman, J. D., Simet, M., Speagle, J., Spergel, D. N., Strauss, M. A., Sugahara, Y., Sugiyama, N., Suto, Y., Suyu, S. H., Suzuki, N., Tait, P. J., Takada, M., Takata, T., Tamura, N., Tanaka, M. M., Tanaka, M., Tanaka, M., Tanaka, Y., Terai, T., Terashima, Y., Toba, Y., Tominaga, N., Toshikawa, J., Turner, E. L., Uchida, T., Uchiyama, H., Umetsu, K., Uraguchi, F., Urata, Y., Usuda, T., Utsumi, Y., Wang, S.-Y., Wang, W.-H., Wong, K. C., Yabe, K., Yamada, Y., Yamanoi,

H., Yasuda, N., Yeh, S., Yonehara, A., and Yuma, S. (2018). The Hyper Suprime-Cam SSP Survey: Overview and survey design. *PASJ*, 70:S4.

Anand, A., Kauffmann, G., and Nelson, D. (2022). Cool circumgalactic gas in galaxy clusters: connecting the DESI legacy imaging survey and SDSS DR16 MgII absorbers. *arXiv e-prints*, page arXiv:2201.07811.

Anand, A., Nelson, D., and Kauffmann, G. (2021). Characterizing the abundance, properties, and kinematics of the cool circumgalactic medium of galaxies in absorption with SDSS DR16. *MNRAS*, 504(1):65–88.

Anderson, M. E. and Sunyaev, R. (2016). Searching for FUV line emission from 10^7 K gas in massive elliptical galaxies and galaxy clusters as a tracer of turbulent velocities. *MNRAS*, 459(3):2806–2821.

Anderson, M. E. and Sunyaev, R. (2018). FUV line emission, gas kinematics, and discovery of [Fe XXI] λ1354.1 in the sightline toward a filament in M87. *A&A*, 617:A123.

Arcodia, R., Campana, S., Salvaterra, R., and Ghisellini, G. (2018). X-ray absorption towards high-redshift sources: probing the intergalactic medium with blazars. *A&A*, 616:A170.

Asplund, M., Grevesse, N., Sauval, A. J., and Scott, P. (2009). The Chemical Composition of the Sun. *ARA&A*, 47(1):481–522.

Augustin, R., Péroux, C., Hamanowicz, A., Kulkarni, V., Rahmani, H., and Zanella, A. (2021). Clumpiness of observed and simulated cold circumgalactic gas. *MNRAS*, 505(4):6195–6205.

Augustin, R., Quiret, S., Milliard, B., Péroux, C., Vibert, D., Blaizot, J., Rasera, Y., Teyssier, R., Frank, S., Deharveng, J. M., Picouet, V., Martin, D. C., Hamden, E. T., Thatte, N., Pereira Santaella, M., Routledge, L., and Zieleniewski, S. (2019). Emission from the circumgalactic medium: from cosmological zoom-in simulations to multi-wavelength observables. *MNRAS*, 489(2):2417–2438.

Ayromlou, M., Nelson, D., Yates, R. M., Kauffmann, G., and White, S. D. M. (2019). A new method to quantify environment and model ram-pressure stripping in N-body simulations. *MNRAS*, 487(3):4313–4331.

Bahar, Y. E., Bulbul, E., Clerc, N., Ghirardini, V., Liu, A., Nandra, K., Pacaud, F., Chiu, I. N., Comparat, J., Ider-Chitham, J., Klein, M., Liu, T., Merloni, A., Migkas, K., Okabe, N., Ramos-Ceja, M. E., Reiprich, T. H., Sanders, J. S., and Schrabback, T. (2022). The eROSITA Final Equatorial-Depth Survey (eFEDS). X-ray properties and scaling relations of galaxy clusters and groups. *A&A*, 661:A7.

Bahé, Y. M., McCarthy, I. G., Balogh, M. L., and Font, A. S. (2013). Why does the environmental influence on group and cluster galaxies extend beyond the virial radius? *MNRAS*, 430(4):3017–3031.

Barret, D., Decourchelle, A., Fabian, A., Guainazzi, M., Nandra, K., Smith, R., and den Herder, J.-W. (2020). The Athena space X-ray observatory and the astrophysics of hot plasma. *Astronomische Nachrichten*, 341(2):224–235.

Baskin, A. and Laor, A. (2005). What controls the CIV line profile in active galactic nuclei? *MNRAS*, 356(3):1029–1044.

Battaglia, N., Bond, J. R., Pfrommer, C., and Sievers, J. L. (2012). On the Cluster Physics of Sunyaev-Zel'dovich and X-Ray Surveys. I. The Influence of Feedback, Non-thermal Pressure, and Cluster Shapes on Y-M Scaling Relations. *ApJ*, 758(2):74.

Bautz, L. P. and Morgan, W. W. (1970). On the Classification of the Forms of Clusters of Galaxies. *ApJ*, 162:L149.

Bergeron, J. (1980). Gas Close to the Radiative Continuum Source(s) in Active Nuclei. In Giacconi, R. and Setti, G., editors, *X-Ray Astronomy*, volume 60 of *NATO Advanced Study Institute (ASI) Series C*, page 355.

Bertone, S., Schaye, J., and Dolag, K. (2008). Numerical Simulations of the Warm-Hot Intergalactic Medium. *Space Sci. Rev.*, 134(1-4):295–310.

Bird, S., Garnett, R., and Ho, S. (2017). Statistical properties of damped Lyman-alpha systems from Sloan Digital Sky Survey DR12. *MNRAS*, 466(2):2111–2122.

Bischetti, M., Feruglio, C., D'Odorico, V., Arav, N., Bañados, E., Becker, G., Bosman, S. E. I., Carniani, S., Cristiani, S., Cupani, G., Davies, R., Eilers, A. C., Farina, E. P., Ferrara, A., Maiolino, R., Mazzucchelli, C., Mesinger, A., Meyer, R. A., Onoue, M., Piconcelli, E., Ryan-Weber, E., Schindler, J.-T., Wang, F., Yang, J., Zhu, Y., and Fiore, F. (2022). Suppression of black-hole growth by strong outflows at redshifts 5.8–6.6. *Nature*, 605(7909):244–247.

Böhringer, H. and Werner, N. (2010). X-ray spectroscopy of galaxy clusters: studying astrophysical processes in the largest celestial laboratories. *A&ARv*, 18(1-2):127–196.

Bonamente, M., Nevalainen, J., Tilton, E., Liivamägi, J., Tempel, E., Heinämäki, P., and Fang, T. (2016). A possible Chandra and Hubble Space Telescope detection of extragalactic WHIM towards PG 1116+215. *MNRAS*, 457(4):4236–4247.

Boroson, T. A. and Green, R. F. (1992). The Emission-Line Properties of Low-Redshift Quasi-stellar Objects. *ApJS*, 80:109.

Boroson, T. A. and Meyers, K. A. (1992). The Optical Properties of IR-selected and MG II Broad Absorption Line Quasars. *ApJ*, 397:442.

Bouché, N., Murphy, M. T., Péroux, C., Csabai, I., and Wild, V. (2006). New perspectives on strong z 0.5 Mg ii absorbers: are halo mass and equivalent width anticorrelated? *MNRAS*, 371(1):495–512.

Bowen, D. V. and Chelouche, D. (2011). The Mg II Cross-section of Luminous Red Galaxies. *ApJ*, 727(1):47.

Bregman, J. N. (2007). The Search for the Missing Baryons at Low Redshift. *ARA&A*, 45(1):221–259.

Brotherton, M. S., Wills, B. J., Steidel, C. C., and Sargent, W. L. W. (1994). Statistics of QSO Broad Emission-Line Profiles. II. The C IV lambda 1549, C iii] lambda 1909, and MG II lambda 2798 Lines. *ApJ*, 423:131.

Brunner, H., Liu, T., Lamer, G., Georgakakis, A., Merloni, A., Brusa, M., Bulbul, E., Dennerl, K., Friedrich, S., Liu, A., Maitra, C., Nandra, K., Ramos-Ceja, M. E., Sanders, J. S., Stewart, I. M., Boller, T., Buchner, J., Clerc, N., Comparat, J., Dwelly, T., Eckert, D., Finoguenov, A., Freyberg, M., Ghirardini, V., Gueguen, A., Haberl, F., Kreykenbohm, I., Krumpe, M., Osterhage, S., Pacaud, F., Predehl, P., Reiprich, T. H., Robrade, J., Salvato, M., Santangelo, A., Schrabback, T., Schwope, A., and Wilms, J. (2022). The eROSITA Final Equatorial Depth Survey (eFEDS). X-ray catalogue. *A&A*, 661:A1.

Butsky, I. S., Burchett, J. N., Nagai, D., Tremmel, M., Quinn, T. R., and Werk, J. K. (2019). Ultraviolet signatures of the multiphase intracluster and circumgalactic media in the ROMULUSC simulation. *MNRAS*, 490(3):4292–4306.

Cen, R. and Ostriker, J. P. (1999). Where Are the Baryons? *ApJ*, 514(1):1–6.

Chiu, I. N., Ghirardini, V., Liu, A., Grandis, S., Bulbul, E., Bahar, Y. E., Comparat, J., Bocquet, S., Clerc, N., Klein, M., Liu, T., Li, X., Miyatake, H., Mohr, J., More, S., Oguri, M., Okabe, N., Pacaud, F., Ramos-Ceja, M. E., Reiprich, T. H., Schrabback, T., and Umetsu, K. (2022). The eROSITA Final Equatorial-Depth Survey (eFEDS). X-ray observable-to-mass-and-redshift relations of galaxy clusters and groups with weak-lensing mass calibration from the Hyper Suprime-Cam Subaru Strategic Program survey. *A&A*, 661:A11.

Churchill, C. W., Mellon, R. R., Charlton, J. C., Jannuzi, B. T., Kirhakos, S., Steidel, C. C., and Schneider, D. P. (2000). Low- and High-Ionization Absorption Properties of Mg II Absorption-selected Galaxies at Intermediate Redshifts. II. Taxonomy, Kinematics, and Galaxies. *ApJ*, 543(2):577–598.

Clerc, N., Adami, C., Lieu, M., Maughan, B., Pacaud, F., Pierre, M., Sadibekova, T., Smith, G. P., Valageas, P., Altieri, B., Benoist, C., Maurogordato, S., and Willis, J. P. (2014). The XMM-LSS survey: the Class 1 cluster sample over the extended 11 deg^2 and its spatial distribution. *MNRAS*, 444(3):2723–2753.

Clerc, N., Kirkpatrick, C. C., Finoguenov, A., Capasso, R., Comparat, J., Damsted, S., Furnell, K., Kukkola, A. E., Ider Chitham, J., Merloni, A., Salvato, M., Gueguen, A., Dwelly, T., Collins, C., Saro, A., Erfanianfar, G., Schneider, D. P., Brownstein, J., Mamon, G. A., Padilla, N., Jullo, E., and Bizyaev, D. (2020). SPIDERS: overview of the X-ray galaxy cluster follow-up and the final spectroscopic data release. *MNRAS*, 497(3):3976–3992.

Clerc, N., Merloni, A., Zhang, Y. Y., Finoguenov, A., Dwelly, T., Nandra, K., Collins, C., Dawson, K., Kneib, J. P., Rozo, E., Rykoff, E., Sadibekova, T., Brownstein, J., Lin, Y. T., Ridl, J., Salvato, M., Schwope, A., Steinmetz, M., Seo, H. J., and Tinker, J. (2016). SPIDERS: the spectroscopic follow-up of X-ray selected clusters of galaxies in SDSS-IV. *MNRAS*, 463(4):4490–4515.

Cooke, R. J. and Fumagalli, M. (2018). Measurement of the primordial helium abundance from the intergalactic medium. *Nature Astronomy*, 2:957–961.

Croston, J. H., Pratt, G. W., Böhringer, H., Arnaud, M., Pointecouteau, E., Ponman, T. J., Sanderson, A. J. R., Temple, R. F., Bower, R. G., and Donahue, M. (2008). Galaxy-cluster gas-density distributions of the representative XMM-Newton cluster structure survey (REXCESS). *A&A*, 487(2):431–443.

Culliton, C., Charlton, J., Eracleous, M., Ganguly, R., and Misawa, T. (2019). Probing quasar winds using intrinsic narrow absorption lines. *MNRAS*, 488(4):4690–4731.

Danforth, C. W., Keeney, B. A., Tilton, E. M., Shull, J. M., Stocke, J. T., Stevans, M., Pieri, M. M., Savage, B. D., France, K., Syphers, D., Smith, B. D., Green, J. C., Froning, C., Penton, S. V., and Osterman, S. N. (2016). An HST/COS Survey of the Low-redshift Intergalactic Medium. I. Survey, Methodology, and Overall Results. *ApJ*, 817(2):111.

Danforth, C. W. and Shull, J. M. (2005). The Low-z Intergalactic Medium. I. O VI Baryon Census. *ApJ*, 624(2):555–560.

Danforth, C. W. and Shull, J. M. (2008). The Low-z Intergalactic Medium. III. H I and Metal Absorbers at z ¡ 0.4. *ApJ*, 679(1):194–219.

Danforth, C. W., Stocke, J. T., and Shull, J. M. (2010). Broad H I Absorbers as Metallicity-independent Tracers of the Warm-Hot Intergalactic Medium. *ApJ*, 710(1):613–633.

Davé, R., Cen, R., Ostriker, J. P., Bryan, G. L., Hernquist, L., Katz, N., Weinberg, D. H., Norman, M. L., and O'Shea, B. (2001). Baryons in the Warm-Hot Intergalactic Medium. *ApJ*, 552(2):473–483.

de Chambure, D., Lainé, R., van Katwijk, K., and Kletzkine, P. (1999). XMM's X-ray telescopes. *ESA Bulletin*, 100:30–42.

De Cia, A., Ledoux, C., Petitjean, P., and Savaglio, S. (2018). The cosmic evolution of dust-corrected metallicity in the neutral gas. *A&A*, 611:A76.

de Graaff, A., Cai, Y.-C., Heymans, C., and Peacock, J. A. (2019a). Probing the missing baryons with the Sunyaev-Zel'dovich effect from filaments. *A&A*, 624:A48.

de Graaff, A., Cai, Y.-C., Heymans, C., and Peacock, J. A. (2019b). Probing the missing baryons with the Sunyaev-Zel'dovich effect from filaments. *A&A*, 624:A48.

de Jong, R. S., Agertz, O., Berbel, A. A., Aird, J., Alexander, D. A., Amarsi, A., Anders, F., Andrae, R., Ansarinejad, B., Ansorge, W., Antilogus, P., Anwand -Heerwart, H., Arentsen, A., Arnadottir, A., Asplund, M., Auger, M., Azais, N., Baade, D., Baker, G., Baker, S., Balbinot, E., Baldry, I. K., Banerji, M., Barden, S., Barklem, P., Barthélémy-Mazot, E., Battistini, C., Bauer, S., Bell, C. P. M., Bellido-Tirado, O., Bellstedt, S., Belokurov, V., Bensby, T., Bergemann, M., Bestenlehner, J. M., Bielby, R., Bilicki, M., Blake, C., Bland-Hawthorn, J., Boeche, C., Boland, W., Boller, T., Bongard, S., Bongiorno, A., Bonifacio, P., Boudon, D., Brooks, D., Brown, M. J. I., Brown, R., Brüggen, M., Brynnel, J., Brzeski, J., Buchert, T., Buschkamp, P., Caffau, E., Caillier, P., Carrick, J., Casagrande, L., Case, S., Casey, A., Cesarini, I., Cescutti, G., Chapuis, D., Chiappini, C., Childress, M., Christlieb, N., Church, R., Cioni, M. R. L., Cluver, M., Colless, M., Collett, T., Comparat, J., Cooper, A., Couch, W., Courbin, F., Croom, S., Croton, D., Daguisé, E., Dalton, G., Davies, L. J. M., Davis, T., de Laverny, P., Deason, A., Dionies, F., Disseau, K., Doel, P., Döscher, D., Driver, S. P., Dwelly, T., Eckert, D., Edge, A., Edvardsson, B., Youssoufi, D. E., Elhaddad, A., Enke, H., Erfanianfar, G., Farrell, T., Fechner, T., Feiz, C., Feltzing, S., Ferreras, I., Feuerstein, D., Feuillet, D., Finoguenov, A., Ford, D., Fotopoulou, S., Fouesneau, M., Frenk, C., Frey, S., Gaessler, W., Geier, S., Fusillo, N. G., Gerhard, O., Giannantonio, T., Giannone, D., Gibson, B., Gillingham, P., González-Fernández, C., Gonzalez-Solares, E., Gottloeber, S., Gould, A., Grebel, E. K., Gueguen, A., Guiglion, G., Haehnelt, M., Hahn, T., Hansen, C. J., Hartman, H., Hauptner, K., Hawkins, K., Haynes, D., Haynes, R., Heiter, U., Helmi, A., Aguayo, C. H., Hewett, P., Hinton, S., Hobbs, D., Hoenig, S., Hofman, D., Hook, I., Hopgood, J., Hopkins, A., Hourihane, A., Howes, L., Howlett, C., Huet, T., Irwin, M., Iwert, O., Jablonka, P., Jahn, T., Jahnke, K., Jarno, A., Jin, S., Jofre, P., Johl, D., Jones, D., Jönsson, H., Jordan, C., Karovicova, I., Khalatyan, A., Kelz, A., Kennicutt, R., King, D., Kitaura, F., Klar, J., Klauser, U., Kneib, J. P., Koch, A., Koposov, S., Kordopatis, G., Korn, A., Kosmalski, J., Kotak, R., Kovalev, M., Kreckel, K., Kripak, Y., Krumpe, M., Kuijken, K., Kunder, A., Kushniruk, I., Lam, M. I., Lamer, G., Laurent, F., Lawrence, J., Lehmitz, M., Lemasle, B., Lewis, J., Li, B., Lidman, C., Lind, K., Liske, J., Lizon, J. L., Loveday, J., Ludwig, H. G., McDermid, R. M., Maguire, K., Mainieri, V., Mali, S., Mandel, H., Mandel, K., Mannering, L., Martell, S., Martinez Delgado, D., Matijevic, G., McGregor, H., McMahon, R., McMillan, P., Mena, O., Merloni, A., Meyer, M. J., Michel, C., Micheva, G., Migniau, J. E., Minchev, I., Monari, G., Muller, R., Murphy, D., Muthukrishna, D., Nandra, K., Navarro, R., Ness, M., Nichani, V., Nichol, R., Nicklas, H., Niederhofer, F., Norberg, P., Obreschkow, D., Oliver, S., Owers, M., Pai, N., Pankratow, S., Parkinson, D., Paschke, J., Paterson, R., Pecontal, A., Parry, I., Phillips, D., Pillepich, A., Pinard, L., Pirard, J., Piskunov, N., Plank, V., Plüschke,

D., Pons, E., Popesso, P., Power, C., Pragt, J., Pramskiy, A., Pryer, D., Quattri, M., Queiroz, A. B. d. A., Quirrenbach, A., Rahurkar, S., Raichoor, A., Ramstedt, S., Rau, A., Recio-Blanco, A., Reiss, R., Renaud, F., Revaz, Y., Rhode, P., Richard, J., Richter, A. D., Rix, H. W., Robotham, A. S. G., Roelfsema, R., Romaniello, M., Rosario, D., Rothmaier, F., Roukema, B., Ruchti, G., Rupprecht, G., Rybizki, J., Ryde, N., Saar, A., Sadler, E., Sahlén, M., Salvato, M., Sassolas, B., Saunders, W., Saviauk, A., Sbordone, L., Schmidt, T., Schnurr, O., Scholz, R. D., Schwope, A., Seifert, W., Shanks, T., Sheinis, A., Sivov, T., Skúladóttir, Á., Smartt, S., Smedley, S., Smith, G., Smith, R., Sorce, J., Spitler, L., Starkenburg, E., Steinmetz, M., Stilz, I., Storm, J., Sullivan, M., Sutherland, W., Swann, E., Tamone, A., Taylor, E. N., Teillon, J., Tempel, E., ter Horst, R., Thi, W. F., Tolstoy, E., Trager, S., Traven, G., Tremblay, P. E., Tresse, L., Valentini, M., van de Weygaert, R., van den Ancker, M., Veljanoski, J., Venkatesan, S., Wagner, L., Wagner, K., Walcher, C. J., Waller, L., Walton, N., Wang, L., Winkler, R., Wisotzki, L., Worley, C. C., Worseck, G., Xiang, M., Xu, W., Yong, D., Zhao, C., Zheng, J., Zscheyge, F., and Zucker, D. (2019). 4MOST: Project overview and information for the First Call for Proposals. *The Messenger*, 175:3–11.

Dekker, H., D'Odorico, S., Kaufer, A., Delabre, B., and Kotzlowski, H. (2000). Design, construction, and performance of UVES, the echelle spectrograph for the UT2 Kueyen Telescope at the ESO Paranal Observatory. In Iye, M. and Moorwood, A. F., editors, *Proc. SPIE*, volume 4008 of *Society of Photo-Optical Instrumentation Engineers (SPIE) Conference Series*, pages 534–545.

DeRoo, C. T., McEntaffer, R. L., Donovan, B. D., Grisé, F., Eichfeld, C., Burwitz, V., Hartner, G., Pelliciari, C., and La Caria, M.-M. (2020). Large-format X-Ray Reflection Grating Operated in an Echelle-like Mounting. *ApJ*, 897(1):92.

DESI Collaboration, Aghamousa, A., Aguilar, J., Ahlen, S., Alam, S., Allen, L. E., Allende Prieto, C., Annis, J., Bailey, S., Balland, C., Ballester, O., Baltay, C., Beaufore, L., Bebek, C., Beers, T. C., Bell, E. F., Bernal, J. L., Besuner, R., Beutler, F., Blake, C., Bleuler, H., Blomqvist, M., Blum, R., Bolton, A. S., Briceno, C., Brooks, D., Brownstein, J. R., Buckley-Geer, E., Burden, A., Burtin, E., Busca, N. G., Cahn, R. N., Cai, Y.-C., Cardiel-Sas, L., Carlberg, R. G., Carton, P.-H., Casas, R., Castander, F. J., Cervantes-Cota, J. L., Claybaugh, T. M., Close, M., Coker, C. T., Cole, S., Comparat, J., Cooper, A. P., Cousinou, M. C., Crocce, M., Cuby, J.-G., Cunningham, D. P., Davis, T. M., Dawson, K. S., de la Macorra, A., De Vicente, J., Delubac, T., Derwent, M., Dey, A., Dhungana, G., Ding, Z., Doel, P., Duan, Y. T., Ealet, A., Edelstein, J., Eftekharzadeh, S., Eisenstein, D. J., Elliott, A., Escoffier, S., Evatt, M., Fagrelius, P., Fan, X., Fanning, K., Farahi, A., Farihi, J., Favole, G., Feng, Y., Fernandez, E., Findlay, J. R., Finkbeiner, D. P., Fitzpatrick, M. J., Flaugher, B., Flender, S., Font-Ribera, A., Forero-Romero, J. E., Fosalba, P., Frenk, C. S., Fumagalli, M., Gaensicke, B. T., Gallo, G., Garcia-Bellido, J., Gaztanaga, E., Pietro Gentile Fusillo, N., Gerard, T., Gershkovich, I., Giannantonio, T., Gillet, D., Gonzalez-de-Rivera, G., Gonzalez-Perez, V., Gott, S., Graur, O., Gutierrez, G., Guy, J., Habib, S., Heetderks, H., Heetderks, I., Heitmann, K.,

Hellwing, W. A., Herrera, D. A., Ho, S., Holland, S., Honscheid, K., Huff, E., Hutchinson, T. A., Huterer, D., Hwang, H. S., Illa Laguna, J. M., Ishikawa, Y., Jacobs, D., Jeffrey, N., Jelinsky, P., Jennings, E., Jiang, L., Jimenez, J., Johnson, J., Joyce, R., Jullo, E., Juneau, S., Kama, S., Karcher, A., Karkar, S., Kehoe, R., Kennamer, N., Kent, S., Kilbinger, M., Kim, A. G., Kirkby, D., Kisner, T., Kitanidis, E., Kneib, J.-P., Koposov, S., Kovacs, E., Koyama, K., Kremin, A., Kron, R., Kronig, L., Kueter-Young, A., Lacey, C. G., Lafever, R., Lahav, O., Lambert, A., Lampton, M., Landriau, M., Lang, D., Lauer, T. R., Le Goff, J.-M., Le Guillou, L., Le Van Suu, A., Lee, J. H., Lee, S.-J., Leitner, D., Lesser, M., Levi, M. E., L'Huillier, B., Li, B., Liang, M., Lin, H., Linder, E., Loebman, S. R., Lukić, Z., Ma, J., MacCrann, N., Magneville, C., Makarem, L., Manera, M., Manser, C. J., Marshall, R., Martini, P., Massey, R., Matheson, T., McCauley, J., McDonald, P., McGreer, I. D., Meisner, A., Metcalfe, N., Miller, T. N., Miquel, R., Moustakas, J., Myers, A., Naik, M., Newman, J. A., Nichol, R. C., Nicola, A., Nicolati da Costa, L., Nie, J., Niz, G., Norberg, P., Nord, B., Norman, D., Nugent, P., O'Brien, T., Oh, M., Olsen, K. A. G., Padilla, C., Padmanabhan, H., Padmanabhan, N., Palanque-Delabrouille, N., Palmese, A., Pappalardo, D., Pâris, I., Park, C., Patej, A., Peacock, J. A., Peiris, H. V., Peng, X., Percival, W. J., Perruchot, S., Pieri, M. M., Pogge, R., Pollack, J. E., Poppett, C., Prada, F., Prakash, A., Probst, R. G., Rabinowitz, D., Raichoor, A., Ree, C. H., Refregier, A., Regal, X., Reid, B., Reil, K., Rezaie, M., Rockosi, C. M., Roe, N., Ronayette, S., Roodman, A., Ross, A. J., Ross, N. P., Rossi, G., Rozo, E., Ruhlmann-Kleider, V., Rykoff, E. S., Sabiu, C., Samushia, L., Sanchez, E., Sanchez, J., Schlegel, D. J., Schneider, M., Schubnell, M., Secroun, A., Seljak, U., Seo, H.-J., Serrano, S., Shafieloo, A., Shan, H., Sharples, R., Sholl, M. J., Shourt, W. V., Silber, J. H., Silva, D. R., Sirk, M. M., Slosar, A., Smith, A., Smoot, G. F., Som, D., Song, Y.-S., Sprayberry, D., Staten, R., Stefanik, A., Tarle, G., Sien Tie, S., Tinker, J. L., Tojeiro, R., Valdes, F., Valenzuela, O., Valluri, M., Vargas-Magana, M., Verde, L., Walker, A. R., Wang, J., Wang, Y., Weaver, B. A., Weaverdyck, C., Wechsler, R. H., Weinberg, D. H., White, M., Yang, Q., Yeche, C., Zhang, T., Zhao, G.-B., Zheng, Y., Zhou, X., Zhou, Z., Zhu, Y., Zou, H., and Zu, Y. (2016). The DESI Experiment Part I: Science,Targeting, and Survey Design. *arXiv e-prints*, page arXiv:1611.00036.

Diemer, B. (2018). COLOSSUS: A Python Toolkit for Cosmology, Large-scale Structure, and Dark Matter Halos. *ApJS*, 239(2):35.

Dolag, K., Mevius, E., and Remus, R.-S. (2017). Distribution and Evolution of Metals in the Magneticum Simulations. *Galaxies*, 5(3):35.

Dolag, K., Vazza, F., Brunetti, G., and Tormen, G. (2005). Turbulent gas motions in galaxy cluster simulations: the role of smoothed particle hydrodynamics viscosity. *MNRAS*, 364(3):753–772.

Domagal-Goldman, S. D., Bolcar, M., and Luvoir Study Team (2020). The LUVOIR Mission Concept: Design and Technology Overview. In *American Astronomical So-*

ciety Meeting Abstracts #235, volume 235 of *American Astronomical Society Meeting Abstracts*, page 171.18.

Eke, V. R., Baugh, C. M., Cole, S., Frenk, C. S., Norberg, P., Peacock, J. A., Baldry, I. K., Bland-Hawthorn, J., Bridges, T., Cannon, R., Colless, M., Collins, C., Couch, W., Dalton, G., de Propris, R., Driver, S. P., Efstathiou, G., Ellis, R. S., Glazebrook, K., Jackson, C., Lahav, O., Lewis, I., Lumsden, S., Maddox, S., Madgwick, D., Peterson, B. A., Sutherland, W., and Taylor, K. (2004). Galaxy groups in the 2dFGRS: the group-finding algorithm and the 2PIGG catalogue. *MNRAS*, 348(3):866–878.

Ellis, R. S., Bland-Hawthorn, J., Bremer, M., Brinchmann, J., Guzzo, L., Richard, J., Rix, H.-W., Tolstoy, E., and Watson, D. (2017). The Future of Multi-Object Spectroscopy: a ESO Working Group Report. *arXiv e-prints*, page arXiv:1701.01976.

Ellison, S. L., Prochaska, J. X., Hennawi, J., Lopez, S., Usher, C., Wolfe, A. M., Russell, D. M., and Benn, C. R. (2010). The nature of proximate damped Lyman α systems. *MNRAS*, 406(3):1435–1459.

Elvis, M. (2000). A Structure for Quasars. *ApJ*, 545(1):63–76.

Ettori, S. (2003). Are we missing baryons in galaxy clusters? *MNRAS*, 344(2):L13–L16.

Everett, J. E. (2005). Radiative Transfer and Acceleration in Magnetocentrifugal Winds. *ApJ*, 631(2):689–706.

Falcone, A. D., Kraft, R. P., Bautz, M. W., Gaskin, J. A., Mulqueen, J. A., and Swartz, D. A. (2018). The high definition x-ray imager (HDXI) instrument on the Lynx X-ray Surveyor. In *Proc. SPIE*, volume 10699 of *Society of Photo-Optical Instrumentation Engineers (SPIE) Conference Series*, page 1069912.

Fang, T. (2010). Detecting the Warm-Hot Intergalactic Medium in the Hercules Supercluster. NASA Proposal id.10-ADAP10-88.

Ferland, G. J., Chatzikos, M., Guzmán, F., Lykins, M. L., van Hoof, P. A. M., Williams, R. J. R., Abel, N. P., Badnell, N. R., Keenan, F. P., Porter, R. L., and Stancil, P. C. (2017). The 2017 Release Cloudy. *Rev. Mex. Astron. Astrofis.*, 53:385–438.

Finoguenov, A., Rykoff, E., Clerc, N., Costanzi, M., Hagstotz, S., Ider Chitham, J., Kiiveri, K., Kirkpatrick, C. C., Capasso, R., Comparat, J., Damsted, S., Dupke, R., Erfanianfar, G., Patrick Henry, J., Kaefer, F., Kneib, J. P., Lindholm, V., Rozo, E., van Waerbeke, L., and Weller, J. (2020). CODEX clusters. Survey, catalog, and cosmology of the X-ray luminosity function. *A&A*, 638:A114.

Flesch, E. W. (2015). The Half Million Quasars (HMQ) Catalogue. *Publ. Astron. Soc. Australia*, 32:e010.

Ford, K. E. S., McKernan, B., Sivaramakrishnan, A., Martel, A. R., Koekemoer, A., Lafrenière, D., and Parmentier, S. (2014). ACTIVE GALACTIC NUCLEUS AND QUASAR SCIENCE WITH APERTURE MASKING INTERFEROMETRY ON THEiJAMES WEBB SPACE TELESCOPE/i. *The Astrophysical Journal*, 783(2):73.

Frank, S., Mathur, S., Pieri, M., and York, D. G. (2010). A Survey of Metal Lines at High Redshift. II. SDSS Absorption Line Studies—O VI Line Density, Space Density, and Gas Metallicity at z $_{abs}$ ~3.0. *AJ*, 140(3):835–843.

Frebel, A. (2018). From Nuclei to the Cosmos: Tracing Heavy-Element Production with the Oldest Stars. *Annual Review of Nuclear and Particle Science*, 68(1):237–269.

Fresco, A. Y., Péroux, C., Merloni, A., Hamanowicz, A., and Szakacs, R. (2020). Tracing the 10^7 K warm-hot intergalactic medium with UV absorption lines. *MNRAS*, 499(4):5230–5240.

Fukugita, M. and Peebles, P. J. E. (2004). The Cosmic Energy Inventory. *ApJ*, 616(2):643–668.

Fumagalli, M. (2015). First Measurement of the Small Scale Structure of Circumgalactic Gas via Grism Spectra of Close Quasar Pairs. HST Proposal id.14127. Cycle 23.

Gad, A. F. (2021). Pygad: An intuitive genetic algorithm python library.

Galeazzi, M., Gupta, A., Huffenberger, K., and Ursino, E. (2010). Detecting The Missing Baryons With Autocorrelation Function Measurements. In *AAS/High Energy Astrophysics Division #11*, AAS/High Energy Astrophysics Division, page 6.06.

Ganguly, R. and Brotherton, M. S. (2008). On the Fraction of Quasars with Outflows. *ApJ*, 672(1):102–107.

Gaskell, C. M., Goosmann, R. W., and Klimek, E. S. (2008). Structure and kinematics of the broad-line region and torus of Active Galactic Nuclei. *Mem. Soc. Astron. Italiana*, 79:1090.

Gatuzz, E., Sanders, J. S., Canning, R., Dennerl, K., Fabian, A. C., Pinto, C., Russell, H., Tamura, T., Walker, S. A., and ZuHone, J. (2022). The velocity structure of the intracluster medium of the Centaurus cluster. *MNRAS*, 513(2):1932–1946.

Giacintucci, S., Venturi, T., Murgia, M., Dallacasa, D., Athreya, R., Bardelli, S., Mazzotta, P., and Saikia, D. J. (2007). Radio morphology and spectral analysis of cD galaxies in rich and poor galaxy clusters. *A&A*, 476(1):99–119.

Girardi, M., Biviano, A., Giuricin, G., Mardirossian, F., and Mezzetti, M. (1993). Velocity Dispersions in Galaxy Clusters. *ApJ*, 404:38.

Gonzalez, A. H., Sivanandam, S., Zabludoff, A. I., and Zaritsky, D. (2013). Galaxy Cluster Baryon Fractions Revisited. *ApJ*, 778(1):14.

Gonzalez, A. H., Zaritsky, D., and Zabludoff, A. I. (2007a). A Census of Baryons in Galaxy Clusters and Groups. *ApJ*, 666(1):147–155.

Gonzalez, A. H., Zaritsky, D., and Zabludoff, A. I. (2007b). A Census of Baryons in Galaxy Clusters and Groups. *ApJ*, 666(1):147–155.

Gunn, J. E., Siegmund, W. A., Mannery, E. J., Owen, R. E., Hull, C. L., Leger, R. F., Carey, L. N., Knapp, G. R., York, D. G., Boroski, W. N., Kent, S. M., Lupton, R. H., Rockosi, C. M., Evans, M. L., Waddell, P., Anderson, J. E., Annis, J., Barentine, J. C., Bartoszek, L. M., Bastian, S., Bracker, S. B., Brewington, H. J., Briegel, C. I., Brinkmann, J., Brown, Y. J., Carr, M. A., Czarapata, P. C., Drennan, C. C., Dombeck, T., Federwitz, G. R., Gillespie, B. A., Gonzales, C., Hansen, S. U., Harvanek, M., Hayes, J., Jordan, W., Kinney, E., Klaene, M., Kleinman, S. J., Kron, R. G., Kresinski, J., Lee, G., Limmongkol, S., Lindenmeyer, C. W., Long, D. C., Loomis, C. L., McGehee, P. M., Mantsch, P. M., Neilsen, Eric H., J., Neswold, R. M., Newman, P. R., Nitta, A., Peoples, John, J., Pier, J. R., Prieto, P. S., Prosapio, A., Rivetta, C., Schneider, D. P., Snedden, S., and Wang, S.-i. (2006). The 2.5 m Telescope of the Sloan Digital Sky Survey. *AJ*, 131(4):2332–2359.

Guo, H., Shen, Y., and Wang, S. (2018). PyQSOFit: Python code to fit the spectrum of quasars. Astrophysics Source Code Library.

Gupta, A., Mathur, S., Krongold, Y., Nicastro, F., and Galeazzi, M. (2012). A Huge Reservoir of Ionized Gas around the Milky Way: Accounting for the Missing Mass? *ApJ*, 756(1):L8.

Hamann, F. and Sabra, B. (2004). The Diverse Nature of Intrinsic Absorbers in AGNs. In Richards, G. T. and Hall, P. B., editors, *AGN Physics with the Sloan Digital Sky Survey*, volume 311 of *Astronomical Society of the Pacific Conference Series*, page 203.

Hamanowicz, A., Péroux, C., Zwaan, M. A., Rahmani, H., Pettini, M., York, D. G., Klitsch, A., Augustin, R., Krogager, J.-K., Kulkarni, V., Fresco, A. r., Biggs, A. D., Milliard, B., and Vernet, J. D. R. (2020). MUSE-ALMA haloes V: physical properties and environment of z $\leq$ 1.4 H I quasar absorbers. *MNRAS*, 492(2):2347–2368.

Hamanowicz, A., Zwaan, M. A., Péroux, C., Lagos, C. d. P., Klitsch, A., Ivison, R. J., Biggs, A. D., Szakacs, R., and Fresco, A. (2023). ALMACAL VIII: a pilot survey for untargeted extragalactic CO emission lines in deep ALMA calibration data. *MNRAS*, 519(1):34–49.

Heilmann, R. K., Bruccoleri, A. R., Burwitz, V., DeRoo, C., Garner, A., Günther, H. M., Gullikson, E. M., Hartner, G., Hertz, E., Langmeier, A., Müller, T., Rukdee, S., Schmidt,

T., Smith, R. K., and Schattenburg, M. L. (2022). X-Ray Performance of Critical-angle Transmission Grating Prototypes for the Arcus Mission. *ApJ*, 934(2):171.

Hill, J. C., Ferraro, S., Battaglia, N., Liu, J., and Spergel, D. N. (2016). Kinematic Sunyaev-Zel'dovich Effect with Projected Fields: A Novel Probe of the Baryon Distribution with Planck, WMAP, and WISE Data. *Phys. Rev. Lett.*, 117(5):051301.

Ho, L. C. (2008). Nuclear activity in nearby galaxies. *ARA&A*, 46:475–539.

Ho, S., Dedeo, S., and Spergel, D. (2009). Finding the Missing Baryons Using CMB as a Backlight. *arXiv e-prints*, page arXiv:0903.2845.

Howk, J. C., Ribaudo, J. S., Lehner, N., Prochaska, J. X., and Chen, H.-W. (2009). Strong z 0.5 o vi absorption toward pks 0405-123: Implications for ionization and metallicity of the cosmic web.

Hudson, D. S., Mittal, R., Reiprich, T. H., Nulsen, P. E. J., Andernach, H., and Sarazin, C. L. (2010). What is a cool-core cluster? a detailed analysis of the cores of the X-ray flux-limited HIFLUGCS cluster sample. *A&A*, 513:A37.

Hummels, C. B., Smith, B. D., and Silvia, D. W. (2017). Trident: A Universal Tool for Generating Synthetic Absorption Spectra from Astrophysical Simulations. *ApJ*, 847(1):59.

Ider Chitham, J., Comparat, J., Finoguenov, A., Clerc, N., Kirkpatrick, C., Damsted, S., Kukkola, A., Capasso, R., Nandra, K., Merloni, A., Bulbul, E., Rykoff, E. S., Schneider, D. P., and Brownstein, J. R. (2020). Cosmological constraints from CODEX galaxy clusters spectroscopically confirmed by SDSS-IV/SPIDERS DR16. *MNRAS*, 499(4):4768–4784.

Johnson, S. D., Mulchaey, J. S., Chen, H.-W., Wijers, N. A., Connor, T., Muzahid, S., Schaye, J., Cen, R., Carlsten, S. G., Charlton, J., Drout, M. R., Goulding, A. D., Hansen, T. T., and Walth, G. L. (2019). The Physical Origins of the Identified and Still Missing Components of the Warm-Hot Intergalactic Medium: Insights from Deep Surveys in the Field of Blazar 1ES1553+113. *ApJ*, 884(2):L31.

Jones, C. and Forman, W. (1999). Einstein Observatory Images of Clusters of Galaxies. *ApJ*, 511(1):65–83.

Kacprzak, G. G., Muzahid, S., Churchill, C. W., Nielsen, N. M., and Charlton, J. C. (2016). HST Observations Reveal the Curious Geometry of Circumgalactic Gas. In *The Interplay between Local and Global Processes in Galaxies,*, page 26.

Kaiser, N. (1986). Evolution and clustering of rich clusters. *MNRAS*, 222:323–345.

Kapferer, W., Kronberger, T., Weratschnig, J., and Schindler, S. (2007). X-ray measured metallicities of the intra-cluster medium: a good measure for the metal mass? *A&A*, 472(3):757–762.

Keeney, B. A., Danforth, C. W., Stocke, J. T., France, K., and Green, J. C. (2012). On the Significance of Absorption Features in HST/COS Data. *PASP*, 124(918):830.

Kim, J.-G. and Kim, W.-T. (2013). Instability of Evaporation Fronts in the Interstellar Medium. *ApJ*, 779(1):48.

Kirkpatrick, C. C., Clerc, N., Finoguenov, A., Damsted, S., Ider Chitham, J., Kukkola, A. E., Gueguen, A., Furnell, K., Rykoff, E., Comparat, J., Saro, A., Capasso, R., Padilla, N., Erfanianfar, G., Mamon, G. A., Collins, C., Merloni, A., Brownstein, J. R., and Schneider, D. P. (2021a). SPIDERS: an overview of the largest catalogue of spectroscopically confirmed x-ray galaxy clusters. *MNRAS*, 503(4):5763–5777.

Kirkpatrick, C. C., Clerc, N., Finoguenov, A., Damsted, S., Ider Chitham, J., Kukkola, A. E., Gueguen, A., Furnell, K., Rykoff, E., Comparat, J., Saro, A., Capasso, R., Padilla, N., Erfanianfar, G., Mamon, G. A., Collins, C., Merloni, A., Brownstein, J. R., and Schneider, D. P. (2021b). SPIDERS: an overview of the largest catalogue of spectroscopically confirmed x-ray galaxy clusters. *MNRAS*, 503(4):5763–5777.

Kirkpatrick, C. C. and McNamara, B. R. (2015). Hot outflows in galaxy clusters. *MNRAS*, 452(4):4361–4376.

Kollmeier, J. A., Zasowski, G., Rix, H.-W., Johns, M., Anderson, S. F., Drory, N., Johnson, J. A., Pogge, R. W., Bird, J. C., Blanc, G. A., Brownstein, J. R., Crane, J. D., De Lee, N. M., Klaene, M. A., Kreckel, K., MacDonald, N., Merloni, A., Ness, M. K., O'Brien, T., Sanchez-Gallego, J. R., Sayres, C. C., Shen, Y., Thakar, A. R., Tkachenko, A., Aerts, C., Blanton, M. R., Eisenstein, D. J., Holtzman, J. A., Maoz, D., Nandra, K., Rockosi, C., Weinberg, D. H., Bovy, J., Casey, A. R., Chaname, J., Clerc, N., Conroy, C., Eracleous, M., Gänsicke, B. T., Hekker, S., Horne, K., Kauffmann, J., McQuinn, K. B. W., Pellegrini, E. W., Schinnerer, E., Schlafly, E. F., Schwope, A. D., Seibert, M., Teske, J. K., and van Saders, J. L. (2017). SDSS-V: Pioneering Panoptic Spectroscopy. *arXiv e-prints*, page arXiv:1711.03234.

Komatsu, E., Smith, K. M., Dunkley, J., Bennett, C. L., Gold, B., Hinshaw, G., Jarosik, N., Larson, D., Nolta, M. R., Page, L., Spergel, D. N., Halpern, M., Hill, R. S., Kogut, A., Limon, M., Meyer, S. S., Odegard, N., Tucker, G. S., Weiland, J. L., Wollack, E., and Wright, E. L. (2011). Seven-year Wilkinson Microwave Anisotropy Probe (WMAP) Observations: Cosmological Interpretation. *ApJS*, 192(2):18.

Kovács, O. E., Bogdán, Á., Smith, R. a. K., Kraft, R. P., and Forman, W. R. (2019). Detection of the Missing Baryons toward the Sightline of H1821+643. *ApJ*, 872(1):83.

Kraljic, K., Laigle, C., Pichon, C., Peirani, S., Codis, S., Shim, J., Cadiou, C., Pogosyan, D., Arnouts, S., Pieri, M., Iršič, V., Morrison, S. S., Oñorbe, J., Pérez-Ràfols, I., and Dalton, G. (2022). Forecasts for WEAVE-QSO: 3D clustering and connectivity of critical points with Lyman-α tomography. *arXiv e-prints*, page arXiv:2201.02606.

Kravtsov, A. V. and Borgani, S. (2012). Formation of Galaxy Clusters. *ARA&A*, 50:353–409.

Kravtsov, A. V., Nagai, D., and Vikhlinin, A. A. (2005). Effects of Cooling and Star Formation on the Baryon Fractions in Clusters. *ApJ*, 625(2):588–598.

Kruczek, N. E., Richards, G. T., Gallagher, S. C., Deo, R. P., Hall, P. B., York, D. G., and Vanden Berk, D. E. (2010). Blueshifting of CIV and the Baldwin Effect in 18,000 SDSS Quasars. In *American Astronomical Society Meeting Abstracts #215*, volume 215 of *American Astronomical Society Meeting Abstracts*, page 433.04.

Kulkarni, V. P., Fall, S. M., Lauroesch, J. T., York, D. G., Welty, D. E., Khare, P., and Truran, J. W. (2005). Hubble space TelescopeObservations of element abundances in low-redshift damped ly galaxies and implications for the global metallicity-redshift relation. *The Astrophysical Journal*, 618(1):68–90.

Kunz, M. W., Jones, T. W., and Zhuravleva, I. (2022). Plasma physics of the intracluster medium. *arXiv e-prints*, page arXiv:2205.02489.

Laganá, T. F., Martinet, N., Durret, F., Lima Neto, G. B., Maughan, B., and Zhang, Y. Y. (2013). A comprehensive picture of baryons in groups and clusters of galaxies. *A&A*, 555:A66.

Laha, S., Reynolds, C. S., Reeves, J., Kriss, G., Guainazzi, M., Smith, R., Veilleux, S., and Proga, D. (2021). Ionized outflows from active galactic nuclei as the essential elements of feedback. *Nature Astronomy*, 5:13–24.

Lan, T.-W. and Mo, H. (2018). The Circumgalactic Medium of eBOSS Emission Line Galaxies: Signatures of Galactic Outflows in Gas Distribution and Kinematics. *ApJ*, 866(1):36.

Lanzetta, K. M. and Bowen, D. (1990). Intermediate-Redshift Galaxy Halos: Results from QSO Absorption Lines. *ApJ*, 357:321.

Lawrence, A. and Elvis, M. (1982). Obscuration and the various kinds of Seyfert galaxies. *ApJ*, 256:410–426.

Lee, J. C., Hwang, H. S., and Song, H. (2021). Searching for Mg II absorbers in and around galaxy clusters. *MNRAS*, 503(3):4309–4319.

Lehner, N., Savage, B. D., Richter, P., Sembach, K. R., Tripp, T. M., and Wakker, B. P. (2007). Physical Properties, Baryon Content, and Evolution of the Lyα Forest: New Insights from High-Resolution Observations at z ¡~0.4. *ApJ*, 658(2):680–709.

Li, J.-T. (2020). An X-ray view of the hot circum-galactic medium. *Astronomische Nachrichten*, 341(2):177–183.

Lim, S. H., Barnes, D., Vogelsberger, M., Mo, H. J., Nelson, D., Pillepich, A., Dolag, K., and Marinacci, F. (2021). Properties of the ionized CGM and IGM: tests for galaxy formation models from the Sunyaev-Zel'dovich effect. *MNRAS*, 504(4):5131–5143.

Lim, S. H., Mo, H. J., Wang, H., and Yang, X. (2020). Detection of Missing Baryons in Galaxy Groups with Kinetic SunyaevZel'dovich Effect. *ApJ*, 889(1):48.

Liske, J., Grazian, A., Vanzella, E., Dessauges, M., Viel, M., Pasquini, L., Haehnelt, M., Cristiani, S., Pepe, F., Avila, G., Bonifacio, P., Bouchy, F., Dekker, H., Delabre, B., D'Odorico, S., D'Odorico, V., Levshakov, S., Lovis, C., Mayor, M., Molaro, P., Moscardini, L., Murphy, M. T., Queloz, D., Shaver, P., Udry, S., Wiklind, T., and Zucker, S. (2008). Cosmic dynamics in the era of Extremely Large Telescopes. *MNRAS*, 386(3):1192–1218.

Liu, W.-J., Zhou, H., Ji, T., Yuan, W., Wang, T.-G., Jian, G., Shi, X., Zhang, S., Jiang, P., Shu, X., Wang, H., Wang, S.-F., Sun, L., Yang, C., Liu, B., and Zhao, W. (2015). A COMPREHENSIVE STUDY OF BROAD ABSORPTION LINE QUASARS. i. PREVALENCE OF he i$*ABSORPTIONLINEMULTIPLETSINLOW-IONIZATIONOBJECTS.TheAstrophysicalJournalSupplementSeries$, 217(1) : 11.

Lofthouse, E. K., Fumagalli, M., Fossati, M., O'Meara, J. M., Murphy, M. T., Christensen, L., Prochaska, J. X., Cantalupo, S., Bielby, R. M., Cooke, R. J., Lusso, E., and Morris, S. L. (2020). MUSE Analysis of Gas around Galaxies (MAGG) - I: Survey design and the environment of a near pristine gas cloud at z $\approx$ 3.5. *MNRAS*, 491(2):2057–2074.

Lopez, S., Barrientos, L. F., Lira, P., Padilla, N., Gilbank, D. G., Gladders, M. D., Maza, J., Tejos, N., Vidal, M., and Yee, H. K. C. (2008). Galaxy Clusters in the Line of Sight to Background Quasars. I. Survey Design and Incidence of Mg II Absorbers at Cluster Redshifts. *ApJ*, 679(2):1144–1161.

Lyke, B. W., Higley, A. N., McLane, J. N., Schurhammer, D. P., Myers, A. D., Ross, A. J., Dawson, K., Chabanier, S., Martini, P., Busca, N. G., Mas des Bourboux, H. d., Salvato, M., Streblyanska, A., Zarrouk, P., Burtin, E., Anderson, S. F., Bautista, J., Bizyaev, D., Brandt, W. N., Brinkmann, J., Brownstein, J. R., Comparat, J., Green, P., de la Macorra, A., Muñoz Gutiérrez, A., Hou, J., Newman, J. A., Palanque-Delabrouille, N., Pâris, I., Percival, W. J., Petitjean, P., Rich, J., Rossi, G., Schneider, D. P., Smith, A., Vivek, M., and Weaver, B. A. (2020). The Sloan Digital Sky Survey Quasar Catalog: Sixteenth Data Release. *ApJS*, 250(1):8.

Lynden-Bell, D. (1969). Galactic Nuclei as Collapsed Old Quasars. *Nature*, 223(5207):690–694.

Machado, R. E. G., Tissera, P. B., Lima Neto, G. B., and Sodré, L. (2018). Properties of the circumgalactic medium in simulations compared to observations. *A&A*, 609:A66.

Macquart, J. P., Prochaska, J. X., McQuinn, M., Bannister, K. W., Bhandari, S., Day, C. K., Deller, A. T., Ekers, R. D., James, C. W., Marnoch, L., Osłowski, S., Phillips, C., Ryder, S. D., Scott, D. R., Shannon, R. M., and Tejos, N. (2020). A census of baryons in the Universe from localized fast radio bursts. *Nature*, 581(7809):391–395.

Mantz, A. B., Allen, S. W., Morris, R. G., Schmidt, R. W., von der Linden, A., and Urban, O. (2015). Cosmology and astrophysics from relaxed galaxy clusters - I. Sample selection. *MNRAS*, 449(1):199–219.

Marconi, A., Allende Prieto, C., Amado, P. J., Amate, M., Augusto, S. R., Becerril, S., Bezawada, N., Boisse, I., Bouchy, F., Cabral, A., Chazelas, B., Cirami, R., Coretti, I., Cristiani, S., Cupani, G., de Castro Leão, I., de Medeiros, J. R., de Souza, M. A. F., Di Marcantonio, P., Di Varano, I., D'Odorico, V., Drass, H., Figueira, P., Fragoso, A. B., Fynbo, J. P. U., Genoni, M., González Hernández, J. I., Haehnelt, M., Hughes, I., Huke, P., Kjeldsen, H., Korn, A. J., Land oni, M., Liske, J., Lovis, C., Maiolino, R., Marquart, T., Martins, C. J. A. P., Mason, E., Monteiro, M. A., Morris, T., Murray, G., Niedzielski, A., Oliva, E., Origlia, L., Pallé, E., Parr-Burman, P., Parro, V. C., Pepe, F., Piskunov, N., Rasilla, J. L., Rees, P., Rebolo, R., Riva, M., Rousseau, S., Sanna, N., Santos, N. C., Shen, T. C., Sortino, F., Sosnowska, D., Sousa, S., Stempels, E., Strassmeier, K., Tenegi, F., Tozzi, A., Udry, S., Valenziano, L., Vanzi, L., Weber, M., Woche, M., Xompero, M., and Zackrisson, E. (2018). ELT-HIRES, the high resolution spectrograph for the ELT: results from the Phase A study. In *Proc. SPIE*, volume 10702 of *Society of Photo-Optical Instrumentation Engineers (SPIE) Conference Series*, page 107021Y.

Marinacci, F., Vogelsberger, M., Pakmor, R., Torrey, P., Springel, V., Hernquist, L., Nelson, D., Weinberger, R., Pillepich, A., Naiman, J., and Genel, S. (2018). First results from the IllustrisTNG simulations: radio haloes and magnetic fields. *MNRAS*, 480(4):5113–5139.

Martizzi, D., Vogelsberger, M., Artale, M. C., Haider, M., Torrey, P., Marinacci, F., Nelson, D., Pillepich, A., Weinberger, R., Hernquist, L., Naiman, J., and Springel, V. (2019). Baryons in the Cosmic Web of IllustrisTNG - I: gas in knots, filaments, sheets, and voids. *MNRAS*, 486(3):3766–3787.

Mas-Ribas, L., Miralda-Escudé, J., Pérez-Ràfols, I., Arinyo-i-Prats, A., Noterdaeme, P., Petitjean, P., Schneider, D. P., York, D. G., and Ge, J. (2017). The Mean Metal-line Absorption Spectrum of Damped Lyα Systems in BOSS. *ApJ*, 846(1):4.

Mathur, S., Nicastro, F., Gupta, A., Krongold, Y., McLaughlin, B. M., Brickhouse, N., and Pradhan, A. (2017). The O VI Mystery: Mismatch between X-Ray and UV Column Densities. *ApJ*, 851(1):L7.

Matsumoto, H., Awaki, H., Ishida, M., Furuzawa, A., Yamauchi, S., Maeda, Y., Mitsuishi, I., Haba, Y., Hayashi, T., Iizuka, R., Ishibashi, K., Itoh, M., Kunieda, H., Miyazawa, T., Mori, H., Okajima, T., Sugita, S., Tamura, K., and Tawara, Y. (2018). Inorbit

performance of the Hard X-ray Telescope (HXT) on board the Hitomi (ASTRO-H) satellite. *Journal of Astronomical Telescopes, Instruments, and Systems*, 4:011212.

McDonald, M., Veilleux, S., Rupke, D. S. N., Mushotzky, R., and Reynolds, C. (2011). Star Formation Efficiency in the Cool Cores of Galaxy Clusters. *ApJ*, 734(2):95.

McQuinn, M. (2016). The Evolution of the Intergalactic Medium. *ARA&A*, 54:313–362.

Meiksin, A. A. (2009). The physics of the intergalactic medium. *Reviews of Modern Physics*, 81(4):1405–1469.

Ménard, B. and Péroux, C. (2003). Investigating lensing by absorbers in the 2dF-quasar survey. *A&A*, 410:33–43.

Merloni, A. (2012). All-sky X-ray surveys with eROSITA: Clusters, AGN, active stars and mor. In *Science from the Next Generation Imaging and Spectroscopic Surveys*, page 43.

Merloni, A., Alexander, D. A., Banerji, M., Boller, T., Comparat, J., Dwelly, T., Fotopoulou, S., McMahon, R., Nandra, K., Salvato, M., Croom, S., Finoguenov, A., Krumpe, M., Lamer, G., Rosario, D., Schwope, A., Shanks, T., Steinmetz, M., Wisotzki, L., and Worseck, G. (2019). 4MOST Consortium Survey 6: Active Galactic Nuclei. *The Messenger*, 175:42–45.

Mernier, F., Biffi, V., Yamaguchi, H., Medvedev, P., Simionescu, A., Ettori, S., Werner, N., Kaastra, J. S., de Plaa, J., and Gu, L. (2018). Enrichment of the Hot Intracluster Medium: Observations. *Space Sci. Rev.*, 214(8):129.

Mishra, S. and Muzahid, S. (2022). Discovery of a cool, metal-rich gas reservoir in the outskirts of z ~0.5 clusters. *arXiv e-prints*, page arXiv:2201.08545.

Murphy, M. T., Kacprzak, G. G., Savorgnan, G. A. D., and Carswell, R. F. (2019). The UVES Spectral Quasar Absorption Database (SQUAD) data release 1: the first 10 million seconds. *MNRAS*, 482(3):3458–3479.

Murray, N., Chiang, J., Grossman, S. A., and Voit, G. M. (1995). Accretion Disk Winds from Active Galactic Nuclei. *ApJ*, 451:498.

Naiman, J. P., Pillepich, A., Springel, V., Ramirez-Ruiz, E., Torrey, P., Vogelsberger, M., Pakmor, R., Nelson, D., Marinacci, F., Hernquist, L., Weinberger, R., and Genel, S. (2018). First results from the IllustrisTNG simulations: a tale of two elements - chemical evolution of magnesium and europium. *MNRAS*, 477(1):1206–1224.

Nandra, K., Barret, D., Barcons, X., Fabian, A., den Herder, J.-W., Piro, L., Watson, M., Adami, C., Aird, J., Afonso, J. M., Alexander, D., Argiroffi, C., Amati, L., Arnaud, M., Atteia, J.-L., Audard, M., Badenes, C., Ballet, J., Ballo, L., Bamba, A., Bhardwaj, A., Stefano Battistelli, E., Becker, W., De Becker, M., Behar, E., Bianchi, S., Biffi, V., Bîrzan, L., Bocchino, F., Bogdanov, S., Boirin, L., Boller, T., Borgani, S., Borm, K.,

Bouché, N., Bourdin, H., Bower, R., Braito, V., Branchini, E., Branduardi-Raymont, G., Bregman, J., Brenneman, L., Brightman, M., Brüggen, M., Buchner, J., Bulbul, E., Brusa, M., Bursa, M., Caccianiga, A., Cackett, E., Campana, S., Cappelluti, N., Cappi, M., Carrera, F., Ceballos, M., Christensen, F., Chu, Y.-H., Churazov, E., Clerc, N., Corbel, S., Corral, A., Comastri, A., Costantini, E., Croston, J., Dadina, M., D'Ai, A., Decourchelle, A., Della Ceca, R., Dennerl, K., Dolag, K., Done, C., Dovciak, M., Drake, J., Eckert, D., Edge, A., Ettori, S., Ezoe, Y., Feigelson, E., Fender, R., Feruglio, C., Finoguenov, A., Fiore, F., Galeazzi, M., Gallagher, S., Gandhi, P., Gaspari, M., Gastaldello, F., Georgakakis, A., Georgantopoulos, I., Gilfanov, M., Gitti, M., Gladstone, R., Goosmann, R., Gosset, E., Grosso, N., Guedel, M., Guerrero, M., Haberl, F., Hardcastle, M., Heinz, S., Alonso Herrero, A., Hervé, A., Holmstrom, M., Iwasawa, K., Jonker, P., Kaastra, J., Kara, E., Karas, V., Kastner, J., King, A., Kosenko, D., Koutroumpa, D., Kraft, R., Kreykenbohm, I., Lallement, R., Lanzuisi, G., Lee, J., Lemoine-Goumard, M., Lobban, A., Lodato, G., Lovisari, L., Lotti, S., McCharthy, I., McNamara, B., Maggio, A., Maiolino, R., De Marco, B., de Martino, D., Mateos, S., Matt, G., Maughan, B., Mazzotta, P., Mendez, M., Merloni, A., Micela, G., Miceli, M., Mignani, R., Miller, J., Miniutti, G., Molendi, S., Montez, R., Moretti, A., Motch, C., Nazé, Y., Nevalainen, J., Nicastro, F., Nulsen, P., Ohashi, T., O'Brien, P., Osborne, J., Oskinova, L., Pacaud, F., Paerels, F., Page, M., Papadakis, I., Pareschi, G., Petre, R., Petrucci, P.-O., Piconcelli, E., Pillitteri, I., Pinto, C., de Plaa, J., Pointecouteau, E., Ponman, T., Ponti, G., Porquet, D., Pounds, K., Pratt, G., Predehl, P., Proga, D., Psaltis, D., Rafferty, D., Ramos-Ceja, M., Ranalli, P., Rasia, E., Rau, A., Rauw, G., Rea, N., Read, A., Reeves, J., Reiprich, T., Renaud, M., Reynolds, C., Risaliti, G., Rodriguez, J., Rodriguez Hidalgo, P., Roncarelli, M., Rosario, D., Rossetti, M., Rozanska, A., Rovilos, E., Salvaterra, R., Salvato, M., Di Salvo, T., Sanders, J., Sanz-Forcada, J., Schawinski, K., Schaye, J., Schwope, A., Sciortino, S., Severgnini, P., Shankar, F., Sijacki, D., Sim, S., Schmid, C., Smith, R., Steiner, A., Stelzer, B., Stewart, G., Strohmayer, T., Strüder, L., Sun, M., Takei, Y., Tatischeff, V., Tiengo, A., Tombesi, F., Trinchieri, G., Tsuru, T. G., Ud-Doula, A., Ursino, E., Valencic, L., Vanzella, E., Vaughan, S., Vignali, C., Vink, J., Vito, F., Volonteri, M., Wang, D., Webb, N., Willingale, R., Wilms, J., Wise, M., Worrall, D., Young, A., Zampieri, L., In't Zand, J., Zane, S., Zezas, A., Zhang, Y., and Zhuravleva, I. (2013). The Hot and Energetic Universe: A White Paper presenting the science theme motivating the Athena+ mission. *arXiv e-prints*, page arXiv:1306.2307.

Narayanan, A. (2007). The Physical Nature of Weak MgII Quasar Absorption Line Systems. In *American Astronomical Society Meeting Abstracts*, volume 211 of *American Astronomical Society Meeting Abstracts*, page 72.04.

Narayanan, A., Savage, B. D., Wakker, B. P., Danforth, C. W., Yao, Y., Keeney, B. A., Shull, J. M., Sembach, K. R., Froning, C. S., and Green, J. C. (2011). Cosmic origins spectrograph detection of ne viii tracing warm-hot gas toward pks 0405–123. *The Astrophysical Journal*, 730(1):15.

Nelson, D., Pillepich, A., Springel, V., Pakmor, R., Weinberger, R., Genel, S., Torrey, P.,

Vogelsberger, M., Marinacci, F., and Hernquist, L. (2019). First results from the TNG50 simulation: galactic outflows driven by supernovae and black hole feedback. *MNRAS*, 490(3):3234–3261.

Nelson, D., Pillepich, A., Springel, V., Weinberger, R., Hernquist, L., Pakmor, R., Genel, S., Torrey, P., Vogelsberger, M., Kauffmann, G., Marinacci, F., and Naiman, J. (2018). First results from the IllustrisTNG simulations: the galaxy colour bimodality. *MNRAS*, 475(1):624–647.

Nelson, D., Sharma, P., Pillepich, A., Springel, V., Pakmor, R., Weinberger, R., Vogelsberger, M., Marinacci, F., and Hernquist, L. (2020). Resolving small-scale cold circumgalactic gas in TNG50. *MNRAS*, 498(2):2391–2414.

Nestor, D. B., Turnshek, D. A., and Rao, S. M. (2005). Mg II Absorption Systems in Sloan Digital Sky Survey QSO Spectra. *ApJ*, 628(2):637–654.

Netzer, H. (2015). Revisiting the Unified Model of Active Galactic Nuclei. *ARA&A*, 53:365–408.

Nevalainen, J., Tempel, E., Ahoranta, J., Liivamägi, L. J., Bonamente, M., Tilton, E., Kaastra, J., Fang, T., Heinämäki, P., Saar, E., and Finoguenov, A. (2019). To be or not to be: the case of the hot WHIM absorption in the blazar PKS 2155-304 sight line. *A&A*, 621:A88.

Nicastro, F., Kaastra, J., Krongold, Y., Borgani, S., Branchini, E., Cen, R., Dadina, M., Danforth, C. W., Elvis, M., Fiore, F., Gupta, A., Mathur, S., Mayya, D., Paerels, F., Piro, L., Rosa-Gonzalez, D., Schaye, J., Shull, J. M., Torres-Zafra, J., Wijers, N., and Zappacosta, L. (2018). Observations of the missing baryons in the warm-hot intergalactic medium. *Nature*, 558(7710):406–409.

Noterdaeme, P., Petitjean, P., Carithers, W. C., Paris, I., Font-Ribera, A., Bailey, S., Aubourg, E., Bizyaev, D., Ebelke, G., Finley, H., Ge, J., Malanushenko, E., Malanushenko, V., Miralda-Escude, J., Myers, A. D., Oravetz, D., Pan, K., Pieri, M. M., Ross, N. P., Schneider, D. P., Simmons, A., and York, D. G. (2012). VizieR Online Data Catalog: SDSS-III DR9 DLA catalogue (Noterdaeme+, 2012). *VizieR Online Data Catalog*, pages J/A+A/547/L1.

Oppenheimer, B. D., Bogdán, Á., Crain, R. A., ZuHone, J. A., Forman, W. R., Schaye, J., Wijers, N. A., Davies, J. J., Jones, C., Kraft, R. P., and Ghirardini, V. (2020). EAGLE and Illustris-TNG Predictions for Resolved eROSITA X-Ray Observations of the Circumgalactic Medium around Normal Galaxies. *ApJ*, 893(1):L24.

Pachat, S., Narayanan, A., Muzahid, S., Khaire, V., Srianand, R., Wakker, B. P., and Savage, B. D. (2016). A pair of O VI and broad Ly α absorbers probing warm gas in a galaxy group environment at z $\sim$ 0.4. *MNRAS*, 458(1):733–746.

Parks, D., Prochaska, J. X., Dong, S., and Cai, Z. (2018). Deep learning of quasar spectra to discover and characterize damped Lyα systems. *MNRAS*, 476(1):1151–1168.

Peebles, P. J. E. (2020). *Cosmology's Century: An Inside History of our Modern Understanding of the Universe*.

Péroux, C. and Howk, J. C. (2020). The Cosmic Baryon and Metal Cycles. *ARA&A*, 58:363–406.

Peroux, C. and Howk, J. C. (2020). The Cosmic Baryon and Metal Cycles. *ARAA*, 58:363–406.

Péroux, C., Zwaan, M. A., Klitsch, A., Augustin, R., Hamanowicz, A., Rahmani, H., Pettini, M., Kulkarni, V., Straka, L. A., Biggs, A. D., York, D. G., and Milliard, B. (2019). Multiphase circumgalactic medium probed with MUSE and ALMA. *MNRAS*, 485(2):1595–1613.

Persic, M. and Salucci, P. (1992). The baryon content of the universe. *MNRAS*, 258(1):14P–18P.

Pieri, M. M., Bonoli, S., Chaves-Montero, J., Pâris, I., Fumagalli, M., Bolton, J. S., Viel, M., Noterdaeme, P., Miralda-Escudé, J., Busca, N. G., Rahmani, H., Peroux, C., Font-Ribera, A., and Trager, S. C. (2016). WEAVE-QSO: A Massive Intergalactic Medium Survey for the William Herschel Telescope. In Reylé, C., Richard, J., Cambrésy, L., Deleuil, M., Pécontal, E., Tresse, L., and Vauglin, I., editors, *SF2A-2016: Proceedings of the Annual meeting of the French Society of Astronomy and Astrophysics*, pages 259–266.

Pillepich, A., Nelson, D., Hernquist, L., Springel, V., Pakmor, R., Torrey, P., Weinberger, R., Genel, S., Naiman, J. P., Marinacci, F., and Vogelsberger, M. (2018). First results from the IllustrisTNG simulations: the stellar mass content of groups and clusters of galaxies. *MNRAS*, 475(1):648–675.

Pillepich, A., Nelson, D., Springel, V., Pakmor, R., Torrey, P., Weinberger, R., Vogelsberger, M., Marinacci, F., Genel, S., van der Wel, A., and Hernquist, L. (2019). First results from the TNG50 simulation: the evolution of stellar and gaseous discs across cosmic time. *MNRAS*, 490(3):3196–3233.

Planck Collaboration, Aghanim, N., Akrami, Y., Ashdown, M., Aumont, J., Baccigalupi, C., Ballardini, M., Banday, A. J., Barreiro, R. B., Bartolo, N., Basak, S., Battye, R., Benabed, K., Bernard, J. P., Bersanelli, M., Bielewicz, P., Bock, J. J., Bond, J. R., Borrill, J., Bouchet, F. R., Boulanger, F., Bucher, M., Burigana, C., Butler, R. C., Calabrese, E., Cardoso, J. F., Carron, J., Challinor, A., Chiang, H. C., Chluba, J., Colombo, L. P. L., Combet, C., Contreras, D., Crill, B. P., Cuttaia, F., de Bernardis, P., de Zotti, G., Delabrouille, J., Delouis, J. M., Di Valentino, E., Diego, J. M., Doré, O., Douspis, M., Ducout, A., Dupac, X., Dusini, S., Efstathiou, G., Elsner, F., Enßlin, T. A., Eriksen, H. K., Fantaye, Y., Farhang, M., Fergusson, J., Fernandez-Cobos, R.,

Finelli, F., Forastieri, F., Frailis, M., Fraisse, A. A., Franceschi, E., Frolov, A., Galeotta, S., Galli, S., Ganga, K., Génova-Santos, R. T., Gerbino, M., Ghosh, T., González-Nuevo, J., Górski, K. M., Gratton, S., Gruppuso, A., Gudmundsson, J. E., Hamann, J., Handley, W., Hansen, F. K., Herranz, D., Hildebrandt, S. R., Hivon, E., Huang, Z., Jaffe, A. H., Jones, W. C., Karakci, A., Keihänen, E., Keskitalo, R., Kiiveri, K., Kim, J., Kisner, T. S., Knox, L., Krachmalnicoff, N., Kunz, M., Kurki-Suonio, H., Lagache, G., Lamarre, J. M., Lasenby, A., Lattanzi, M., Lawrence, C. R., Le Jeune, M., Lemos, P., Lesgourgues, J., Levrier, F., Lewis, A., Liguori, M., Lilje, P. B., Lilley, M., Lindholm, V., López-Caniego, M., Lubin, P. M., Ma, Y. Z., Macías-Pérez, J. F., Maggio, G., Maino, D., Mandolesi, N., Mangilli, A., Marcos-Caballero, A., Maris, M., Martin, P. G., Martinelli, M., Martínez-González, E., Matarrese, S., Mauri, N., McEwen, J. D., Meinhold, P. R., Melchiorri, A., Mennella, A., Migliaccio, M., Millea, M., Mitra, S., Miville-Deschênes, M. A., Molinari, D., Montier, L., Morgante, G., Moss, A., Natoli, P., Nørgaard-Nielsen, H. U., Pagano, L., Paoletti, D., Partridge, B., Patanchon, G., Peiris, H. V., Perrotta, F., Pettorino, V., Piacentini, F., Polastri, L., Polenta, G., Puget, J. L., Rachen, J. P., Reinecke, M., Remazeilles, M., Renzi, A., Rocha, G., Rosset, C., Roudier, G., Rubiño-Martín, J. A., Ruiz-Granados, B., Salvati, L., Sandri, M., Savelainen, M., Scott, D., Shellard, E. P. S., Sirignano, C., Sirri, G., Spencer, L. D., Sunyaev, R., Suur-Uski, A. S., Tauber, J. A., Tavagnacco, D., Tenti, M., Toffolatti, L., Tomasi, M., Trombetti, T., Valenziano, L., Valiviita, J., Van Tent, B., Vibert, L., Vielva, P., Villa, F., Vittorio, N., Wandelt, B. D., Wehus, I. K., White, M., White, S. D. M., Zacchei, A., and Zonca, A. (2020). Planck 2018 results. VI. Cosmological parameters. *A&A*, 641:A6.

Popesso, P., Biviano, A., Finoguenov, A., Wilman, D., Salvato, M., Magnelli, B., Gruppioni, C., Pozzi, F., Rodighiero, G., Ziparo, F., Berta, S., Elbaz, D., Dickinson, M., Lutz, D., Altieri, B., Aussel, H., Cimatti, A., Fadda, D., Ilbert, O., Le Floch, E., Nordon, R., Poglitsch, A., and Xu, C. K. (2015). The evolution of galaxy star formation activity in massive haloes. *A&A*, 574:A105.

Popović, L. Č., Kovačević-Dojčinović, J., and Marčeta-Mandić, S. (2019). The structure of the Mg II broad line emitting region in Type 1 AGNs. *MNRAS*, 484(3):3180–3197.

Poudel, S., Kulkarni, V. P., Cashman, F. H., Frye, B., Péroux, C., Rahmani, H., and Quiret, S. (2020). Metal-enriched galaxies in the first ∼1 billion years: evidence of a smooth metallicity evolution at z ∼ 5. *MNRAS*, 491(1):1008–1025.

Predehl, P., Andritschke, R., Arefiev, V., Babyshkin, V., Batanov, O., Becker, W., Böhringer, H., Bogomolov, A., Boller, T., Borm, K., Bornemann, W., Bräuninger, H., Brüggen, M., Brunner, H., Brusa, M., Bulbul, E., Buntov, M., Burwitz, V., Burkert, W., Clerc, N., Churazov, E., Coutinho, D., Dauser, T., Dennerl, K., Doroshenko, V., Eder, J., Emberger, V., Eraerds, T., Finoguenov, A., Freyberg, M., Friedrich, P., Friedrich, S., Fürmetz, M., Georgakakis, A., Gilfanov, M., Granato, S., Grossberger, C., Gueguen, A., Gureev, P., Haberl, F., Hälker, O., Hartner, G., Hasinger, G., Huber, H., Ji, L., Kienlin, A. v., Kink, W., Korotkov, F., Kreykenbohm, I., Lamer, G., Lomakin, I., Lapshov, I.,

Liu, T., Maitra, C., Meidinger, N., Menz, B., Merloni, A., Mernik, T., Mican, B., Mohr, J., Müller, S., Nandra, K., Nazarov, V., Pacaud, F., Pavlinsky, M., Perinati, E., Pfeffermann, E., Pietschner, D., Ramos-Ceja, M. E., Rau, A., Reiffers, J., Reiprich, T. H., Robrade, J., Salvato, M., Sanders, J., Santangelo, A., Sasaki, M., Scheuerle, H., Schmid, C., Schmitt, J., Schwope, A., Shirshakov, A., Steinmetz, M., Stewart, I., Strüder, L., Sunyaev, R., Tenzer, C., Tiedemann, L., Trümper, J., Voron, V., Weber, P., Wilms, J., and Yaroshenko, V. (2021). The eROSITA X-ray telescope on SRG. *A&A*, 647:A1.

Prochaska, J. X., Gawiser, E., Wolfe, A. M., Castro, S., and Djorgovski, S. G. (2003). The Age-Metallicity Relation of the Universe in Neutral Gas: The First 100 Damped Lyα Systems. *ApJ*, 595(1):L9–L12.

Prochaska, J. X., Werk, J. K., Worseck, G., Tripp, T. M., Tumlinson, J., Burchett, J. N., Fox, A. J., Fumagalli, M., Lehner, N., Peeples, M. S., and Tejos, N. (2017). The COS-Halos Survey: Metallicities in the Low-redshift Circumgalactic Medium. *ApJ*, 837(2):169.

Proga, D. and Kallman, T. R. (2004). Dynamics of Line-driven Disk Winds in Active Galactic Nuclei. II. Effects of Disk Radiation. *ApJ*, 616(2):688–695.

Putman, M. E., Peek, J. E. G., and Joung, M. R. (2012). Gaseous Galaxy Halos. *ARA&A*, 50:491–529.

Qiang, D.-C. and Wei, H. (2020). Reconstructing the fraction of baryons in the intergalactic medium with fast radio bursts via Gaussian processes. *J. Cosmology Astropart. Phys.*, 2020(4):023.

Quirrenbach, A. and 4MOST Consortium (2015). 4MOST - 4-meter Multi-Object Spectroscopic Telescope. In *IAU General Assembly*, volume 29, page 2258057.

Rafelski, M., Wolfe, A. M., Prochaska, J. X., Neeleman, M., and Mendez, A. J. (2012). Metallicity Evolution of Damped Lyα Systems Out to z ~5. *ApJ*, 755(2):89.

Rahmati, A., Pawlik, A. H., Raičević, M., and Schaye, J. (2013). On the evolution of the H I column density distribution in cosmological simulations. *MNRAS*, 430(3):2427–2445.

Rankine, A. L., Matthews, J. H., Hewett, P. C., Banerji, M., Morabito, L. K., and Richards, G. T. (2021). Placing LOFAR-detected quasars in C IV emission space: implications for winds, jets and star formation. *MNRAS*, 502(3):4154–4169.

Rees, M. J. and Mészáros, P. (1998). Refreshed Shocks and Afterglow Longevity in Gamma-Ray Bursts. *ApJ*, 496(1):L1–L4.

Reiprich, T. H., Basu, K., Ettori, S., Israel, H., Lovisari, L., Molendi, S., Pointecouteau, E., and Roncarelli, M. (2013). Outskirts of Galaxy Clusters. *Space Sci. Rev.*, 177(1-4):195–245.

Reiprich, T. H., Veronica, A., Pacaud, F., Ramos-Ceja, M. E., Ota, N., Sanders, J., Kara, M., Erben, T., Klein, M., Erler, J., Kerp, J., Hoang, D. N., Brüggen, M., Marvil, J., Rudnick, L., Biffi, V., Dolag, K., Aschersleben, J., Basu, K., Brunner, H., Bulbul, E., Dennerl, K., Eckert, D., Freyberg, M., Gatuzz, E., Ghirardini, V., Käfer, F., Merloni, A., Migkas, K., Nandra, K., Predehl, P., Robrade, J., Salvato, M., Whelan, B., Diaz-Ocampo, A., Hernandez-Lang, D., Zenteno, A., Brown, M. J. I., Collier, J. D., Diego, J. M., Hopkins, A. M., Kapinska, A., Koribalski, B., Mroczkowski, T., Norris, R. P., O'Brien, A., and Vardoulaki, E. (2021). The Abell 3391/95 galaxy cluster system. A 15 Mpc intergalactic medium emission filament, a warm gas bridge, infalling matter clumps, and (re-) accelerated plasma discovered by combining SRG/eROSITA data with ASKAP/EMU and DECam data. *A&A*, 647:A2.

Reynolds, C. S. and Fabian, A. C. (1995). Warm absorbers in active galactic nuclei. *MNRAS*, 273(4):1167–1176.

Richards, G. T., Kruczek, N. E., Gallagher, S. C., Hall, P. B., Hewett, P. C., Leighly, K. M., Deo, R. P., Kratzer, R. M., and Shen, Y. (2011). Unification of Luminous Type 1 Quasars through C IV Emission. *AJ*, 141(5):167.

Rivera, A. B., Richards, G. T., Hewett, P. C., and Rankine, A. L. (2020). Characterizing Quasar C IV Emission-line Measurements from Time-resolved Spectroscopy. *ApJ*, 899(2):96.

Romaniello, M., Zampieri, S., Delmotte, N., Forchì, V., Hainaut, O., Micol, A., Retzlaff, J., Vera, I., Fourniol, N., Khan, M. A., Lange, U., Sisodia, D., Stellert, M., Stoehr, F., Arnaboldi, M., Spiniello, C., Mascetti, L., and Sterzik, M. F. (2018). Enhanced Data Discovery Services for the ESO Science Archive. *The Messenger*, 172:2–7.

Rosati, P., Borgani, S., and Norman, C. (2002). The Evolution of X-ray Clusters of Galaxies. *ARA&A*, 40:539–577.

Rowan-Robinson, M. (1977). On the unity of activity in galaxies. *ApJ*, 213:635–647.

Rykoff, E. S., Rozo, E., Hollowood, D., Bermeo-Hernandez, A., Jeltema, T., Mayers, J., Romer, A. K., Rooney, P., Saro, A., Cervantes, C. V., Wechsler, R. H., Wilcox, H., Abbott, T. M. C., Abdalla, F. B., Allam, S., Annis, J., Benoit-Lé vy, A., Bernstein, G. M., Bertin, E., Brooks, D., Burke, D. L., Capozzi, D., Rosell, A. C., Kind, M. C., Castander, F. J., Childress, M., Collins, C. A., Cunha, C. E., D'Andrea, C. B., da Costa, L. N., Davis, T. M., Desai, S., Diehl, H. T., Dietrich, J. P., Doel, P., Evrard, A. E., Finley, D. A., Flaugher, B., Fosalba, P., Frieman, J., Glazebrook, K., Goldstein, D. A., Gruen, D., Gruendl, R. A., Gutierrez, G., Hilton, M., Honscheid, K., Hoyle, B., James, D. J., Kay, S. T., Kuehn, K., Kuropatkin, N., Lahav, O., Lewis, G. F., Lidman, C., Lima, M., Maia, M. A. G., Mann, R. G., Marshall, J. L., Martini, P., Melchior, P., Miller, C. J., Miquel, R., Mohr, J. J., Nichol, R. C., Nord, B., Ogando, R., Plazas, A. A., Reil, K., Sahlén, M., Sanchez, E., Santiago, B., Scarpine, V., Schubnell, M., Sevilla-Noarbe, I.,

Smith, R. C., Soares-Santos, M., Sobreira, F., Stott, J. P., Suchyta, E., Swanson, M. E. C., Tarle, G., Thomas, D., Tucker, D., Uddin, S., Viana, P. T. P., Vikram, V., Walker, A. R., and and, Y. Z. (2016). THE REDMAPPER GALAXY CLUSTER CATALOG FROM DES SCIENCE VERIFICATION DATA. *The Astrophysical Journal Supplement Series*, 224(1):1.

Ryu, D., Kang, H., Hallman, E., and Jones, T. W. (2003). Cosmological Shock Waves and Their Role in the Large-Scale Structure of the Universe. *ApJ*, 593(2):599–610.

Salucci, P. and Persic, M. (1999). The baryonic mass function of spiral galaxies: clues to galaxy formation. *MNRAS*, 309(4):923–928.

Sanderson, A. J. R., O'Sullivan, E., Ponman, T. J., Gonzalez, A. H., Sivanandam, S., Zabludoff, A. I., and Zaritsky, D. (2013). The baryon budget on the galaxy group/cluster boundary. *MNRAS*, 429(4):3288–3304.

Sarazin, C. L. (1986). X-ray emission from clusters of galaxies. *Reviews of Modern Physics*, 58(1):1–115.

Savage, B. D., Kim, T. S., Wakker, B. P., Keeney, B., Shull, J. M., Stocke, J. T., and Green, J. C. (2014). The Properties of Low Redshift Intergalactic O VI Absorbers Determined from High S/N Observations of 14 QSOs with the Cosmic Origins Spectrograph. *ApJS*, 212(1):8.

Schaye, J., Aguirre, A., Kim, T.-S., Theuns, T., Rauch, M., and Sargent, W. L. W. (2003). Metallicity of the Intergalactic Medium Using Pixel Statistics. II. The Distribution of Metals as Traced by C IV. *ApJ*, 596(2):768–796.

Schaye, J., Crain, R. A., Bower, R. G., Furlong, M., Schaller, M., Theuns, T., Dalla Vecchia, C., Frenk, C. S., McCarthy, I. G., Helly, J. C., Jenkins, A., Rosas-Guevara, Y. M., White, S. D. M., Baes, M., Booth, C. M., Camps, P., Navarro, J. F., Qu, Y., Rahmati, A., Sawala, T., Thomas, P. A., and Trayford, J. (2015). The EAGLE project: simulating the evolution and assembly of galaxies and their environments. *MNRAS*, 446(1):521–554.

Seyffert, E. N., Cooksey, K. L., Simcoe, R. A., O'Meara, J. M., Kao, M. M., and Prochaska, J. X. (2013). Precious Metals in SDSS Quasar Spectra. II. Tracking the Evolution of Strong, 0.4 ¡ z ¡ 2.3 Mg II Absorbers with Thousands of Systems. *ApJ*, 779(2):161.

Shull, J. M., Smith, B. D., and Danforth, C. W. (2012). The Baryon Census in a Multiphase Intergalactic Medium: 30% of the Baryons May Still be Missing. *ApJ*, 759(1):23.

Shull, J. M. and van Steenberg, M. (1982). The ionization equilibrium of astrophysically abundant elements. *ApJS*, 48:95–107.

Simionescu, A., Werner, N., Böhringer, H., Kaastra, J. S., Finoguenov, A., Brüggen, M., and Nulsen, P. E. J. (2009). Chemical enrichment in the cluster of galaxies Hydra A. *A&A*, 493(2):409–424.

Simionescu, A., ZuHone, J., Zhuravleva, I., Churazov, E., Gaspari, M., Nagai, D., Werner, N., Roediger, E., Canning, R., Eckert, D., Gu, L., and Paerels, F. (2019). Constraining Gas Motions in the Intra-Cluster Medium. *Space Sci. Rev.*, 215(2):24.

Smee, S. A., Gunn, J. E., Uomoto, A., Roe, N., Schlegel, D., Rockosi, C. M., Carr, M. A., Leger, F., Dawson, K. S., Olmstead, M. D., Brinkmann, J., Owen, R., Barkhouser, R. H., Honscheid, K., Harding, P., Long, D., Lupton, R. H., Loomis, C., Anderson, L., Annis, J., Bernardi, M., Bhardwaj, V., Bizyaev, D., Bolton, A. S., Brewington, H., Briggs, J. W., Burles, S., Burns, J. G., Castander, F. J., Connolly, A., Davenport, J. R. A., Ebelke, G., Epps, H., Feldman, P. D., Friedman, S. D., Frieman, J., Heckman, T., Hull, C. L., Knapp, G. R., Lawrence, D. M., Loveday, J., Mannery, E. J., Malanushenko, E., Malanushenko, V., Merrelli, A. J., Muna, D., Newman, P. R., Nichol, R. C., Oravetz, D., Pan, K., Pope, A. C., Ricketts, P. G., Shelden, A., Sandford, D., Siegmund, W., Simmons, A., Smith, D. S., Snedden, S., Schneider, D. P., SubbaRao, M., Tremonti, C., Waddell, P., and York, D. G. (2013). The Multi-object, Fiber-fed Spectrographs for the Sloan Digital Sky Survey and the Baryon Oscillation Spectroscopic Survey. *AJ*, 146(2):32.

Springel, V., Pakmor, R., Pillepich, A., Weinberger, R., Nelson, D., Hernquist, L., Vogelsberger, M., Genel, S., Torrey, P., Marinacci, F., and Naiman, J. (2018). First results from the IllustrisTNG simulations: matter and galaxy clustering. *MNRAS*, 475(1):676–698.

Springel, V., White, S. D. M., Jenkins, A., Frenk, C. S., Yoshida, N., Gao, L., Navarro, J., Thacker, R., Croton, D., Helly, J., Peacock, J. A., Cole, S., Thomas, P., Couchman, H., Evrard, A., Colberg, J., and Pearce, F. (2005). Simulations of the formation, evolution and clustering of galaxies and quasars. *Nature*, 435(7042):629–636.

Szakacs, R., Péroux, C., Zwaan, M., Hamanowicz, A., Klitsch, A., Fresco, A. Y., Augustin, R., Biggs, A., Kulkarni, V., and Rahmani, H. (2021). MUSE-ALMA haloes VI: coupling atomic, ionized, and molecular gas kinematics of galaxies. *MNRAS*, 505(4):4746–4761.

Tanimura, H., Aghanim, N., Bonjean, V., Malavasi, N., and Douspis, M. (2020). Density and temperature of cosmic-web filaments on scales of tens of megaparsecs. *A&A*, 637:A41.

Temple, M. J., Matthews, J. H., Hewett, P. C., Rankine, A. L., Richards, G. T., Banerji, M., Ferland, G. J., Knigge, C., and Stepney, M. (2023). Testing AGN outflow and accretion models with CIV and HeII emission line demographics in z=2 quasars. *arXiv e-prints*, page arXiv:2301.02675.

The MSE Science Team, Babusiaux, C., Bergemann, M., Burgasser, A., Ellison, S., Haggard, D., Huber, D., Kaplinghat, M., Li, T., Marshall, J., Martell, S., McConnachie, A.,

Percival, W., Robotham, A., Shen, Y., Thirupathi, S., Tran, K.-V., Yeche, C., Yong, D., Adibekyan, V., Silva Aguirre, V., Angelou, G., Asplund, M., Balogh, M., Banerjee, P., Bannister, M., Barría, D., Battaglia, G., Bayo, A., Bechtol, K., Beck, P. G., Beers, T. C., Bellinger, E. P., Berg, T., Bestenlehner, J. M., Bilicki, M., Bitsch, B., Bland-Hawthorn, J., Bolton, A. S., Boselli, A., Bovy, J., Bragaglia, A., Buzasi, D., Caffau, E., Cami, J., Carleton, T., Casagrande, L., Cassisi, S., Catelan, M., Chang, C., Cortese, L., Damjanov, I., Davies, L. J. M., de Grijs, R., de Rosa, G., Deason, A., di Matteo, P., Drlica-Wagner, A., Erkal, D., Escorza, A., Ferrarese, L., Fleming, S. W., Font-Ribera, A., Freeman, K., Gänsicke, B. T., Gabdeev, M., Gallagher, S., Gandolfi, D., García, R. A., Gaulme, P., Geha, M., Gennaro, M., Gieles, M., Gilbert, K., Gordon, Y., Goswami, A., Greco, J. P., Grillmair, C., Guiglion, G., Hénault-Brunet, V., Hall, P., Hand ler, G., Hansen, T., Hathi, N., Hatzidimitriou, D., Haywood, M., Hernández Santisteban, J. V., Hillenbrand, L., Hopkins, A. M., Howlett, C., Hudson, M. J., Ibata, R., Ilić, D., Jablonka, P., Ji, A., Jiang, L., Juneau, S., Karakas, A., Karinkuzhi, D., Kim, S. Y., Kong, X., Konstantopoulos, I., Krogager, J.-K., Lagos, C., Lallement, R., Laporte, C., Lebreton, Y., Lee, K.-G., Lewis, G. F., Lianou, S., Liu, X., Lodieu, N., Loveday, J., Mészáros, S., Makler, M., Mao, Y.-Y., Marchesini, D., Martin, N., Mateo, M., Melis, C., Merle, T., Miglio, A., Gohar Mohammad, F., Molaverdikhani, K., Monier, R., Morel, T., Mosser, B., Nataf, D., Necib, L., Neilson, H. R., Newman, J. A., Nierenberg, A. M., Nord, B., Noterdaeme, P., O'Dea, C., Oshagh, M., Pace, A. B., Palanque-Delabrouille, N., Pandey, G., Parker, L. C., Pawlowski, M. S., Peter, A. H. G., Petitjean, P., Petric, A., Placco, V., Popović, L. Č., Price-Whelan, A. M., Prsa, A., Ravindranath, S., Rich, R. M., Ruan, J., Rybizki, J., Sakari, C., Sanderson, R. E., Schiavon, R., Schimd, C., Serenelli, A., Siebert, A., Siudek, M., Smiljanic, R., Smith, D., Sobeck, J., Starkenburg, E., Stello, D., Szabó, G. M., Szabo, R., Taylor, M. A., Thanjavur, K., Thomas, G., Tollerud, E., Toonen, S., Tremblay, P.-E., Tresse, L., Tsantaki, M., Valentini, M., Van Eck, S., Variu, A., Venn, K., Villaver, E., Walker, M. G., Wang, Y., Wang, Y., Wilson, M. J., Wright, N., Xu, S., Yildiz, M., Zhang, H., Zwintz, K., Anguiano, B., Bedell, M., Chaplin, W., Collet, R., Cuillandre, J.-C., Duc, P.-A., Flagey, N., Hermes, J., Hill, A., Kamath, D., Laychak, M. B., Małek, K., Marley, M., Sheinis, A., Simons, D., Sousa, S. G., Szeto, K., Ting, Y.-S., Vegetti, S., Wells, L., Babas, F., Bauman, S., Bosselli, A., Côté, P., Colless, M., Comparat, J., Courtois, H., Crampton, D., Croom, S., Davies, L., de Grijs, R., Denny, K., Devost, D., di Matteo, P., Driver, S., Fernandez-Lorenzo, M., Guhathakurta, R., Han, Z., Higgs, C., Hill, V., Ho, K., Hopkins, A., Hudson, M., Ibata, R., Isani, S., Jarvis, M., Johnson, A., Jullo, E., Kaiser, N., Kneib, J.-P., Koda, J., Koshy, G., Mignot, S., Murowinski, R., Newman, J., Nusser, A., Pancoast, A., Peng, E., Peroux, C., Pichon, C., Poggianti, B., Richard, J., Salmon, D., Seibert, A., Shastri, P., Smith, D., Sutaria, F., Tao, C., Taylor, E., Tully, B., van Waerbeke, L., Vermeulen, T., Walker, M., Willis, J., Willot, C., and Withington, K. (2019). The Detailed Science Case for the Maunakea Spectroscopic Explorer, 2019 edition. *arXiv e-prints*, page arXiv:1904.04907.

Theuns, T., Leonard, A., Efstathiou, G., Pearce, F. R., and Thomas, P. A. (1998). P$\hat{3}$M-

SPH simulations of the Lyalpha forest. *MNRAS*, 301(2):478–502.

Tremmel, M., Quinn, T. R., Ricarte, A., Babul, A., Chadayammuri, U., Natarajan, P., Nagai, D., Pontzen, A., and Volonteri, M. (2019). Introducing ROMULUSC: a cosmological simulation of a galaxy cluster with an unprecedented resolution. *MNRAS*, 483(3):3336–3362.

Tripp, T. M., Lu, L., and Savage, B. D. (1998). The Relationship between Galaxies and Low-Redshift Weak Lyα Absorbers in the Directions of H1821+643 and PG 1116+215. *ApJ*, 508(1):200–231.

Tripp, T. M., Savage, B. D., and Jenkins, E. B. (2000). Intervening O VI Quasar Absorption Systems at Low Redshift: A Significant Baryon Reservoir. *ApJ*, 534(1):L1–L5.

Tripp, T. M., Sembach, K. R., Bowen, D. V., Savage, B. D., Jenkins, E. B., Lehner, N., and Richter, P. (2008). A High-Resolution Survey of Low-Redshift QSO Absorption Lines: Statistics and Physical Conditions of O VI Absorbers. *ApJS*, 177(1):39–102.

Tumlinson, J., Peeples, M. S., and Werk, J. K. (2017). The Circumgalactic Medium. *ARA&A*, 55(1):389–432.

Vanden Berk, D. E., Richards, G. T., Bauer, A., Strauss, M. A., Schneider, D. P., Heckman, T. M., York, D. G., Hall, P. B., Fan, X., Knapp, G. R., Anderson, S. F., Annis, J., Bahcall, N. A., Bernardi, M., Briggs, J. W., Brinkmann, J., Brunner, R., Burles, S., Carey, L., Castander, F. J., Connolly, A. J., Crocker, J. H., Csabai, I., Doi, M., Finkbeiner, D., Friedman, S., Frieman, J. A., Fukugita, M., Gunn, J. E., Hennessy, G. S., Ivezić, Ž., Kent, S., Kunszt, P. Z., Lamb, D. Q., Leger, R. F., Long, D. C., Loveday, J., Lupton, R. H., Meiksin, A., Merelli, A., Munn, J. A., Newberg, H. J., Newcomb, M., Nichol, R. C., Owen, R., Pier, J. R., Pope, A., Rockosi, C. M., Schlegel, D. J., Siegmund, W. A., Smee, S., Snir, Y., Stoughton, C., Stubbs, C., SubbaRao, M., Szalay, A. S., Szokoly, G. P., Tremonti, C., Uomoto, A., Waddell, P., Yanny, B., and Zheng, W. (2001). Composite Quasar Spectra from the Sloan Digital Sky Survey. *AJ*, 122(2):549–564.

Vestergaard, M. and Wilkes, B. (2001). An Empirical Ultraviolet Iron Spectrum Template Applicable to Active Galaxies. In Ferland, G. and Savin, D. W., editors, *Spectroscopic Challenges of Photoionized Plasmas*, volume 247 of *Astronomical Society of the Pacific Conference Series*, page 359.

Voges, W. (1992). The ROSAT All-Sky X-ray survey. In ESA, Environment Observation and Climate Modelling Through International Space Projects. Space Sciences with Particular Emphasis on High-Energy Astrophysics p 9-19 (SEE N93-23878 08-88).

Voit, G. M. (2005). Tracing cosmic evolution with clusters of galaxies. *Reviews of Modern Physics*, 77(1):207–258.

Wang, H., Wang, T., Zhou, H., Liu, B., Wang, J., Yuan, W., and Dong, X. (2011). Coexistence of Gravitationally-bound and Radiation-driven C IV Emission Line Regions in Active Galactic Nuclei. *ApJ*, 738(1):85.

Wang, Q. D. and Yao, Y. (2012). Comments on "A huge reservoir of ionized gas around the Milky Way: accounting for the missing mass?" (2012 ApJL, 756, 8) and "The warm-hot gaseous halo of the Milky Way" (arXiv1211.3137). *arXiv e-prints*, page arXiv:1211.4834.

Weinberger, R., Springel, V., Pakmor, R., Nelson, D., Genel, S., Pillepich, A., Vogelsberger, M., Marinacci, F., Naiman, J., Torrey, P., and Hernquist, L. (2018). Supermassive black holes and their feedback effects in the IllustrisTNG simulation. *MNRAS*, 479(3):4056–4072.

Weisskopf, M. C., Tananbaum, H. D., Van Speybroeck, L. P., and O'Dell, S. L. (2000). Chandra X-ray Observatory (CXO): overview. In Truemper, J. E. and Aschenbach, B., editors, *X-Ray Optics, Instruments, and Missions III*, volume 4012 of *Society of Photo-Optical Instrumentation Engineers (SPIE) Conference Series*, pages 2–16.

Wen, Z. L., Han, J. L., and Liu, F. S. (2012). A Catalog of 132,684 Clusters of Galaxies Identified from Sloan Digital Sky Survey III. *ApJS*, 199(2):34.

Werk, J. K., Prochaska, J. X., Cantalupo, S., Fox, A. J., Oppenheimer, B., Tumlinson, J., Tripp, T. M., Lehner, N., and McQuinn, M. (2016). The COS-Halos Survey: Origins of the Highly Ionized Circumgalactic Medium of Star-Forming Galaxies. *ApJ*, 833(1):54.

Werk, J. K., Prochaska, J. X., Thom, C., Tumlinson, J., Tripp, T. M., O'Meara, J. M., and Peeples, M. S. (2013). The COS-Halos Survey: An Empirical Description of Metal-line Absorption in the Low-redshift Circumgalactic Medium. *ApJS*, 204(2):17.

Werk, J. K., Prochaska, J. X., Tumlinson, J., Peeples, M. S., Tripp, T. M., Fox, A. J., Lehner, N., Thom, C., O'Meara, J. M., Ford, A. B., Bordoloi, R., Katz, N., Tejos, N., Oppenheimer, B. D., Davé, R., and Weinberg, D. H. (2014). The COS-Halos Survey: Physical Conditions and Baryonic Mass in the Low-redshift Circumgalactic Medium. *ApJ*, 792(1):8.

Werner, K., Barnstedt, J., Kappelmann, N., Becker-Roß, H., and Florek, S. (2009). HIRDES-The High-Resolution Double-Echelle Spectrograph for WSO-UV. In van Steenberg, M. E., Sonneborn, G., Moos, H. W., and Blair, W. P., editors, *Future Directions in Ultraviolet Spectroscopy: A Conference Inspired by the Accomplishments of the Far Ultraviolet Spectroscopic Explorer Mission*, volume 1135 of *American Institute of Physics Conference Series*, pages 338–341.

Werner, N., Durret, F., Ohashi, T., Schindler, S., and Wiersma, R. P. C. (2008). Observations of Metals in the Intra-Cluster Medium. *Space Sci. Rev.*, 134(1-4):337–362.

Weymann, R. J., Morris, S. L., Foltz, C. B., and Hewett, P. C. (1991). Comparisons of the Emission-Line and Continuum Properties of Broad Absorption Line and Normal Quasi-stellar Objects. *ApJ*, 373:23.

Wijers, N. A., Schaye, J., and Oppenheimer, B. D. (2020). The relation between galaxies and the warm-hot circumgalactic medium probed with X-ray and UV line absorption in the EAGLE simulation. *arXiv e-prints*, page arXiv:2004.05171.

Williams, B. (2022). Science with XRISM. In *AAS/High Energy Astrophysics Division*, volume 54 of *AAS/High Energy Astrophysics Division*, page 402.02.

Wills, B. J., Brotherton, M. S., Fang, D., Steidel, C. C., and Sargent, W. L. W. (1993). Statistics of QSO Broad Emission-Line Profiles. I. The C IV lambda 1549 Line and the lambda 1400 Feature. *ApJ*, 415:563.

Wisotzki, L., Bacon, R., Brinchmann, J., Cantalupo, S., Richter, P., Schaye, J., Schmidt, K. B., Urrutia, T., Weilbacher, P. M., Akhlaghi, M., Bouché, N., Contini, T., Guiderdoni, B., Herenz, E. C., Inami, H., Kerutt, J., Leclercq, F., Marino, R. A., Maseda, M., Monreal-Ibero, A., Nanayakkara, T., Richard, J., Saust, R., Steinmetz, M., and Wendt, M. (2018). Author Correction: Nearly all the sky is covered by Lyman-α emission around high-redshift galaxies. *Nature*, 563(7733):E31–E31.

Wolfe, A. M., Lanzetta, K. M., Foltz, C. B., and Chaffee, F. H. (1995). The Large Bright QSO Survey for Damped LY alpha Absorption Systems. *ApJ*, 454:698.

Wolfe, A. M., Turnshek, D. A., Smith, H. E., and Cohen, R. D. (1986). Damped Lyman-Alpha Absorption by Disk Galaxies with Large Redshifts. I. The Lick Survey. *ApJS*, 61:249.

XRISM Science Team (2022). XRISM Quick Reference. *arXiv e-prints*, page arXiv:2202.05399.

Yoon, J. H. and Putman, M. E. (2013). The Influence of Environment on the Circumgalactic Medium. *ApJ*, 772(2):L29.

Yun, K., Pillepich, A., Zinger, E., Nelson, D., Donnari, M., Joshi, G., Rodriguez-Gomez, V., Genel, S., Weinberger, R., Vogelsberger, M., and Hernquist, L. (2019). Jellyfish galaxies with the IllustrisTNG simulations - I. Gas-stripping phenomena in the full cosmological context. *MNRAS*, 483(1):1042–1066.

Yung, L. Y. A., Somerville, R. S., Finkelstein, S. L., Hirschmann, M., Davé , R., Popping, G., Gardner, J. P., and Venkatesan, A. (2021). Semi-analytic forecasts for iJWST/i – v. AGN luminosity functions and helium reionization at iz/i = 2–7. *Monthly Notices of the Royal Astronomical Society*, 508(2):2706–2729.

Zastrocky, T. E., Howk, J. C., Lehner, N., and O'Meara, J. M. (2018). Spectral Stacking to Probe the Baryonic Mass of the Milky Way Halo with Fe XIV Absorption. *Research Notes of the American Astronomical Society*, 2(4):227.

Zhu, G., Ménard, B., Bizyaev, D., Brewington, H., Ebelke, G., Ho, S., Kinemuchi, K., Malanushenko, V., Malanushenko, E., Marchante, M., More, S., Oravetz, D., Pan, K., Petitjean, P., and Simmons, A. (2014). The large-scale distribution of cool gas around luminous red galaxies. *MNRAS*, 439(3):3139–3155.

Zhu, G. B., Comparat, J., Kneib, J.-P., Delubac, T., Raichoor, A., Dawson, K. S., Newman, J., Yèche, C., Zhou, X., and Schneider, D. P. (2015). Near-ultraviolet Spectroscopy of Star-forming Galaxies from eBOSS: Signatures of Ubiquitous Galactic-scale Outflows. *ApJ*, 815(1):48.

Zhuravleva, I., Churazov, E., Kravtsov, A., and Sunyaev, R. (2012). Constraints on the ICM velocity power spectrum from the X-ray lines width and shift. *MNRAS*, 422(3):2712–2724.

Danksagung

This journey started when I was only a kid, where my parents had always encouraged me to follow my dreams. Thanks to my brother and sister, wish you always know its very hard to be far away from you. I have so much to give thanks for. To my grandfather, abuelo Petoto, who was the first one to introduce me to astronomy. To my mentor, Blas Servin, the one that made sure I didn't stray from my path, you're always in my heart.
To my tio Ricardo, the one that bet on me first, visited me everywhere, and made me feel like home wherever an whenever we met.
To the funding from Paraguay, BECAL, that made my dreams come true.
During my masters I had the most wonderful advisor, Juan Antonio, that always helped me through the first hardships of this career. During the same time I met the best people I could ever meet that really made Tenerife a real paradise, thanks to Javi, Virgi and Mila, for making me never want to leave.
For their patience and guidance throughout this roller-coaster, Celine and Andrea, I'm so thankful for having people with such great hearts as advisors above all. Thank you for making me pull it through.
To my best friend during covid times, Liliya, don't know what would have been those years if we didn't have each other. To the small community of european family that accepted me and made me feel welcomed from the very beginning, Ricky, Adam, Damien and Hanna, Jere, Linda, Florian, and to the big latin family that made of Munich a home, Jay, Joaco, Moni, and extended family Simon, Nahir and Daniel, Ale and Ramses, there will never be enough words to describe the bond.
Thank you for existing in my life Nathan, Julia, Rohan.
To Ema and Thales, you are an inspiration and have forever stolen a piece of my heart.
To all the amazing people that received me with a beautiful smile every morning in the IPP entrance from the guards, Zoist, Bert, Ali, to the receptionists Erich and Gisela for always helping with anything and everything and exchanging small chocolates, to the cleaning ladies Sabrina, Martina, you always made my days start beautifully with the most welcoming "Gutten Morgen" I've ever heard.
And I can't end this without saying again thank you mum and dad, you keep teaching me, being the best example, supporting me and loving me so much.

Este viaje comenzó cuando yo era sólo un niña, donde mis padres siempre me habían animado a seguir mis sueños. Gracias a mi hermano y a mi hermana, espero que siempre

sepan que es muy duro estar lejos de ustedes. Tengo tanto por lo que dar las gracias. A mi abuelo Petoto, que fue el primero que me introdujo en la astronomía. A mi mentor, Blas Servín, el que hizo que no me desviara de mi camino, siempre estás en mi corazón. A mi tio Ricardo, el que apostó por mi primero, me visitó en todas partes, y me hizo sentir como en casa donde quiera y cuando quiera que nos encontráramos.
A la financiación de Paraguay, BECAL, que hizo que mis sueños se hicieran realidad. Durante mi maestría tuve al asesor más maravilloso, Juan Antonio, que siempre me ayudó en las primeras dificultades de esta carrera. Al mismo tiempo conocí a las mejores personas que he podido conocer y que realmente hicieron de Tenerife un verdadero paraíso, gracias a Javi, Virgi y Mila, por hacer que nunca me quisiera ir.
Por su paciencia y guía a lo largo de esta montaña rusa, Celine y Andrea, estoy muy agradecida por tener a personas con un corazón tan grande como asesores por encima de todo. Gracias por hacerme salir adelante.
A mi mejor amiga durante los tiempos covid, Liliya, no se que hubiera sido de aquellos años si no nos hubiéramos tenido la una a la otra. A la pequeña comunidad de la familia europea que me aceptó y me hizo sentir bienvenida desde el principio, Ricky, Adam, Damien y Hanna, Jere, Linda, Florian, y a la gran familia latina que hizo de Munich un hogar, Jay, Joaco, Moni, y la familia extendida Simon, Nahir y Daniel, Ale y Ramses, nunca habrá suficientes palabras para describir el vínculo.
Gracias por existir en mi vida Nathan, Julia, Rohan.
A Ema y Thales, son una inspiración y robaron para siempre un pedazo de mi corazón.
A todas las personas increíbles que me recibían con una hermosa sonrisa cada mañana en la entrada del IPP, desde los guardias, Zoist, Bert, Ali, a los recepcionistas Erich y Gisela por ayudarme siempre con todo e intercambiar pequeños chocolates, a las señoras de la limpieza Sabrina, Martina, siempre hacen que mis días empiecen maravillosamente con el "Gutten Morgen" más acogedor que he oído nunca.
Y no puedo terminar esto sin volver a dar las gracias a mamá y papá, siguen enseñándome, siendo el mejor ejemplo, apoyándome y queriéndome tanto.